Engineering a Chromoprotein Optimized for Photoacoustic Imaging and Biosensing Applications

by

Yan Li

A thesis submitted in partial fulfillment of the requirements for the degree of

Master of Science

Department of Chemistry

University of Alberta

Abstract

A subset of the family of fluorescent proteins are the non-fluorescent chromoproteins which serve as important tools in biomedical research. Recently, chromoproteins have been utilized as both reporter molecules in photoacoustic imaging and acceptor chromophores in Förster resonance energy transfer (FRET)-based biosensors. Photoacoustic imaging enables imaging deep in tissue with relatively high resolution while FRET-based biosensors are the principal technology for live cell imaging of physiological events, such as enzymatic activity, protein-protein interaction and changes in small molecule concentration. However, there are few chromoproteins that have ideal characteristics for photoacoustic imaging and biosensors due to a limited ability to artificially evolve them for improved photoacoustic signals. A major challenge of directed laboratory protein evolution is establishing a simple and efficient screening method.

In this thesis we describe our efforts to address this shortcoming in the area of chromoproteins evolution and application by developing a novel colony-based photoacoustic screening method. Through iterative rounds of directed evolution and subsequent screening, the best variants of chromoproteins exhibited higher photoacoustic signal and extinction coefficient and lower quantum yield. We also report the application and performance of a tandem dimer chromoprotein in FRET-based biosensors compared with monomer acceptor. The change of donor fluorescence represented the functionality of biosensor attributing to non-fluorescence of acceptor. Specifically, we demonstrated that tandem dimer-based FRET

biosensors are useful for detecting activation of caspase-3 and changes in calcium ion (Ca^{2+}) concentration in live cells.

Preface

The research described in Chapter 2 is an interdisciplinary collaboration, led by Dr. Roger J. Zemp in Department of Electrical & Computer Engineering at the University of Alberta, and Dr. Robert E. Campbell in Department of Chemistry at the University of Alberta. All photoacoustic imaging is credited to Alexander Forbrich, a gradate student under the supervision of in Dr. Zemp. The photoacoustic imaging data analysis is done with the assistance of Alex. I was responsible for the molecular biology experimentation component, including directed evolution, primary absorption screening, protein purification, in vitro protein characterization and sample preparation for photoacoustic imaging.

Acknowledgements

Choosing Dr. Robert E Campbell as my supervisor was one of the best decision I ever made! He has given me the opportunity to work in his awesome group and helped me to accomplish the research presented in this thesis. I am sincerely grateful to him.

I want to thank Dr. Roger Zemp for his cooperation on the photoacoustic imaging of chromoproteins. His support and guidance was essential to the smooth progress of my research. In addition, working with his graduate student Alexander Forbrich was an excellent experience. My thanks go to Alex for providing me with the endless photoacoustic imaging support, as well as editing sections of this thesis related to photoacoustics.

I believe I owe a lot of thanks to my lab mates Dr. Yidan Ding, Dr. Spencer Alford and PhD candidate Yi Shen. They took time out of their busy schedule to patiently teach me many molecular biology techniques used in my research. Outside the lab, they were always there to provide kind help and encouragement when life got tougher. Dr. Alford has also graciously helped me edit this thesis. I'd also like to thank Jhon Ralph Enteria and Wei Zhang for their kind assistance both inside the lab and out. Finally, thank you to all my other lovely group members, including Ahmed Abdelfattah, Hang Zhou, Matthew Wien, Nazanin Assempour, Jiahui Wu, Landon Zarowny, Retesh K. Saini, Tiffany Lai, Yongxin Zhao. It was your collective kindness and friendships that made working in the lab such a pleasurable and unforgettable experience.

Beyond the lab, I would like to acknowledge my former university professors Yongxin Ji and Zhongzheng Li for their kind attention and best

wishes in the past three years. My life at the University of Alberta would not have been as interesting and memorable if not for my friends Lance Wu, Fangxin Ge, Ping Jiang, Xiuli Yang, Qiuyu Yang, Kezhen Bai, Tao Huai, Xue Li, Qian Shi, Feng Jia, Mengliao Wang and Chengmin Cao others.

Finally, I owe everything I've achieved so far to my family for their immense and continuous love, support and faith.

Table of Contents

List of Tables

List of Figures

List of Abbreviations

a	a tissue dependent constant
β	thermal coefficient of volume expansion
Γ	Gruneisen parameter
ε	extinction coefficient
ε	molar absorbtivity
κ	thermal diffusivity
κ^2	orientation factor
λ	wavelength
λ_A	central wavelength of photoacoustic signal
μ	acoustic attenuation coefficient
μ_a	absorption coefficient of the molecule
v_s	speed of sound in the medium
τ_{th}	thermal relaxation time
τ_s	stress relaxation time
Φ	quantum yield
Φ	laser fluence
Δf_A	photoacoustic signal bandwidth
A	acceptor fluorescent protein
A	absorbance
aeCP597	*Actinia equine* chromoprotein with an absorption maximum at 597 nm
AL	acoustic lens
ANSI	American National Standards Institute
AR-PAM	acoustic-resolution photoacoustic microscopy

avGFP	*Aequorea* victoria green fluorescent protein
asCP	*Anemonia sulcate* Chromoprotein
asFP595	*Anemonia sulcate* Fluorescent protein with emission at 595nm
BCA	bicinchoninic acid
BFP	blue fluorescent protein
B-PER	bacterial protein extraction reagent
M2tC	M13-t-Ultramarine 7.2- tdTomato-CaM
CaM	calmodulin
CCD	charge-coupled device
CFP	cyan fluorescent protein
cgCP	*Condilactis gigantea* chromoprotein
cjBlue	*Cindopus japonicas* blue color chromoprotein
c	concentration
C_p	heat capacity
cm	centimeter
Corl	correction lens
CP	chromoprotein
Cys	cysteine
d_c	the characteristic linear dimension of the sample volume being heated
d_p	characteristic linear dimension of the sample volume being heated
D	donor fluorescent protein
D	dimension
DA	dark acceptor
DAQ	data acquisition card

dB	decibel
DEVD	aspartate-glutamate-valine-aspartate
DMEM	Dulbecco's modified eagle media
DNA	deoxyribonucleic acid
DNase	deoxyribonuclease
dNTPs	deoxynucleotide triphosphates
DIO	digital input-output card
DsRed	*Discosoma* species Red fluorescent protein
E. coli	*Escherichia coli*
eCGP123	enhanced consensus green protein variant 123
EGFP	enhanced green fluorescent protein
EGTA	ethylene glycol-bis(2-aminoethylether)-N,N,N′,N′-tetraacetic acid
eqFP611	Entacmaea quadricolor Fluorescent protein with e emission maximum at 611nm
EYFP	enhanced yellow fluorescent protein
f	frequency of the ultrasound
f_A	frequency of the PA signal, respectively
FBS	fetal bovine serum
FD	fluorescent donor
FLIM	Fluorescence-lifetime imaging microscopy
FP	fluorescent protein
FRET	Förster resonance energy transfer
FWHM	full width at half maximum
GFP	green fluorescent protein
Glu	glutamic acid

Gly	Glycine
gtCP	*Gonipora tenuidens* chromoprotein
GTPase	guanosine triphosphatase
h	hour
hcCP	*Heteractis crispa* chromoprotein
HcRed	far red fluorescent protein developed from hcCP
HeLa	cervical cancer cell line originating from Henrietta Lacks
HHBSS	HEPES-buffered Hank's balanced salt solution
HT	hula twist
IPTG	isopropyl β-D-thiogalactopyranoside
iRFP	infrared fluorescent protein
kDa	kilodalton
K_d	dissociation constant
KFP	Kindling Fluorescent Protein
l	the path length of the cuvette in which the sample is contained
LB	Luria Bertani
M	mirror
MBSU	Molecular Biology Services Unit
MC	motor controller
Met	methionine
mg	milligram
MHz	Megahertz
mJ	millijoule

mL	milliliter
mm	millimeter
mM	millimolar
MOPS	3-(N-morpholino)propanesulfonic acid
mW	milliwatt
n	Hill coefficient
NA	numerical aperture
NA_A	numerical aperture of the ultrasonic transducer
Nd:YAG	neodymium-doped yttrium aluminium garnet
nm	nanometer
nM	nanomolar
NTA	nitrilotriacetic acid
OAM	optically absorbing absorber
OL	objective lens
OPO	optical parametric oscillator
OR-PAM	optical-resolution photoacoustic microscopy
p	pressure rise
PA	photoacoustic
PAM	photoacoustic microscopy
PAT	photoacoustic tomography
PBS	phosphate buffered saline
PCR	polymerase chain reaction
PD	photodiode
PDB	protein data bank
Phe	phenylalanine

PR	pulser-receiver
QY	quantum yield
R_0	the Förster radius at which 50% of the excitation energy of donor is transferred to the acceptor chromophore
$R_{A,AR/OR}$	axial resolution of AR-PAM or OR-PAM
$R_{L,AR}$	lateral resolution of AR-PAM
$R_{L,OR}$	lateral resolution of OR-PAM
RAP	right angled prism
REACh	resonance energy-accepting chromoprotein
RFP	red fluorescent protein
RhP	rhomboid prism
RPE	rental pigment epithelium
Rtms5	chromoprotein isolated from reef building coral *Montipora efflorescens*
S	slopes
SDS-PAGE	sodium dodecyl sulfate polyacrylamide gel electrophoresis
StEP	staggered extension process
shCP	*Stichodactyla haddoni* chromoprotein
SNR	signal-to-noise ratio
SOL	silicone oil layer
tdTomato	tandem dimeric Tomato fluorescent protein
Tyr	tyrosine
µg	microgram
µL	microliter
µM	micromolar
Um	Ultramarine

UST	ultrasound transducer
UT	ultrasonic transducer
UV	ultraviolet
V	volt
WT	Water tank
X-gal	5-bromo-4-chloro-3-indolyl-β-D-galactoside
YFP	yellow fluorescent protein

Chapter 1: Introduction

1.1 Overview and premise

Organisms exhibit an enormous variety of colors and fluorescent hues. These visual appearances are determined by structural coloration or biological pigmentation, or the combination of both [1]. Structural coloration arises from an interference effect caused by schemochromes, the microscopically intricate ultrafine physical organization of tissues, such as the tail feathers of male peacocks or the wings of butterflies. Biological pigments, also known as biochromes or simply pigments, typically exist as chromoproteins or low-molecular weight molecules. The extended conjugated π-system of these pigments endows them with the ability to absorb certain wavelengths of visible light and reflect or transmit others, resulting in many possible colors.

As a rule, a chromoprotein is a protein that consists of a pigmented prosthetic group (or cofactor, generally a small non-peptide molecule or metal ion) bound to the folded protein structure [2-4]. The most prevalent example of a chromoprotein is hemoglobin, a serum protein that carries an iron-containing heme cofactor and confers the characteristic red color to oxygenated mammalian blood.

Another type of protein that can change the visible color of an animal is the green fluorescent protein (avGFP) [5] from jellyfish *Aequorea victoria* and its homologues [6]. The distinctive color and fluorescence properties of GFP are conferred by a chromophore that autonomously forms from its intrinsic amino acid sequence. Accordingly, GFP's optical properties are genetically-encoded and require no additional prosthetic groups or cofactors [7].

The GFP-like family members can be categorized into two clades [8]. The first, more prominent, clade is comprised of fluorescent proteins, which emit a large fraction of absorbed energy as photons. The second clade is comprised of non-fluorescent chromoproteins, which still effectively absorb, but fail to emit, light. The former clade are widely utilized as optical reporters for protein localization and gene expression, as components of genetically-encoded biosensors and probes, and as non-invasive *in vivo* probes of biological processes occurring in the intra-cellular environment [9-11].

Non-invasive imaging of tissues in live organisms is an advantageous feature enabled uniquely by GFP-like proteins, on account of their ability to genetically encode fluorescence in living cells and tissues, without the requirement of adding exogenous contrast reagents [12]. However, the utility of these proteins for non-invasive imaging deep into tissues with high resolution is hindered by the intense optical scattering and absorption in biological tissue (at depths greater than ~1 mm). This generally results in the acquisition of low-resolution images. Obtaining high-resolution optical images at depths ~1 mm below the tissue surface is incredibly challenging [13]. Fortunately, some optically absorbing molecules can convert photons into acoustic waves, which can be detected by using an ultrasound transducer. The acoustic waves are attenuated and scattered orders of magnitude less than the photons and allow for higher resolution imaging of deeper optically-absorbing structures *in vivo* compared with traditional optical imaging techniques. The conversion of light energy into acoustic energy is known as the photoacoustic effect and photoacoustic imaging has been an emerging area of research for biomedical applications. Broadly, photoacoustic imaging can be divided into

two groups: (1) photoacoustic microscopy (PAM) which uses a single illumination source and acoustic detector, and (2) photoacoustic tomography (PAT) which uses multiple illumination sources or multiple detectors to visualize the generation of acoustic waves [14]. By taking advantage of the photoacoustic effect, these photoacoustic imaging techniques overcome the limitations imposed by scattering of optical photons in tissue [15, 16] and thus provides a method for high-resolution visualization of GFP-like proteins deep within living organisms [17, 18].

GFP-like proteins not only can be used as static imaging labels (in both fluorescence and photoacoustic imaging), but also can be engineered to be active biosensors. A variety of GFP-like protein-based biosensors have served as valuable molecular tools in cell biology, especially in the field of neuroscience [19-21]. One of the most common types of biosensor relies on Förster resonance energy transfer (FRET). Prominent examples of very useful FRET-based biosensors include designs to monitor Ca^{2+} dynamics and caspase-3 activity in single live cells [22-24]. However, an oft-encountered limitation is the problem of fluorescent protein spectrum contamination, including direct acceptor excitation and donor emission bleed-through. For this reason the FRET biosensor designs incorporating 'dark acceptors' -- where the donor is a fluorescent protein and the acceptor is a non-fluorescent chromoprotein -- has recently attracted much attention [25, 26].

For the work described in this thesis, we attempted to engineer improved non-fluorescent chromoproteins by directed evolution and apply them for photoacoustic imaging and FRET-based biosensing applications. The remainder of the introduction provides necessary background details on topics

including the properties and chemistry of chromoproteins, the principles and application of photoacoustic imaging, and designs of chromoprotein FRET-based biosensors and their applications in live cell imaging.

1.2 Non-fluorescent chromoproteins

1.2.1 Discovery of chromoproteins

A wide range of fluorescent and non-fluorescent pigments are the key determinants of the diverse colorization of marine corals [27-29]. The non-fluorescent pigments are chromoproteins, which generate vivid color patterns due to strong absorptions [30]. The first two chromoproteins discovered in nature -- one pink and one blue -- were named pocilloporins, and were isolated from two *Scleractinian* coral species [31]. The pink pocilloporin has strong absorbance at 560 nm and 390 nm, and the blue pocilloporin absorbs at 590 nm. Biochemical data indicates pocilloporins are tetrameric complexes with 28 kD subunits. However, their GFP-like "β-can" three-dimensional structures were not determined until five years after they were discovered -- first by molecular modeling [27] and soon after by X-ray crystallography [32].

In 2000, the GFP-like chromoprotein asCP (or asulCP), isolated from sea anemone *Anemonia sulcate*, was the first chromoprotein cloned and expressed in the heterologous systems of bacteria and mammalian cells [33]. An additional feature of this protein is the ability to photoswitch between two different states [33-35]. Initially non-fluorescent, asCP becomes fluorescent with an emission at 595 nm ("kindling") upon exposure to green light. For this reason, the protein is also known as asFP595, where "FP" stands for "fluorescent protein". The protein in the fluorescent state relaxes back to its initial non-fluorescent state or can be "quenched" immediately by blue light

irradiation [33]. Since these initial findings, asCP has been thoroughly characterized both spectroscopically and structurally [34, 35]

In addition to pocilloporin and asCP, a variety of other chromoproteins have been isolated from nature, such as the purple hcCP from *Heteractis crispa* [36], the purple-blue gtCP from *Gonipora tenuidens* [37], the blue aeCP597 from *Actinia equine*[38], the blue cjBlue from *Cindopus japonicas* [39] and the purple shCP from carpet anemone *Stichodactyla haddoni* [40]. In addition to isolation from natural sources, some chromoproteins have also been engineered from fluorescent proteins, including the dark yellow chromoprotein REACh developed from yellow fluorescent protein (YFP) [25] and an orange chromoprotein developed from green fluorescent protein eCGP123 [39]. The functional role of chromoproteins in corals is still poorly understood, but it may be similar to the proposed roles of fluorescent proteins; they may provide protection for photosystems of their resident microalgae by regulating the light environment [41, 42].

1.2.2 Primary sequence and three-dimensional structure

To facilitate a detailed explanation of chromoproteins and their three-dimensional structure, the chromoprotein Rtms5, isolated from the reef-building coral *Montipora efflorescens* [43], will be discussed as an illustrative example. Rtms5 was the first chromoprotein to have its X-ray crystal structure solved [32]. The protein is 221 amino acids with a calculated molecular mass ~25 kDa. The protein folds into a rigid cylindrical 11-antiparallel stranded β-barrel (β-can), with a short helix and the interconnecting loops isolating the chromophore from surrounding solvent. A central helix runs coaxial through the middle of the β-can. Residues Gln65–Tyr66–Gly67 on the central helix

ultimately form the chromophore, after undergoing a series of post-translational modifications facilitated by the amino acid environment provided by the surrounding β-can shell [32]. The chromophore is buried in the core of the protein and oriented approximately perpendicular to the longitudinal axis of the barrel. Rtms5 exists naturally as a tetramer even in relative low protein concentration solution (i.e., 0.1 mg/ml) according to analytical ultracentrifugation [44]. **Figure 1.1** illustrates the three dimensional structure in two different viewing angles.

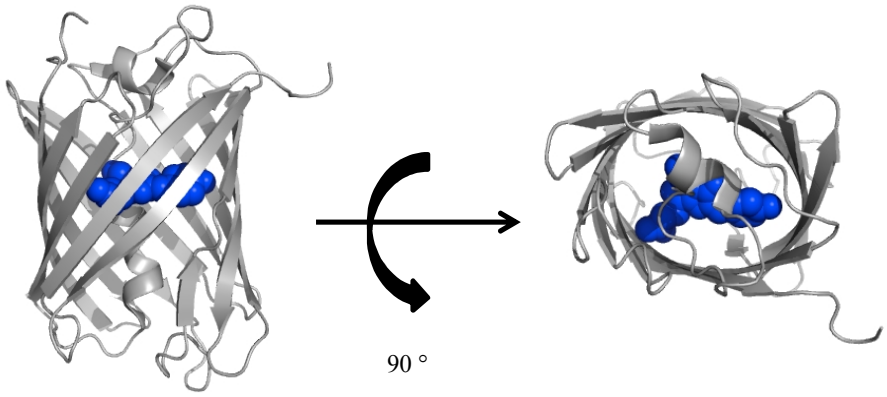

Figure 1.1 Three-dimensional structure of Rtms5. A cartoon representation of Rtms5 (PDB ID 1MOU) [32] with the chromophore shown in blue spheres, α-helix and β-sheet in gray.

All characterized chromoproteins share a structurally homologous three-dimensional β-barrel fold with fluorescent proteins, despite significant differences in their primary sequences. For example, Rtms5 exhibits only 22% and 63% sequence identity with avGFP [45] and DsRed (a well characterized red fluorescent protein from *Discosoma* sp.) [46], respectively. The complete and proper folding of the β-barrel is the key factor dictating correct and autogenic formation of the chromophore.

1.2.3 Chromophore formation

The mature chromophore is synthesized by an autogenic posttranslational modification of a tripeptide in the central helix. The mechanisms for chromophore formation in avGFP and DsRed are the most widely studied [7] [47]. Briefly, the chromophore formation pathway involves: (1) pre-organization of chromophore-forming residues; (2) cyclization; (3) oxidation; and (4) dehydration. Since chromoproteins isolated from coral share a relatively high sequence identity with DsRed, and have a DsRed-like chromophore tripeptide composition (X–Tyr66–Gly67, where X = any of a number of different possible amino acids), it has been proposed that chromoproteins and DsRed share a similar pathway for chromophore formation [48]. In addition, the similarity [32] of the chromophore structures, as well as the fact that it is possible to interconvert red fluorescent proteins (RFPs) derived from DsRed into non-fluorescent chromoproteins by mutagenesis [49], also support a similar chromophore formation pathway.

In this thesis, the latest and most thoroughly validated chromophore formation pathway [47] is adopted to explain the chromophore formation of chromoproteins, using chromoprotein Rtms5 (Glu65–Tyr66–Gly67) as an example. The only chemical species required for chromophore formation -- aside from the protein itself -- is molecular oxygen [50]. The mechanism for this process involves several key steps (**Figure 1.2**). (1) Protein folding distorts the polypeptide backbone and positions Glu65 carbonyl carbon close to Gly67 amide nitrogen in the precyclized state. (2) Peptide cyclisation initiated by attack of the nucleophilic Gly67 amide nitrogen on the Glu65 carbonyl carbon to form an imidazolinzone ring (intermediate I). (3)

Intermediate I is trapped by oxidation and results in intermediate II, the hydroxylated cyclic imine. (4) By OH^- exchange, interconversion of intermediate II and intermediate III rapidly reaches equilibrium. (5) A short-lived intermediate IV forms from the cyclic imine (intermediate III) oxidation. (6) Intermediate IV undergoes irreversible hydroxylation and renders intermediate V. (7) A phenolic form of chromophore arises from dehydration of intermediate V. (8) The final anionic species is generated by deprotonation of the phenol chromophore. The highly conjugated π system confers the chromophore's light absorbing ability. The acylimine bond that extends the π system renders the absorbance red-shifted relative to the GFP chromophore [51, 52].

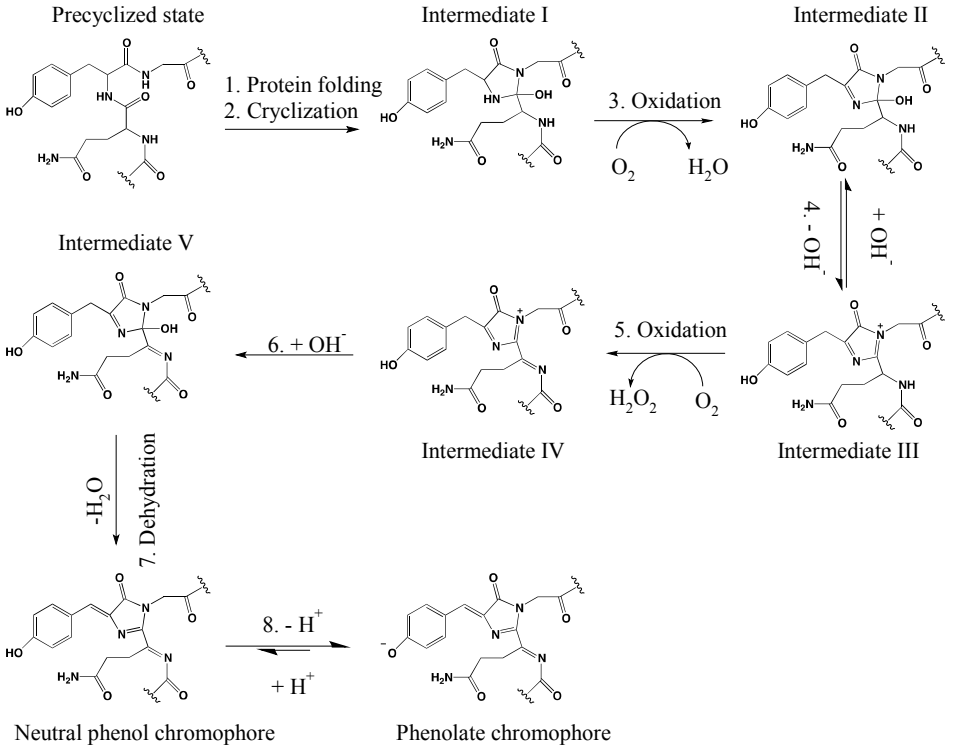

Figure 1.2 Proposed mechanisms for chromophore formation in chromoproteins (CPs).

1.2.4 Chromophore conformation of chromoproteins

Although chromoproteins and DsRed share a common chromophore formation pathway and identical chromophore structures, their final chromophore conformations are different. X-ray crystallographic studies show non-fluorescent chromoproteins typically adopt a non-planar *trans* conformation [32], which is distinct from the co-planar *cis* chromophore found in fluorescent proteins [53]. The lone exception is the chromoprotein eqFP611[54], which has a co-planar *trans* chromophore [51]. **Figure 1.3** illustrates the chromophore structures of Rtms5, DsRed and eqFP611.

The coplanar chromophore conformation provides a high fluorescent quantum yield (QY), but the *trans* non-coplanar chromophore cannot emit photons, rendering proteins with these chromophores non-fluorescent. Crystallographic studies have also revealed *cis/trans* isomerization is responsible for the photoswitch phenomenon observed in Kindling fluoresncent protein (KFP) asCP-A143G. In this case, the *cis* isomer is the fluorescent chromophore, while the *trans* isomer is not fluorescent [55]. A similar phenomenon is also observed in far-red fluorescent protein HcRed (from *Heteractis crispa* chromoprotein hcCP) [56] and Rtms5-H146S [57].

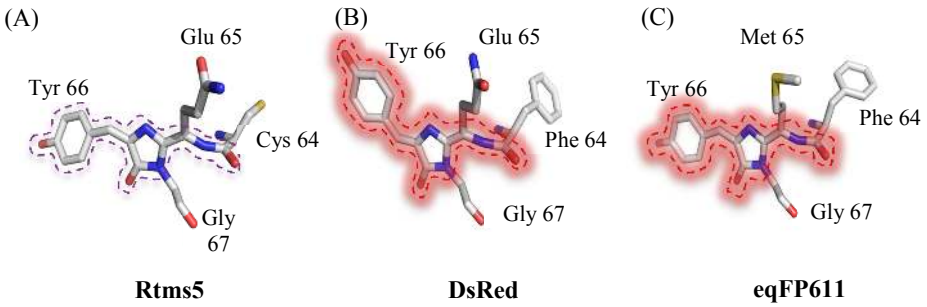

Figure 1.3 Chromophore structures of GFP-like proteins. (A) Non-fluorescent chromoprotein Rtms5; (B) Fluorescent protein DsRed; (C) Far-red fluorescent protein, *Entacmaea* eqFP611. Carbon, nitrogen, oxygen and sulfur are gray, blue, red and yellow, respectively. Dashed lines mark the conjugated systems of the chromophores.

Crystallographic studies suggest a hula-twist (HT) isomerization mechanism [34] best explains the observed *trans-cis* chromophore interconversion (**Figure 1.4**). The HT mechanism involves concurrent rotation around the τ (N_1-C_1-C_2-C_3) and the φ (C_1-C_2-C_3-C_4) dihedral angles [58], which might be induced by pH changes [57, 59] or absorbance of specific wavelengths of light [35].

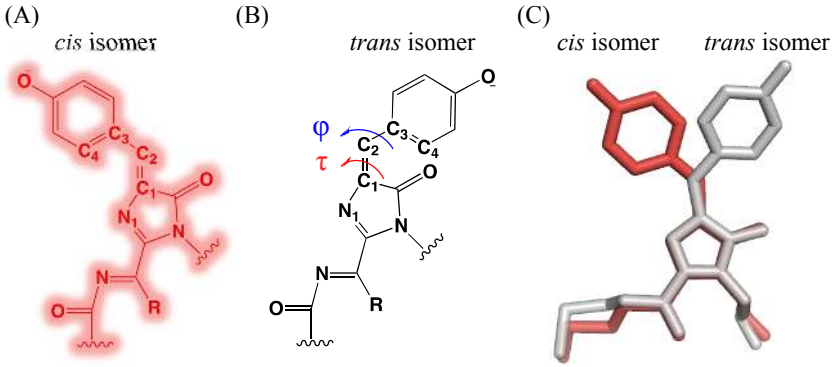

Figure 1.4 *Cis* and *trans* conformation of chromoproteins' chromophore. (A) Fluorescent state of *cis* chromophore; (B) Dark state of *trans* chromophore; (C) Over lay of *trans-cis* conformation of asCP chromophore (QYG). Fluorescent state and dark state are represented in red and gray, respectively. Dihedral angles τ and φ are depicted by red and blue, respectively.

1.2.5 Engineered chromoprotein variants

Although numerous naturally occurring chromoproteins have been discovered and isolated, their usage as imaging tools has been hindered by the limited number of spectrally distinct proteins, as well as their propensity for oligomerization. Fortunately, like their fluorescent protein cousins, chromoproteins are amenable to engineering by altering their gene sequences to produce chromoproteins exhibiting desired and improved spectral and physical properties. Such engineering would greatly extend the utility of chromoproteins in various research applications.

Currently, there are three classes of engineered chromoprotein variants. The first class comprises chromoproteins that have been engineered to be fluorescent proteins with far-red fluorescence emission. Conversion of chromoproteins into fluorescent proteins has opened up a novel source of far-red fluorescent proteins. For example, the far-red fluorescent protein evolved from chromoprotein aeCP597 (from *Actinia equina*) has emission at 663 nm [36, 38, 49]. If chromoproteins are discovered with even more red-shifted absorption spectra, it will likely be possible to engineer fluorescent proteins with further red-shifted emissions. The second class of chromoprotein variants are the 'kindling'-type fluorescent proteins (KFP). These proteins have fluorescence "on" and "off" states that can be interconverted by illumination with light at distinct wavelength. That is, they are photoconvertible. For example a group of red and far-red kindling fluorescent proteins have been derived from asCP, cgCP (from *Condilactis gigantea*) and hcCP, through extensive mutagenesis [60]. The third class of chromoprotein are those monomeric variants engineered from oligomeric parent chromoproteins. Most

naturally occurring chromoproteins are tetrameric [39, 43], with the exception of anm2CP (from *Anthomedusa*), which is a native monomer [61]. To extend the biological utilities of chromoproteins, monomeric chromoproteins may be created through mutagenesis. One example is Ultramarine, the first engineered monomeric chromoprotein derived from the tetramer Rtms5. This monomer has been used as a dark FRET acceptor in protease sensing biosensor designs [44].

1.2.6 Protein engineering

The objective of protein engineering research is to generate proteins with highly tailored and/or new functionality by making purposeful genetic changes to the genes encoding the proteins [62]. Two strategies are commonly implemented to engineer proteins: rational computational design and mutagenesis with directed evolution. The former involves theoretical computational analysis relying on existing data and knowledge, such as sequence-structure-function studies of a precursor protein and its homologues, or published crystallographic data [63, 64]. The latter strategy is inspired by natural selection through the "survival of the fittest" and aims to apply an artificial selection pressure in the laboratory. This process utilizes molecular biology techniques and genetic or phenotypic screening methods [65] and iterative cycling. In brief, a typical directed evolution strategy involves: (1) generation of a diverse gene library; (2) transformation of the gene library into a suitable host (e.g., *Escherichia coli*); (3) expression of the gene library on a suitable medium; (4) screening the library for variants exhibiting a desired phenotype; (5) selection and isolation of desired clones such that only the genes encoding the best (desired) properties are used as templates for next

round of mutagenesis and selection pressure (**Figure 1.5**). The computational design and directed evolution strategies are not mutually exclusive, and are often implemented together to arrive at the desired protein. Protein engineering is most efficient when both strategies are integrated into a coordinated engineering effort, leveraging the strengths of both approaches.

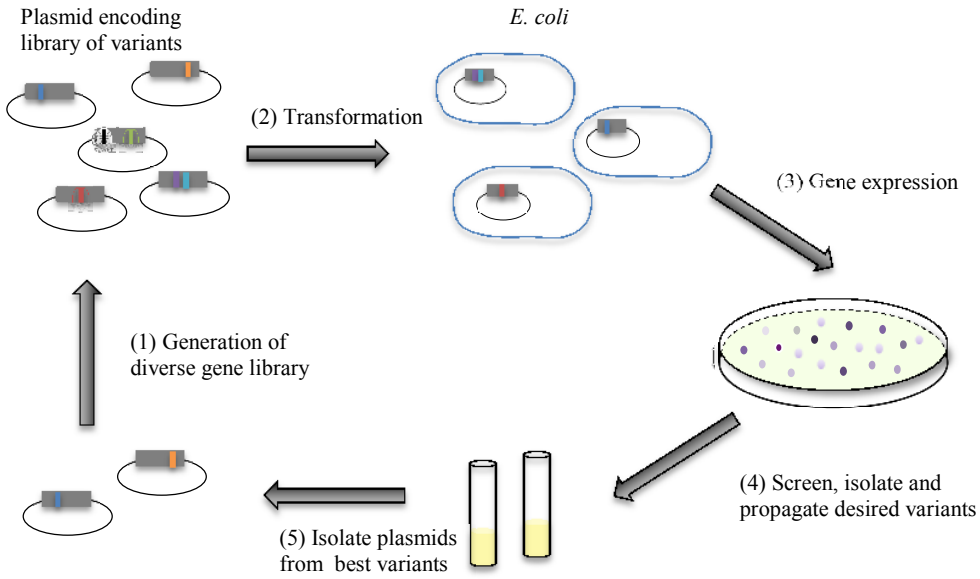

Figure 1.5 Schematic representation of the process of directed evolution.

The practical techniques for generation of diverse gene libraries are now relatively well established and commonly include site-directed mutagenesis, random mutagenesis, and gene recombination. Based on rational design, specific combinations of amino acids, or even all 20 common amino acids, can be easily and effectively introduced into specific sites of the target protein by site-directed mutagenesis [66]. This allows the generation of a small gene library that encode all 20 amino acids at a given position in the protein (saturation mutagenesis) or a subset of predefined amino acids (semi-saturation mutagenesis) at specific positions in the protein [65].

Another approach for creating a gene library is by random mutagenesis. Random mutagenesis utilizes an error-prone polymerase chain reaction (PCR) dependent technique [67]. In this procedure, incorrect nucleotides are incorporated by a low fidelity polymerase -- typically *Taq* polymerase -- with mutagenic buffering conditions during gene amplification. The template may be a single gene or a pool of different variants of the same gene. The mutation rate can be modulated by the concentration of Mg^{2+} and Mn^{2+}, the concentration of deoxynucleotide triphosphates (dNTPs), the template amount, and the number of PCR reaction cycles [68]. However, harmful mutations occur more frequently as the mutation rate increases, and improved variants are thus less likely to be obtained [69]. Therefore, directed evolution is a highly iterative process and large gains in desired functions are rarely observed in a single round of evolution. To overcome this limitation, gene hybridization methods were developed and are commonly utilized in protein engineering efforts. This approach is powerful because it can combine beneficial mutations together for synergistic gains in function by assembling hybrid genes from several gene templates. Among all known gene recombination techniques [65, 70], DNA-shuffling [71] and staggered extension PCR (StEP) [72] are the most commonly implemented. In DNA-shuffling, several gene templates containing mutually exclusive beneficial mutations are fragmented by DNase, and then are reassembled and amplified by PCR to achieve gene recombination [71]. In StEP, gene fragments are generated and recombined by modified PCR with abbreviated thermocycling conditions that results in template switching [72].

While good quality gene libraries are a necessity for protein engineering, the method of screening is equally, if not more, important. An effective screening strategy should be accessible and able to distinguish the readouts from single clones in order to isolate those with desired properties [73]. A commonly used screening strategy is to directly screen colonies on agar growth media or in cell lysates [74]. Advances in screening methods have correlated with the number of and successful protein engineering efforts.

1.3 Photoacoustic imaging

Photoacoustic imaging is a rapidly developing hybrid imaging modality based on the photoacoustic effect. Chromophores absorb light energy, typically from a nanosecond-pulsed laser source, causing a transient thermoelastic expansion that generates an acoustic pressure wave that can be detected using ultrasound transducers [75]. Since acoustic waves are absorbed and scattered much less than the visible light used in traditional optical imaging techniques, photoacoustic imaging is capable of imaging reporter molecules in deep tissues with a high depth-to-resolution ratio. This combination of high resolution and high penetration depth has proven useful for studying the microvasculature structure and development (angiogenesis) in animals, as well as studying the flow rate and oxygen saturation and consumption in blood vessels non-invasively, *in vivo* [14].

1.3.1 Photoacoustic effect

Although, the photoacoustic effect was first reported by Alexander Graham Bell in the 1880s [76], its practical use could not be realized until the advent of the laser. For biomedical imaging, it wasn't until 1994 when Kruger demonstrated its application in highly scattering media [77]. Hoelen

subsequently applied the photoacoustic principle to biomedical imaging in 1998 [78]. The photoaoustic effect explains the generation of an acoustic wave by absorption and conversion of electromagnetic energy [75]. When a short-pulsed laser beam illuminates a sample, the optically absorbing molecules inside the sample will locally absorb the energy and convert it into heat. The sudden rise in temperature leads to a transient thermo-elastic expansion, which initiates the acoustic pressure wave. The acoustic waves propagate through the media to the surface and are detected by ultrasound detectors (e.g., a piezoelectric transducer) positioned nearby (**Figure 1.6**).

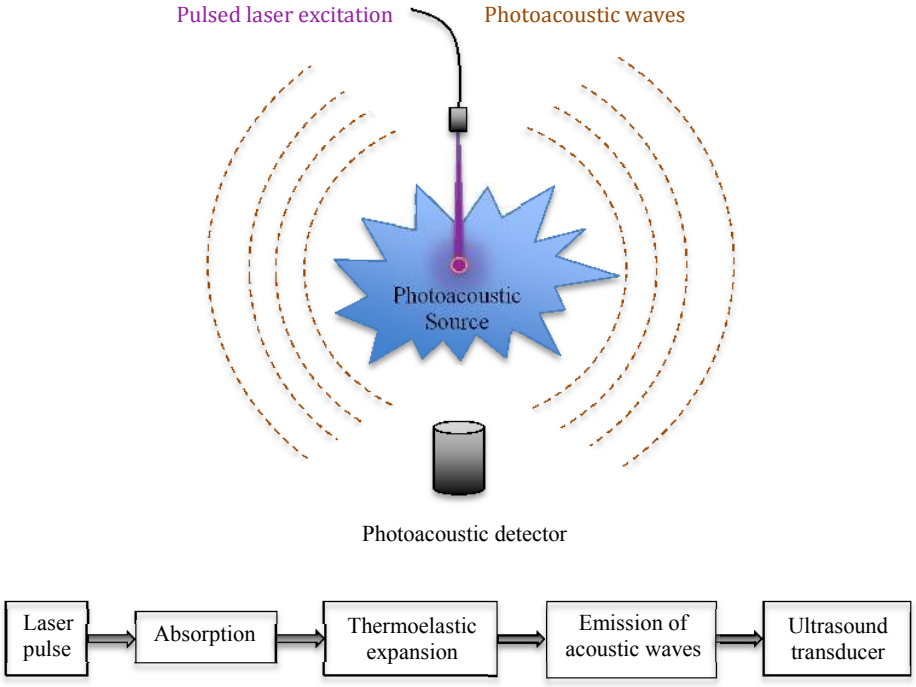

Figure 1.6 Schematic illustration of photoacoustic imaging.

To generate an acoustic wave efficiently, the light pulse must be in thermal and stress confinement. That is, the laser pulse must be shorter than both the thermal relaxation time (τ_{th}) and the stress relaxation time (τ_{s}), respectively described by **Eq. 1** and **Eq. 2** [79].

$$\tau_{th} = \frac{d_p^2}{4\kappa} \quad (1)$$

Where d_p (cm) is the characteristic linear dimension of the sample volume being heated (i.e., the size of the absorbing structure or the penetration depth of laser) and κ (cm^2/s) is the thermal diffusivity of the sample. Under thermal confinement, heat diffusion is negligible during the excitation pulse [75].

$$\tau_s = \frac{d_p}{\nu_s} \quad (2)$$

Where ν_s is the speed of sound in the sample (m/s). Under stress confinement, high thermoelastic pressure can be accumulated rapidly in the sample [75].

When both thermal and stress confinements are satisfied, the pressure rise, p, due to the thermo-elastic expansion can be described by **Eq. 3** [80].

$$p = \Gamma \mu_a \Phi \quad (3)$$

Where Γ represents the Gruneisen parameter, μ_a represents the absorption coefficient of the molecule (cm^{-1}), and Φ represents the laser fluence at the sample (J/cm^2). The Gruneisen parameter could be considered as the efficiency of converting the light energy to acoustic energy and is given by **Eq. 4** [80],

$$\Gamma = \frac{\beta \nu_s^2}{C_p} \quad (4)$$

Where β represents the thermal coefficient of volume expansion (K^{-1}), ν_s represents the speed of sound in medium (m/s), and C_p represents the specific heat capacity (J/(kg·K). From **Eq. 3**, we see that the pressure generated should be linearly related to the Gruneisen parameter, optical absorption coefficient, and the laser fluence. Since the Gruneisen parameter is relatively constant and laser fluence does not vary greatly within one sample, the detected pressure

should directly map the optical absorption of the sample. Although typically taken as valid, the assumption of constant laser fluence is not necessarily accurate below one transport mean free path (1 mm) due to the scattering and absorption of light into tissues. Much research has been investigated into accurately accounting for the variation in laser fluence [81, 82].

The generated photoacoustic wave also suffers from attenuation when propagating in a sample. Photoacoustic signal attenuation in a medium can be described by **Eq. 5** [75].

$$\mu = af^b \tag{5}$$

Where μ is the acoustic attenuation coefficient (*dB/cm*), a is a tissue dependent constant, *b* is another tissue dependent constant that typically in the range of 1.0-2.0, in many biological tissues b = 1.0 [83], *f* is the frequency of the ultrasound. Therefore, high frequency acoustic waves result in higher spatial resolution at the expense of imaging depth.

1.3.2 Photoacoustic microscopy

With the advent of the laser, computer, and ultrasonic transducers, the photoacoustic effect was primed for implementation as an advanced imaging technology. Photoacoustic imaging is capable of providing morphological features and functional information of optically absorbing molecules by a combination of time resolved acoustic detection and two-dimensional (2D) mechanical scanning along the x-y transverse sample [84]. Photoacoustic imaging is a hybrid of an ultrasound imaging modality with optical-absorption contrast and can provide high-resolution images in both the transverse and depth directions. Based on how the laser pulse is focused for generating photoacoustic images, photoacoustic imaging can be classified into acoustic-

resolution photoacoustic microscopy (AR-PAM) [13] and optical-resolution photoacoustic microscopy (OR-PAM) [85, 86]. Since this research exclusively uses AR-PAM to image samples, a detailed description of only AR-PAM will be described below while only a very brief description of OR-PAM will be given.

1.3.2.1 Acoustic-Resolution Photoacoustic Microscopy

The primary difference between AR-PAM and OR-PAM is the degree to which the incident light is focus on a sample. For AR-PAM, the acoustic focal width is narrower than the optical focus therefore the lateral resolution is afforded by the acoustic properties of the transducer. In many AR-PAM scenarios the optical spot size is often several times larger than the acoustic focus.

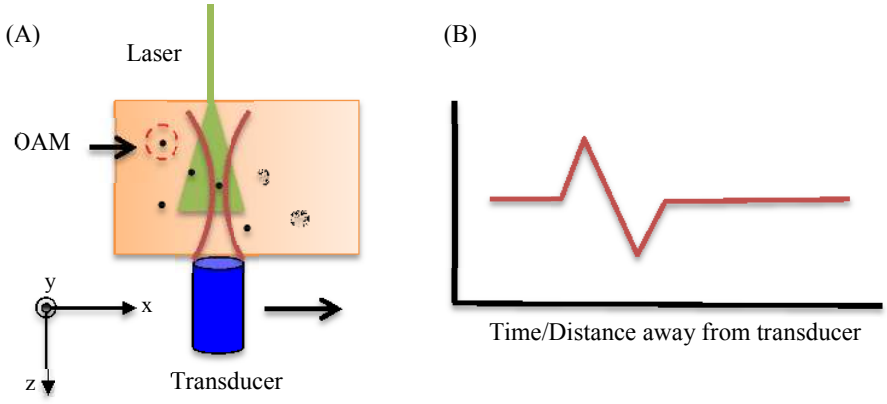

Figure 1.7 Schematic illustration of AR-PAM. (A) A typical B-scan of AR-PAM. OAM: optically absorbing absorber. (B) 'N'-shaped photoacoustic signal.

As depicted in **Figure 1.7A**, the light enters the medium and, in tissues and *in vivo* samples, nearly immediately starts to scatter. A focused ultrasound transducer must be used to separate signals in the illuminated volume. The transducer can then be laterally scanned across the sample in one dimension to form a 2D depth image, known as a B-scan. The transducer can also be

laterally scanned in a second dimension to form a 3D scan known as a C-scan. **Figure 1.7B** depicts the characteristic 'N'-shaped photoacoustic signal seen from optically absorbing structures. This 'N'-shape represents the compression and rarefraction of the material, while the width of the 'N' shape is determined by the geometry of the object under investigation.

Since AR-PAM uses loosely focused light to excite optically-absorbing molecules within a large volume and relies on an ultrasonic detector to separate photoacoustic signals generated within the illuminated area, the spatial resolution of AR-PAM systems is fully determined by the lateral resolution of the ultrasound transducer. For a single element, focused ultrasound transducer, the lateral resolution, $R_{L,AR}$, can be estimated with **Eq. 6** [13].

$$R_{L,AR} = 0.61\frac{\lambda_A}{NA_A} = 0.61\frac{v_s}{NA_A * f_A} \quad (6)$$

Where the constant 0.61 reflects the full width at half maximum (FWHM) of the acoustic focal spot in acoustic amplitude rather than the intensity detected by the ultrasonic transducer; λ_A and f_A are the central wavelength and frequency of the photoacoustic signal, respectively. NA_A is the numerical aperture of the ultrasonic transducer; v_s is the speed of sound in the medium.

The axial resolution is determined by the bandwidth of the detected photoacoustic signals rather than the confocal parameter [87]. Based on the assumption that the photoacoustic signal originating from a point target follows a Gaussian frequency profile, AR-PAM shares the axial resolution formula (see **Eq. 7**) with OR-PAM since the axial resolution is determined by the time of arrival of acoustic signal to ultrasound transducer [14].

$$R_{A,AR/OR} = 0.88\frac{v_s}{\Delta f_A} \quad (7)$$

Where v_s is the speed of sound in the medium; Δf_A is the photoacoustic signal bandwidth (proportional to its central frequency f_A). When photoacoustic signal bandwidth is much wider than the detection bandwidth, Δf_A can be approximated as the detection bandwidth of the ultrasonic transducer.

As with ultrasound imaging, there is a tradeoff between imaging depth and spatial resolution. photoacoustic waves with high frequency are attenuated faster than low frequency ones (see **Eq. 5**), therefore, photoacoustic signal bandwidth decreases with imaging depth, resulting in lower axial resolution at greater depths [88].

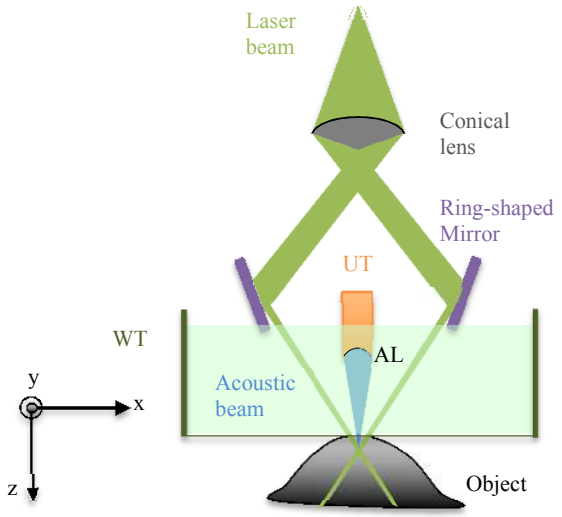

Figure 1.8 Schematic of the AR-PAM system. AL, acoustic lens; UT, ultrasonic transducer; WT, water tank.

One classic system for performing photoacoustic microscopy is dark-field AR-PAM [13, 89] depicted in **Figure 1.8**. the laser beam from a multi-mode fiber is passed through a conical lens to form a donut-shaped illumination that is loosely focused into the sample. The optical focus

coaxially overlaps the ultrasonic focus. The generated photoacoustic waves are focused by a concave acoustic lens and then detected by an ultrasonic transducer [13]. The advantages of this dark-field configuration are (1) elimination of the surface interference signals, such as signal from melanin in the epidermis of human skin), and (2) good confocal and coaxial alignment of the optical and acoustic beam [14].

1.3.2.2 Optical-Resolution Photoacoustic Microscopy

Many of the properties of OR-PAM are the same as AR-PAM such as the characteristic 'N'-shaped acoustic signal and the axial resolution being determined by the bandwidth of the signal. The key difference between these two techniques is that the lateral resolution is determine by the light spot size rather than the acoustic focal zone. This gives some interesting opportunities such as using an unfocused transducer to detect over large areas while moving the light source.

The lateral resolution of OR-PAM, $R_{L,OR}$, is derived by the focal spot size of the excitation light, since the optical focus is much tighter than acoustic focus [14]. This term is described by **Eq. 8**.

$$R_{L,OR} = 0.51\frac{\lambda_O}{NA_O} \tag{8}$$

Where the constant 0.51 reflects the FWHM of the optical focal spot in light intensity, λ_0 is the optical wavelength, and NA_0 is the numerical aperture of the optical objective.

One typical OR-PAM system is depicted in **Figure 1.9**. The nanosecond excitation light pulse is tightly focused into local areas of a sample by an optical microscope objective. An optical-acoustic beam combiner, composed

of a thin layer of silicone oil sandwiched by a right-angle prism and a rhomboid prism, is used for optical-acoustic coaxial and confocal alignment. It also provides optical transmission without acoustic reflection, attributing to the matched optical refractive indices and mismatched acoustic impedances between prism glass and silicone oil. Photoacoustic waves are focused by a plano-concave acoustic lens attached to the bottom of combiner and then detected by an unfocused ultrasonic transducer. Optical aberration is compensated by a correction lens positioned on the top surface of the right-angle prism [85, 86]. OR-PAM is limited to ~1 mm penetration depth in tissues due to light scattering. A similar setup is sometimes used in AR-PAM systems, however, in these cases the light is focused less tightly.

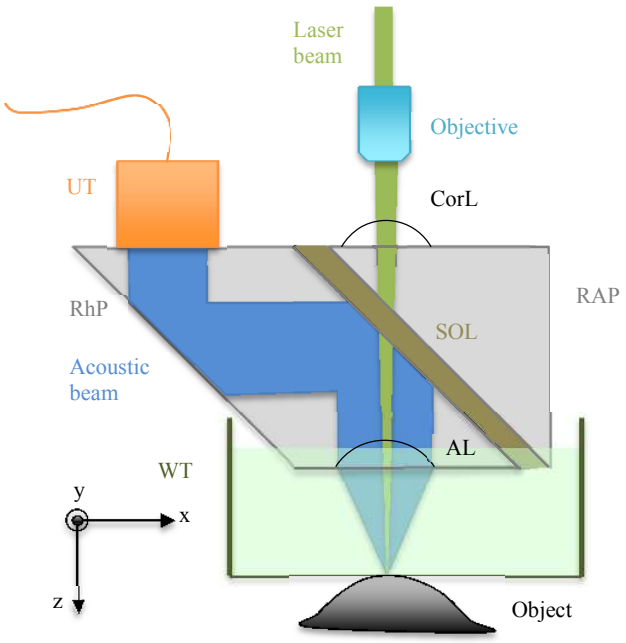

Figure 1.9 Schematic of the OR-PAM system. AL, acoustic lens; Corl, correction lens; RAP, right angled prism; RhP, rhomboid prism; SOL, silicone oil layer; UT, ultrasonic transducer; WT, water tank.

1.3.3 Applications of photoacoustic imaging

Photoacoustic imaging offers a unique non-invasive method to image reporter molecules with optical absorption contrast and high depth-to-resolution ratios. Essentially any samples with high optical absorption contrast will absorb some of the energy and emit an acoustic pressure wave when exposed to a pulsed laser beam. Since photoacoustic imaging depends on one-way propagation of light into samples and detection of minimally scattered acoustic signals, photoacoustic imaging is capable of imaging deeper tissues compared to the traditional optical imaging techniques. Photoacoustic imaging has proven to be a useful technology in various areas of biomedicine, including oncology, neurology, vascular biology, dermatology, cardiology and ophthalmology (reviewed in [15, 75, 88, 90, 91]). In the scope our research, only a few representative applications of genetically encoded molecular imaging were explored and are described in this thesis.

1.3.3.1 Photoacoustic imaging for endogenous chromophores

The predominant light absorbing molecules in biological tissues are hemoglobin and melanin. These endogenous contrast agents allow photoacoustic imaging to non-invasively study various biological processes *in vivo*. Due to the strong and unique absorption spectrum of hemoglobin (**Figure 1.10**) [92], photoacoustic imaging has been applied to study the microvasculature of animals [93]. The use of hemoglobin as a chromophore for photoacoustic imaging can offer us a convenient means to gain insight into the vasculature of tissues. It can also be used to research the growth of new blood vessels, which is especially useful in cancer research since the growth of

new blood vessels (angiogenesis) is substantially increased around tumors. There have been many photoacoustic studies examining cancer angiogenesis [86, 94].

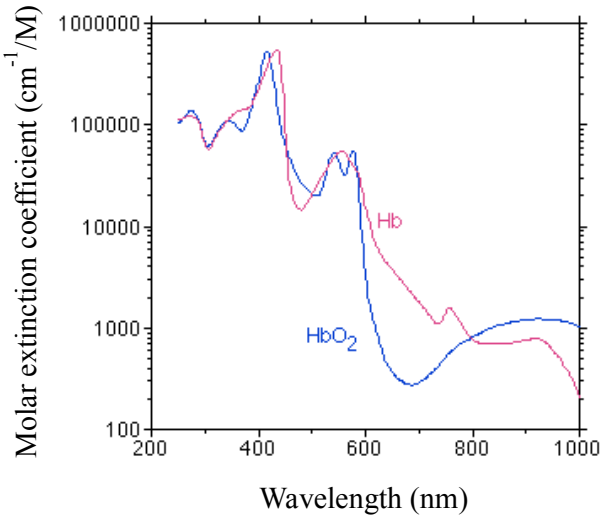

Figure 1.10 Optical absorption spectra of oxygenated and deoxygenated hemoglobin. Oxygenated hemoglobin and deoxygenated hemoglobin absorption spectra are depicted in blue and red lines, respectively.

Moreover, the variations of absorption spectra between hemoglobin in the oxygenated and deoxygenated states have been used to estimate blood oxygen saturation and oxygen consumption [95]. To determine the oxy- and deoxyhemolgobin concentration (C_{oxy} and C_{deoxy}, respectively) we can use the system of equations depicted by **Eq. 9**.

$$\begin{bmatrix} p_{\lambda_1} \\ p_{\lambda_2} \end{bmatrix} = \Gamma \Phi \begin{bmatrix} \varepsilon_{oxy_{\lambda_1}} & \varepsilon_{deoxy_{\lambda_1}} \\ \varepsilon_{oxy_{\lambda_2}} & \varepsilon_{deoxy_{\lambda_2}} \end{bmatrix} \begin{bmatrix} C_{oxy} \\ C_{deoxy} \end{bmatrix} \tag{9}$$

Where ε represents the extinction coefficient, C represents the concentration, the subscript *oxy* and *deoxy* represent oxyhemoglobin and deoxyhemoglobin, respectively, and the subscripts λ_1 and λ_2 represents two wavelengths of light. This equation also assumes that the sample only contains oxy- and deoxyhemoglobin. This equation can be derived from **Eq. 3** remembering that

$\mu_a = \varepsilon C$. Since the photoacoustic signal and fluence are measureable, the Gruneisen parameter is near constant for the two wavelengths, and the extinction coefficient are known from the literature, the concentration of oxyhemoglobin and deoxyhemoglobin can be found by solving the inverse problem. Finally, the oxygen saturation can be determined using these relative concentrations. This principle has been used in numerous publications [95] and has been used to estimate the concentration of various optically-absorbing molecules in a sample. The system of equations described by **Eq. 9** is easily extensible to different molecules and samples that contain more than two molecules, with the caveat that (at very least) the number of wavelengths used must match the number of components in the sample. Multi-wavelength imaging can therefore separate different components within a sample and allow the estimation of the molecular concentration.

Melanin is another principal endogenous absorber in biological tissues. Due to its strong and broad absorption, melanin has been explored extensively as a contrast agent for early melanosomes detection by photoacoustic imaging [13, 96]. Photoacoustic imaging has been successfully used to detect the circulation of melanoma cells in blood and longitudinally monitor melanoma growth in animals [97-99]. It has also been used to assess the spatial distribution of the melanoma cells in scaffolds for tissue engineering [100]. In addition, melanin is also an ideal contrast agent in the retinal pigment epithelium (RPE) for photoacoustic imaging, which is promising for both fundamental investigation and clinical diagnosis of eye diseases [101].

1.3.3.2 Photoacoustic imaging for exgenous chromophores

In addition to endogenous absorbers, exogenous genetically encoded

reporter genes also have been investigated for photoacoustic imaging. An exogenous genetically encoded reporter gene is incorporated into the genome of a tumor cell line and is produced either constitutively or under the control of a regulated promoter. The combination of reporter genes under control of a regulated promoter, and photoacoustic imaging, enables researchers to non-invasively investigate gene expression in live cells. For example, the expression of reporter gene lacZ in gliosarcoma tumor cells has been utilized in photoacoustic imaging [102, 103]. The β-galactosidase encoded by lacZ reporter gene can cleave the glycosidic linkage of the substrate X-gal (5-bromo-4-chloro-3-indolyl-β-D-galactoside) to create a blue product with high optical absorption. With the help of this blue contrast agent, the tumor cells and surrounding microvasculature can be observed by photoacoustic imaging [102]. As the primary enzyme responsible for expression of melanin in melanogenic cells, tyrosinase has also been used as a genetically encoded inducible reporter gene. Tyrosinase-expressing tumor cells can be differentiated from surrounding vasculature *in vivo* by photoacoustic imaging [104-106].

The discovery and development of genetically encoded GFP-like proteins has substantially aided the understanding of biological processes and opened new opportunities for development of new optical imaging modalities and new molecular imaging tools. Recently, fluorescent proteins were demonstrated to have potential as photoacoustic reporter molecules. Razansky et al. demonstrated that photoacoustic tomography could resolve tissue-specific expression of enhanced-GFP (EGFP), DsRed and mCherry fluorescent proteins several millimeters deep in tissues while maintaining 20-

100 μm resolution [17]. In 2012, an infrared fluorescent protein (iRFP) was used for photoacoustic imaging *in vivo* and shown to provide a significantly stronger photoacoustic contrast than conventional fluorescent proteins [107]. Although fluorescent proteins have great potential, most of them suffer from photobleaching upon exposure to pulsed laser energy and limited photostability. More importantly and detrimental to photoacoustic imaging is that the most commonly used fluorescent proteins have been optimized for high fluorescence quantum yield resulting in inefficient laser energy transduction into thermoelastic expansion necessary for photoacoustic imaging. Other GFP-like non-fluorescent chromoproteins have also been evaluated by photoacoustic imaging and compared with various fluorescent proteins [18]. It was shown that chromoproteins cjBlue and aeCP597 are more robust to laser-induced bleaching after repetitive laser exposures. Therefore, chromoproteins are more generally more photostable than fluorescent proteins, and can therefore serve as superior reporter molecules for photoacoustic applications.

1.4 Genetically encoded FRET-based biosensor

GFP-like proteins are widely used for engineering biosensors that allow researchers to study analyte (i.e., a small biomolecule) flux, enzyme activities, biological recognition, and signal transduction in live cells. Among the various designs of fluorescent protein-based biosensors, Förster (or fluorescence) resonance energy transfer (FRET)-based biosensors are the most widely utilized. Typically, the donor and acceptor fluorophores are fluorescent proteins, but some dark acceptors (i.e., chromoproteins) have also been utilized [25, 26, 44].

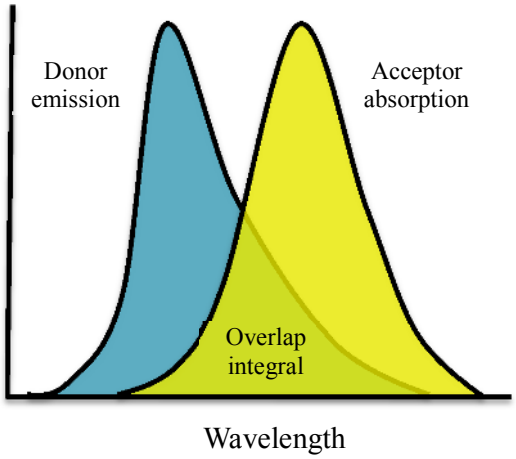

Figure 1.11 Schematic representation of FRET spectral overlap. A necessity for FRET is that donor emission (cyan) overlaps acceptor absorption spectrum (yellow).

1.4.1 Introduction to FRET

FRET is a non-radiative process of energy transfer based on dipole-dipole interaction between two fluorophore [108]. The donor fluorophore (D) in an excited electronic state may transfer its excitation energy to a ground state acceptor chromophore (A) if the donor emission spectral overlaps the acceptor absorption (**Figure 1.11**) and they are in close proximity [109]. This energy transfer is quantified by FRET efficiency, which is proportional to the amount of donor quenching. FRET does not require that the acceptor chromophore be fluorescent, but if it is, the phenomenon of sensitized acceptor emission can be observed. An advantage of sensitized emission from a fluorescent acceptor is that the emitted signal becomes a ratiometric signal. Generally speaking, it is easier to quantify ratiometric signals than intensiometric signals.

FRET efficiency is strongly dependent on the distance and orientation of donor and acceptor fluorophores (**Figure 1.12**) [109, 110]. As the distance between donor and acceptor decreases, the FRET efficiency increases. FRET is more efficient at closer distances, but significant FRET efficiency can

typically be achieved for distances of up to 10 nm, when using suitable fluorescent protein pairs. The orientation factor (κ^2) is generally assumed to constant and to have a value of 2/3, corresponding to random dipole orientations [110]. FRET efficiency is also dependent on the photophysical properties of donor and acceptor, including the donor quantum yield (Φ), acceptor extinction coefficient (ε), and the overlap between the emission profile of the donor and the absorbance profile of the acceptor. Other practical issues that can complicate FRET measurements are the sensitivity to protein environment changes (such as pH, temperature and halide ion concentration) and susceptibility to photobleaching [110].

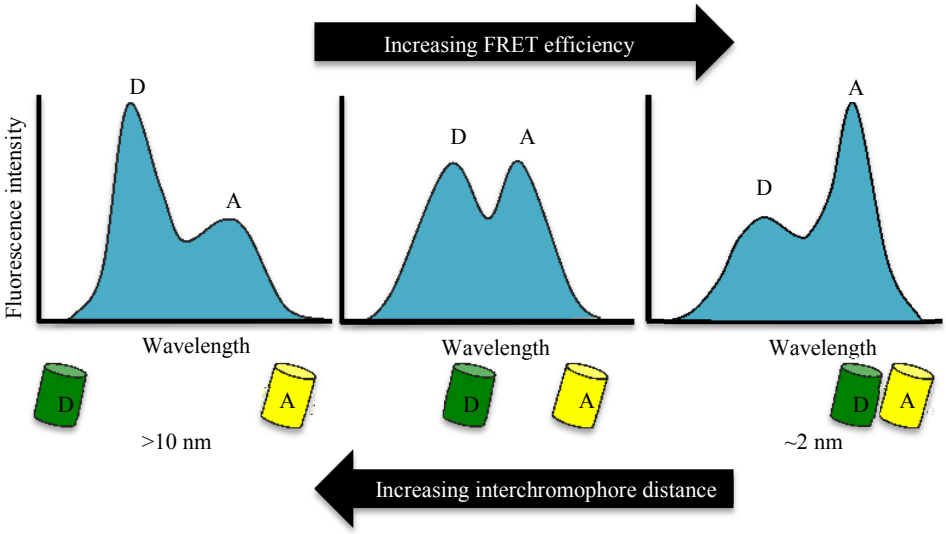

Figure 1.12 Schematic representation of emission spectra for a typical FRET type biosensor. As the distance between Donor (D) and Acceptor (A) decrease, the emission of acceptor increase.

1.4.2 Strategies to assemble FRET-based biosensor

The most commonly utilized FRET-based biosensor designs involve the fusion of molecular recognition domains to a pair of fluorescent proteins that have an appropriate spectral overlap. A summary of popular FRET-based biosensor design strategies is presented in **Figure 1.13**.

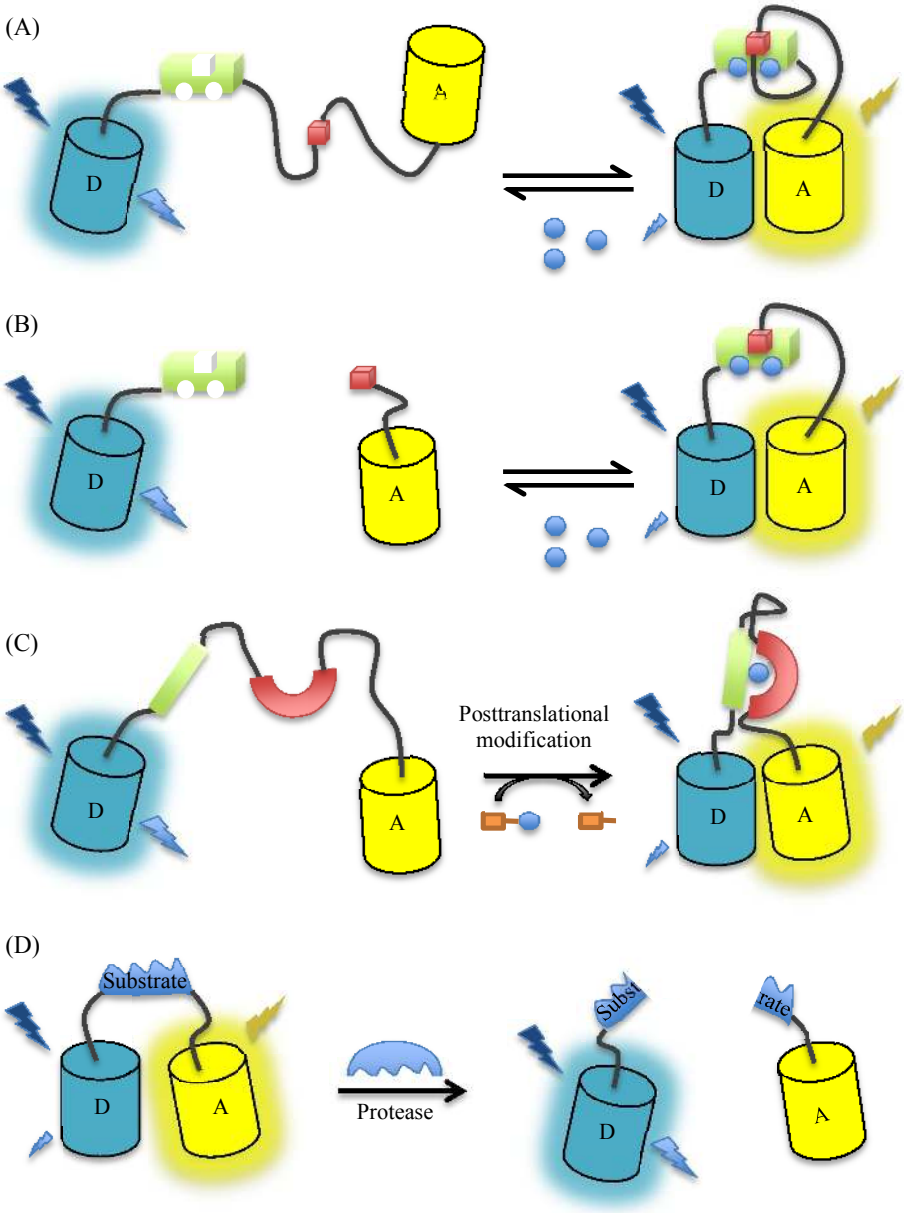

Figure 1.13 Fluorescent protein-based FRET biosensor design strategies. For all examples the cyan barrel is the donor (D) fluorescent protein and yellow barrel is the acceptor (A) fluorescent protein. (A) Intramolecular and (B) intermolecular biosensors for a small molecule (blue circle) induced protein-protein interaction. (C) Biosensors of enzyme activity. The blue circle depicts a chemical functionality that is installed into a substrate domain (light green ellipse) by specific enzyme. (D) Protease biosensors. Donor and acceptor fluorescent proteinss are linked by the protease-cleavable substrate.

In the first strategy, the biosensor is designed based of a small molecule dependent protein-protein interaction, either as an intramolecular single polypeptide biosensor (**Figure 1.13A**), or an intermolecular biosensor (**Figure**

1.13B). The most well known example of this type of strategy is the 'cameleon' Ca^{2+} biosensor [22, 111, 112]. The donor (e.g., CFP) and acceptor (e.g., YFP) fluorescent proteins are fused directly to Calmodulin (CaM) and M13 peptide, respectively. Upon binding, CaM/Ca^{2+} wraps around M13 peptide and bring donor and acceptor fluorescent proteins into much closer proximity, and thus increase the FRET efficiency [112]. The FRET efficiency of cameleon biosensors is highly sensitive to the concentration of Ca^{2+} in the live cells [113].

The second strategy takes advantage of conformational changes induced by post-translational enzymatic modification. A molecular recognition domain and a substrate are fused together with donor and acceptor fluorescent proteins (**Figure 1.13C**). After post-translational enzymatic modification (e.g., phosphorylation or glycosylation), the modified substrate binds to the molecular recognition domain, and results in a change in FRET efficiency attributed to distance and/or orientation changes. This design of biosensors is widely utilized for the study of enzymes such as GTPases [114] and kinases [115, 116].

In contrast to the first two strategies, the third strategy utilizes the loss of FRET response based on protease-substrate recognition. In this design, a peptide contains a protease cleavage substrate linked between two fluorescent proteins. Upon protease-substrate recognition, the protease cleaves the substrate and causes the separation of donor and acceptor fluorescent proteins (**Figure 1.13D**). This strategy was used in the first demonstration of FRET between blue fluorescent protein (BFP) and GFP joined by a trypsin-cleavable linker [117]. FRET-based protease biosensors have since been used to detect a

variety of proteases, such as caspase-3 [24, 118], caspase-6 [119], caspase-8 [120] in live cells.

In addition to these widely used FRET biosensors, a great number of other interesting designs of FRET-based biosensors have been developed and applied to specific research areas, such as mechanical tension biosensing [121] and ratiometric pH biosensing [122]. However, these alternative strategies are less commonly used than the three primary strategies described above.

1.5 The scope of the thesis

In this thesis, we present our efforts to engineer chromoproteins for photoacoustic imaging. The improved variants were then used as photoacoustic probes and dark acceptors of FRET-based biosensors, which were further applied in live cells to detect multiple dynamic activities.

Chapter 2 describes a novel method used to screen and evolve chromoproteins for enhanced photoacoustic properties. We devoted our efforts to evolve two chromoproteins, Ultramarine and cjBlue, using directed evolution combined with two distinct colony-based screening techniques: absorption-based screening and photoacoustic-based screening. After several rounds of evolution and screening, the best variants (t-Ultramarine 7.2 and cjBlue 7.1) with higher photoacoustic signal were characterized and used as genetically encoded probes for photoacoustic imaging.

Chapter 3 focuses on the implementation of the tandem dimer acceptor, t-Ultramarine 7.2, as the 'dark' acceptor in a FRET-based protease biosensor and a FRET-based Ca^{2+} biosensor. For protease biosensors, tandem dimer t-Ultramarine 7.2 was used as a dark acceptor, while a fluorescent protein (i.e., EGFP, mPapaya, or mRuby2) served as the donor. For comparison, protease

biosensors were also constructed using Ultramarine as a dark acceptor. We successfully detected protease caspase-3 activation in live cells. For Ca^{2+} biosensors, a cameleon-type Ca^{2+} biosensor (where the donor is tdTomato and the acceptor is t-Ultramarine 7.2) was constructed and applied for live cell imaging of Ca^{2+} dynamics.

The final chapter provides a summary of this work and proposes several future directions for the field of genetically encoded probes for photoacoustic imaging and application of dark acceptor-based FRET biosensors.

Chapter 2: A photoacoustic imaging based screening method for the directed evolution of chromoproteins

2.1 Introduction

Chromoproteins are GFP-like proteins with quantum yields that are so low that they are essentially non-fluorescent. Similar to DsRed [53], chromoproteins form a visible wavelength chromophore through a self-catalyzed modification of their own polypeptide sequences, ultimately conferring its host organism with a unique color. Since the chromophore is derived from the inherent protein sequence, coloration does not require a pigmented prosthetic group, which is often found in other chromoproteins [48]. Chromoproteins are distinguished from fluorescent proteins by their chromophore photochemistry; chromoproteins' chromophores effectively absorb photons, but cannot emit photons. The energy absorbed by chromoproteins' chromophores dissipates as heat through non-radiative relaxation, which can lead to a thermo-elastic expansion and generates an acoustic pressure wave, a phenomenon known as the photoacoustic effect. Acoustic waves generated by chromoproteins can be detected by ultrasound transducer [16, 107].

The research described in this chapter is a close collaboration with Dr. Roger J. Zemp group in Department of Electrical & Computer Engineering, University of Alberta, Edmonton, Alberta, Canada, T6G 2V4. All photoacoustic imaging is credited to Alexander Forbrich, a gradate student under the supervision of in Dr. Zemp, including Figures 2.2, 2.3, 2.4, 2.7, 2.8, 2.14, 2.15, 2.16 and the photoacoustic signal of proteins in Table 2.1 and 2.2. The directed evolution, primary absorption screening, protein purification, sample preparation for photoacoustic imaging and *in vitro* protein characterization were all performed by the author of this thesis (Yan Li).

Therefore, chromoproteins can be utilized as genetically encoded probes using photoacoustic imaging. Further, the photoacoustic signal intensity also can be used to make quantitative measurements of chromoprotein spectral properties, such as extinction coefficient (ε) and quantum yield (QY or Φ). Laufer et al. has demonstrated that chromoproteins cjBlue and aeCP597 provide high photoacoustic signal amplitude and exhibited low photobleaching, compared to fluorescent proteins, which are conventionally used as probes for live cell imaging [18].

Thus far, chromoproteins have been under-utilized as probes for live cell imaging. One limitation is that most of the known chromoproteins yet need to be optimized to make them a more attractive alternative class of proteins for live cell imaging. However, an appropriate directed evolution system must be established in order to improve the photoacoustic signal of chromoproteins *in vitro*. To engineer an optimized chromoprotein, we took inspiration from directed evolution strategies widely used for fluorescent proteins [123], to screen for chromoproteins exhibiting desired properties. The first requirement is the ability to screen large numbers, or a library, of chromoprotein mutants. We therefore, developed a novel colony-based photoacoustic screening method.

Ultramarine [44], a monomeric chromoprotein derived from Rtms5, was selected as a starting template for photoacoustic-based directed evolution. This protein was selected because it possesses several favorable attributes for photoacoustic imaging. First, Ultramarine has a relatively high extinction coefficient of 64,000 $M^{-1}cm^{-1}$, resulting in a strong absorption at 586 nm. Second, it has a very low fluorescent quantum yield (Φ = 0.001), which

translates to extensive non-radiative energy dissipation and thus contributes a strong photoacoustic signal. Third, Ultramarine is a monomer and the crystal structure of its precursor chromoprotein, Rtms5, has been solved [32], thus allowing some biochemical introspection of any results obtained. To test our directed evolution and screening system for different chromoproteins, cjBlue [39] was also subjected into the same evolution and screening as Ultramarine. Chromoprotein cjBlue also has a high extinction coefficient (ε = 66,700 $M^{-1}cm^{-1}$) and red-shifted absorption at 610 nm (Φ < 0.0001). X-ray crystallographic studies show cjBlue is a natural octamer [39].

We anticipated two main challenges in developing a system for chromoprotein directed evolution: (1) the photoacoustic signal amplitude produced by Ultramarine or cjBlue in a single *E. coli* colony was likely not large enough for photoacoustic imaging and (2) no existing method was established to screen for photoacoustic signals. Here we describe our efforts to overcome these challenges and establish a novel photoacoustic imaging-based chromoprotein screening method.

2.2 Results and discussion

2.2.1 Evaluation of chromoproteins and comparison with selected fluorescent proteins

To test whether chromoproteins were indeed more promising photoacoustic imaging than fluorescent proteins, we initially compared several fluorescent proteins (mCherry [123] and EYFP [25]), to a dark EYFP [25] and to several chromoproteins (Ultramarine [44] and cjBlue [39]). For each protein, we measured the absorption spectrum, extinction coefficient, quantum yield, photoacoustic signal-to-noise ratio (SNR), and photostability.

In comparison to fluorescent proteins, the chromoproteins exhibited more red-shifted absorptions. Ultramarine absorbs at wavelengths up to ~650 nm, while cjBlue absorbs at wavelengths up to ~670 nm (**Figure 2.1**). Red and near-infrared absorption peaks are very important to tissue imaging due to haemoglobin absorbance at lower wavelengths and less light scattering at longer wavelengths. **Table 2.1** tabulates the spectral characteristics of the fluorescent proteins and chromoproteins tested in this study. Although the extinction coefficients of Ultramarine and cjBlue are slightly lower than those of the fluorescent proteins, the quantum yield of chromoproteins is over two orders of magnitude lower than fluorescent proteins, which is one of possible factors confering greater than an order of magnitude greater photoacoustic signal. For example, EYFP (with the highest quantum yield tested, 0.61) produces the least photoacoustic signal, while Ultramarine with a low quantum yield (0.001) emits the strongest photoacoustic signal. Low quantum yield ensures a high non-radiative quantum yield; the absorbed energy is transformed to heat rather than a fluorescent emission, which is a requisite step for generating photoacoustic signals. For the photoacoustic imaging of purified fluorescent proteins and chromoproteins, SNR has been normalized to protein concentration and laser fluence for appropriate evaluation and comparison. The SNR of photoacoustic signals from chromoproteins tend to be much greater than the SNR from fluorescent proteins prior to any severe photobleaching.

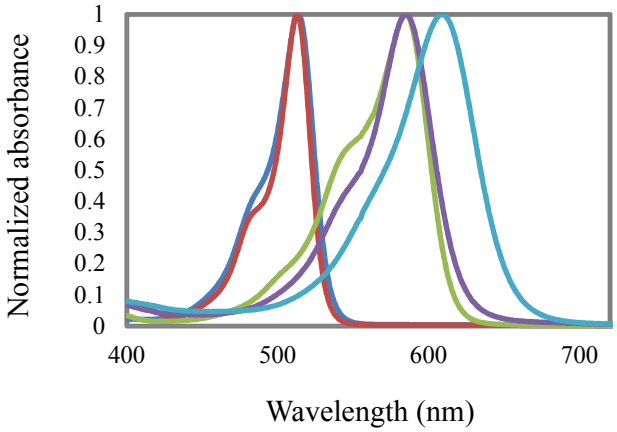

Figure 2.1 Normalized absorption spectra of fluorescent proteins (FPs) and chromoproteins (CPs). Dark YFP (blue). YFP (red), Ultramarine (purple), mCherry (light green) and cjBlue (cyan).

Table 2.1: Spectral characteristics of several FPs and CPs

Protein	λ_{ex} (nm)	ε (10^3 $M^{-1}cm^{-1}$)	Φ	SNR* (V/V)	SNR/ ε (10^{-6} (V/V)/$M^{-1}cm^{-1}$)
mCherry	587	72.0	0.22	3.2	44.0
EYFP	514	83.4	0.61	0.8	10.0
Dark EYFP	513	100.1	0.02	8.5	84.6
cjBlue	610	66.7	< 0.0001	63.8	956.0
Ultramarine	586	64.0	0.001	207.8	3250.0

*: SNR has been normalized by the molar concentration of each protein sample and fluence at each wavelength. Photoacoustic SNR data was collected by Alexander Forbrich.

In addition, it was found chromoproteins exhibit enhanced photostability relative to fluorescent proteins (**Figure 2.2**). After 1,000 laser pulses of 2.5 mJ/cm^2, the photoacoustic SNR from the fluorescent proteins decreased by 25-50% while the SNR decreased by less than 5% for the chromoproteins. This result agrees with the finding of Laufer et al. [18], who demonstrated that chromoproteins showed only minor photobleaching to pulsed laser illumination, in contrast to the majority of fluorescent proteins.

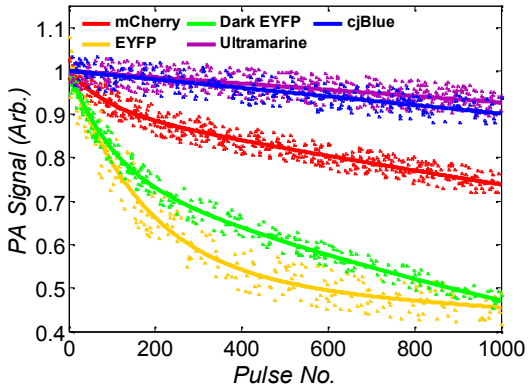

Figure 2.2 Photobleaching of purified proteins. EYFP (yellow, $\lambda_{exc.}$ = 514 nm), dark EYFP (green, $\lambda_{exc.}$ = 513 nm), mCherry (red, $\lambda_{exc.}$ = 587 nm), Ultramarine (purple, $\lambda_{exc.}$ = 586 nm), and cjBlue (blue, $\lambda_{exc.}$ = 610 nm) proteins. The photoacoustic signal (normalized to molar concentration and laser fluence) decays exponentially for the fluorescent proteins while remains constant for the chromoproteins. Figure was prepared by Alexander Forbrich.

The photoacoustic spectra of chromoprotein-producing *E. coli* cells were compared with the absorption spectra of the purified proteins (**Figure 2.3**). For both Ultramarine and cjBlue, the photoacoustic spectra are in good qualitative agreement with the absorption spectra.

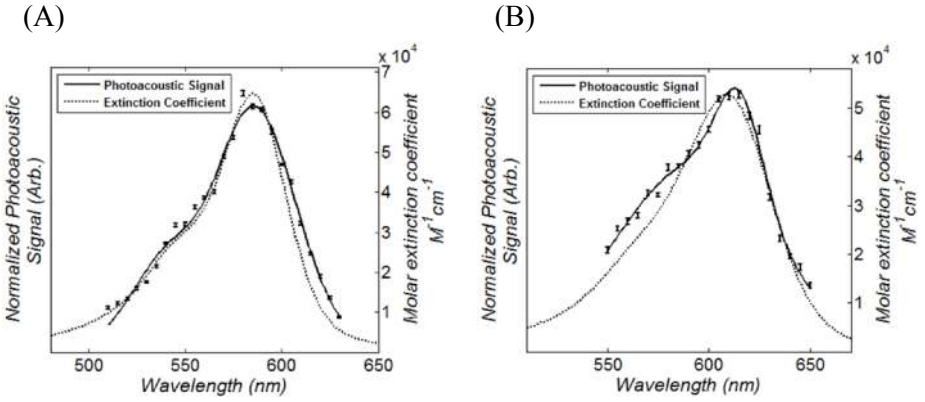

Figure 2.3 Comparison of the photoacoustic spectrum (solid lines) to the absorption spectrum (dashed lines) of Ultramarine (A) and cjBlue (B). Figure was prepared by Alexander Forbich.

To verify the potential of chromoproteins as reporter molecules to differentiate tissues and blood, a series of B-scan images at different

wavelengths were taken and subsequently assessed by a least squares demixing algorithm. PBS, resuspended *E. coli* cells producing either cjBlue or Ultramarine, and blood were sealed in four separate tubes and then subjected to photoacoustic B-scan image under water (**Figure 2.4A**). The average maximum photoacoustic signals within each tube at different wavelength are depicted in **Figure 2.4B**. The photoacoustic spectra matched the absorption spectra accurately (compare **Figure 2.4B** with absorption spectra in **Figure 2.3** and **Figure 1.10**). **Figure 2.4C** demonstrated that there was accurate differentiation of cjBlue from blood; however, crosstalk existed between the Ultramarine and blood tubes which may attributed to similarity of the absorption spectra of Ultramarine and blood beyond 585 nm. Given the characteristics of the transducer, we can estimate that the minimal number of cells required to give 3 V/V SNR at the ANSI (American National Standards Institute) safety limit of ~20 mJ/cm^2 (for visible light) as 50-3,000 cells per voxel. This is similar to Razanksy et al. [17] who demonstrated that the minimum number of cells is ~10^3 for imaging DsRed-expressing HeLa cells.

For the chromoproteins cjBlue and Ultramarine, the red-shifted absorption peaks, high photoacoustic signals, enhanced photostabilities and good spectral demixing capabilities make them very promising candidate probes for photoacoustic imaging. Imaging the purified chromoproteins at the ANSI safety limit of ~20 mJ/cm^2 enables us to detect protein concentrations of 180 nM and 588 nM for Ultramarine and cjBlue, respectively, with 3 V/V SNR. These concentrations agree to within an order of magnitude with Li et al. [102], who demonstrated 515 nM sensitivity of the blue product from the LacZ gene embedded 5 mm in tissue.

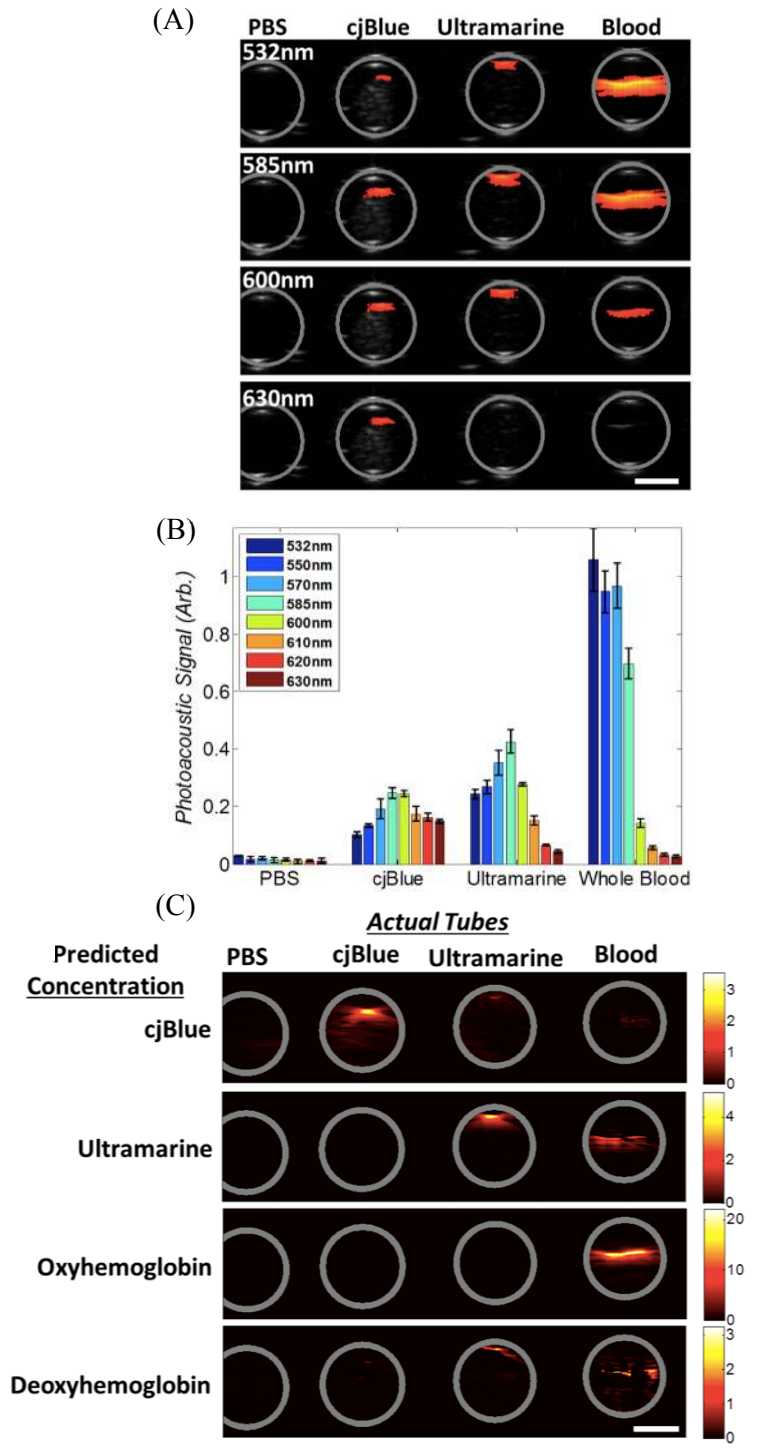

Figure 2.4 Multi-wavelength B-scan studies of tubes containing (from left to right) PBS, cjBlue or Ultramarine *E. coli* cells (~10^9 cells/mL), or heparinized rat blood. (A) Interlaced ultrasound (gray) and photoacoustic (orange) B-scans at select wavelengths. (B) Average maximum photoacoustic signal within each tube. C) Relative concentration of each sample using a least-squares demixing algorithm on each pixel. Scalebars represents 1mm. Figure was prepared by Alexander Forbrich.

2.2.2 Directed evolution and characterization of chromoproteins

Since our initial data demonstrated chromoproteins are superior to fluorescent proteins as genetically encoded probes for photoacoustic imaging, we next investigated the use of directed evolution to evolve chromoproteins for optimized photoacoustic characteristics. To achieve this goal, we subjected the Ultramarine and cjBlue to iterative rounds of mutagenesis and screening in which each round involved creating a library of gene mutants by error-prone PCR [67, 124] followed by two distinct colony-based screening techniques (**Figure 2.5**). In each round of evolution, approximately 5000 colonies were screened and approximately 5 to 10 variants were selected for further propagation and mutagenesis. The mixture of genes encoding these top variants was used as the template for subsequent rounds of library generation and screening. In the first several rounds, an absorption-based primary screening was utilized to improve the expression and rate of maturation of Ultramarine and cjBlue. The colonies with darkest color (20 to 30) were manually picked and their absorption spectra were collected. The strongest absorbing variants (5 to 10) were selected as template for next round. In the 4^{th} and 3^{rd} rounds of evolution of Ultramarine and cjBlue, respectively, 10 absorption-enhanced clones were chosen and plated on agar plate and further subjected to colony-based photoacoustic screening. The Ultramarine variant (numbered as 4.30) (**Figure 2.6A**) and cjBlue variant (numbered as 3.5) (**Figure 2.6B**) with both highest absorption and photoacoustic signal were used as templates for continuing directed evolution combined with direct photoacoustic imaging-based screening.

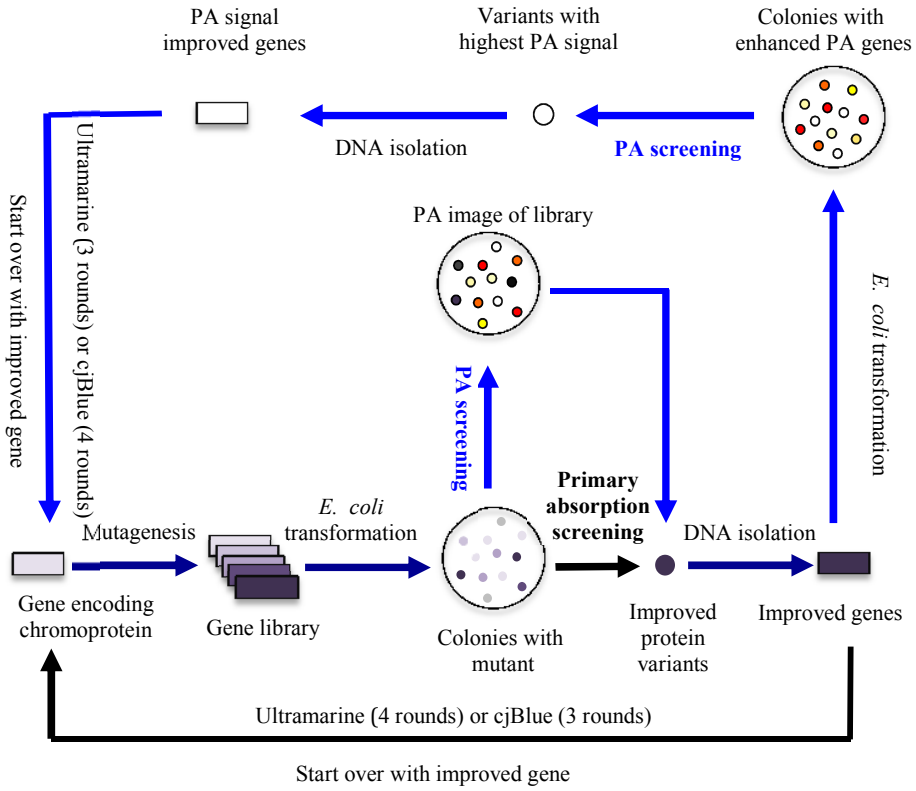

Figure 2.5 Schematic procedure of directed evolution of chromoprotein Ultramarine or cjBlue. Absorption screening-based directed evolution procedure is exhibited by dark blue and black arrow direction. Photoacoustic (PA) imaging screening-based directed evolution procedure is represented by dark blue and blue arrow direction.

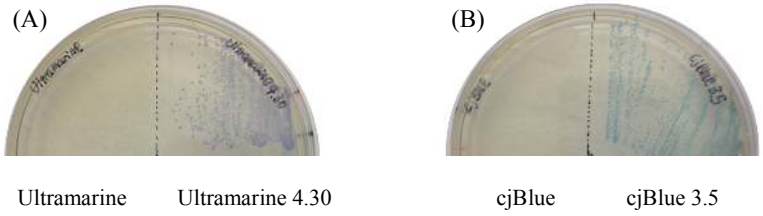

Figure 2.6 Comparison of *E. coli* expressing Ultramarine (left) with Ultramarine 4.30 (right) (A) and cjBlue (left) with cjBlue 3.5 (right) (B).

Before photoacoustic signal-based screening, a layer of agar was overlaid on the colonies, since the screening procedure occurs in a water tank. The thickness of overlay agar was just sufficient to cover the colonies. **Figure 2.7** depicts a schematic of the system for photoacoustic imaging. The colonies on

the agar plate were illuminated by a Nd:YAG laser uniformly. Chromoproteins expressed in *E. coli* colonies absorbed the energy and generated the photoacoustic signal, which is subsequently detected by the transducer.

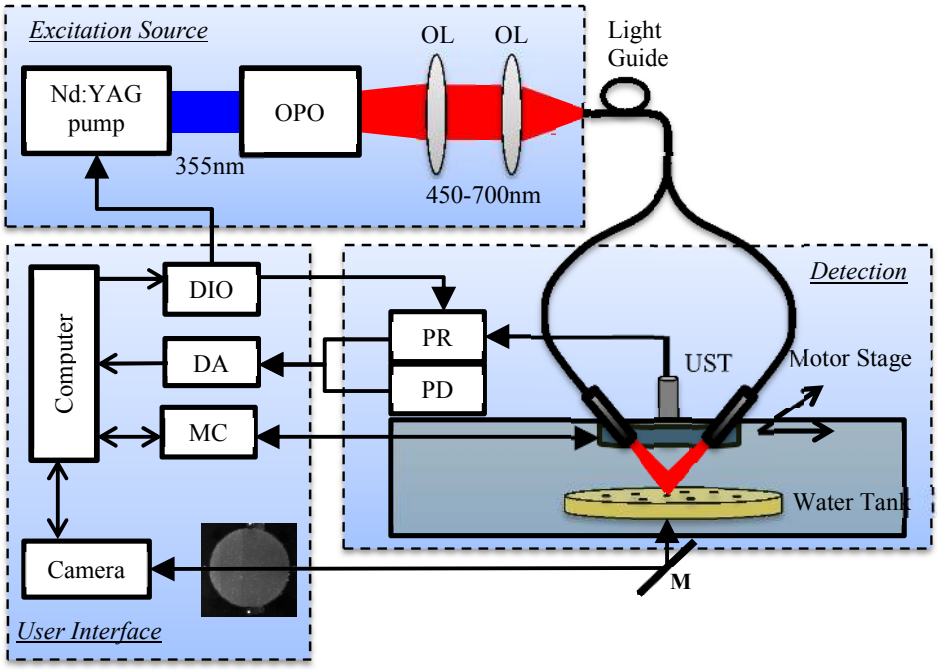

Figure 2.7 Schematic system of photoacoustic imaging. OPO, optical parametric oscillator; OL, objective lens; UST, ultrasound transducer; PD, photodiode; PR, pulser-receiver; DIO, digital input-output card; DAQ, data acquisition card; MC, motor controller; M, mirror. Figure was prepared under the guidance of Alexander Forbrich.

In the photoacoustic-based screening, single colonies were located using a camera (**Figure 2.8A**), the single element transducer was automatically positioned overtop the colony, and laser-induced photoacoustic signals were visualized on the computer monitor. The result of imaging one plate of library variants is presented in **Figure 2.8B**, where the color spectrum of black-red-yellow-white represents increasing photoacoustic signal intensity. The results from random mutagenesis demonstrate most of variants harbor detrimental mutations represented by the black dots; however, a few variants have the

desired phenotype of high photoacoustic signal levels. To account for variations in laser fluence between plates imaged on different days or weeks and to select the 'best' enhanced variant, the selected variants were imaged and screened together on a single plate (**Figure 2.8C**).

After the 7th round of evolution of both Ultramarine and cjBlue, we sequenced the variants with the highest photoacoustic signal. Ultramarine-N113S/T116I/F148V/R159H/K203R (**Figure 2.9**) is designated as Ultramarine 7.2 and cjBlue-M40V/E41V/D111V/N168S (**Figure 2.10**) is designated as cjBlue 7.1.

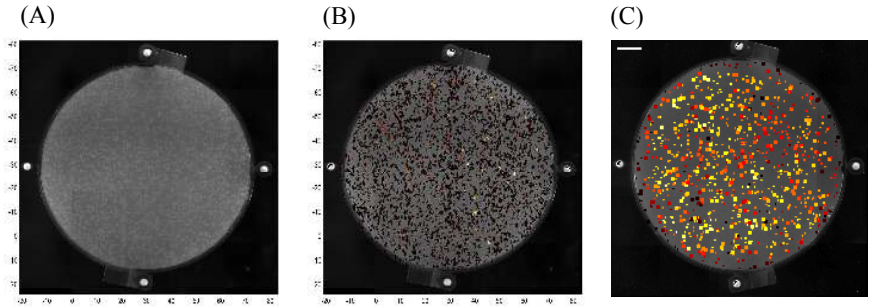

Figure 2.8 Photoacoustic imaging-based screening for directed evolution of Ultramarine. (A) Camera image of library plate; (B) Photoacoustic image of library plate; (C) Photoacoustic image of selected enhanced variants. The colorful dots represent the photoacoustic signal intensity, using a black-red-yellow-white color scheme to show increasing photoacoustic signal intensity. photoacoustic imaging is credit to Alexander Forbich.

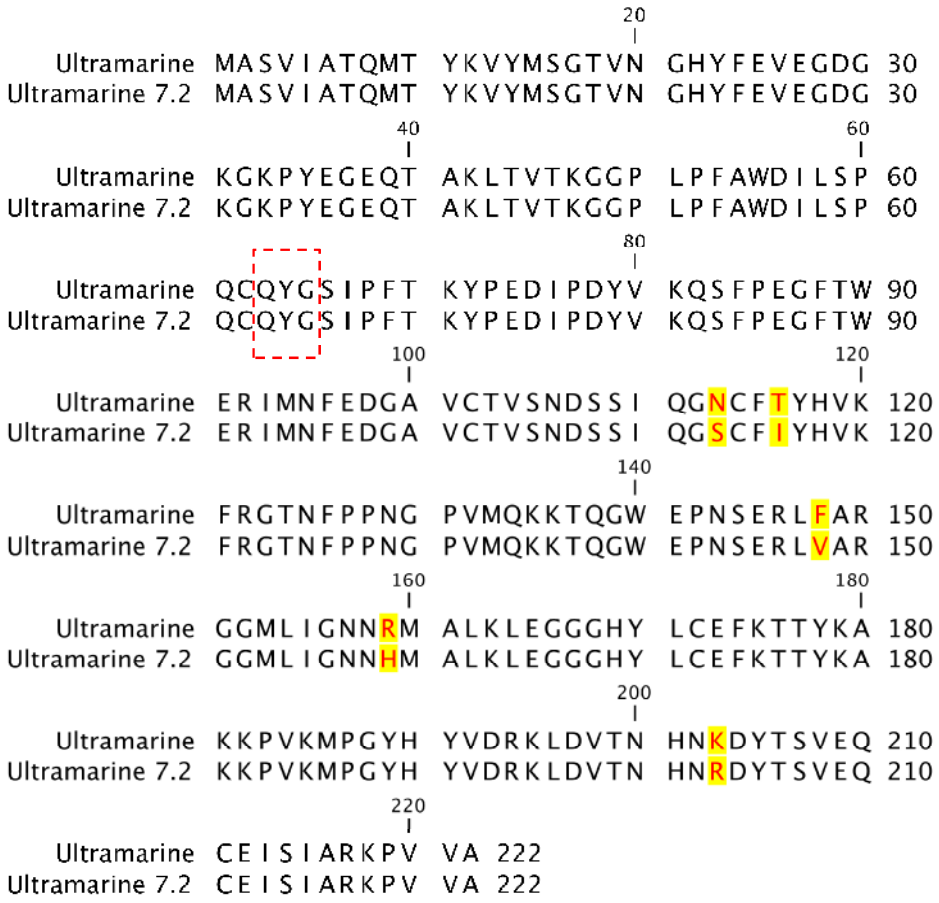

Figure 2.9 Sequence alignment of Ultramarine and Ultramarine 7.2. Substitutions in Ultramarine 7.2, relative to Ultramarine, are represented as red text on a yellow background. The chromophore forming residues are highlighted by red dash line in this alignment.

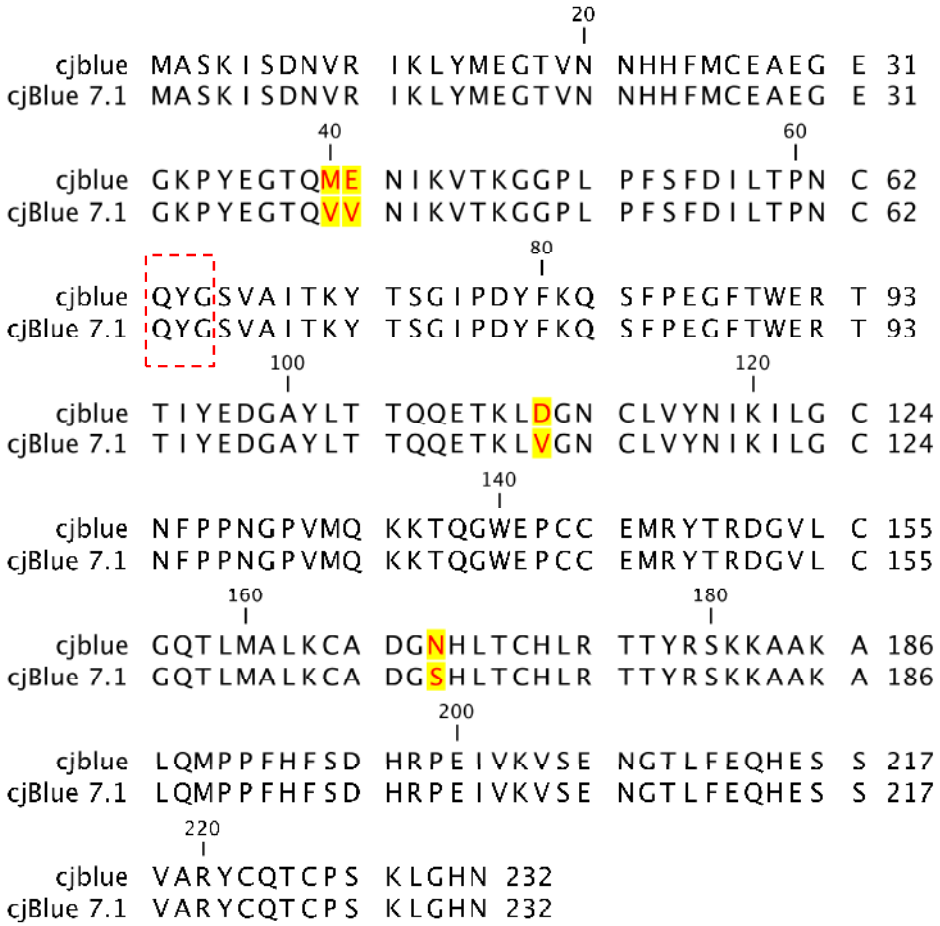

Figure 2.10 Sequence alignment of cjBlue and cjBlue 7.1. Substitutions in cjBlue 7.1, relative to cjBlue, are represented as red text on a yellow background. The chromophore forming residues are highlighted by red dash line in this alignment.

Since Ultramarine was derived from Rtms5, the X-ray crystal structure of Rtms5 was utilized to analyze and interpret the mutations (**Figure 2.11A**). All five mutations were found to correspond to residues that have their side chains directed towards the outside of the protein. Of these mutations, the one at position 159 has the most dramatic effect, since it is in the dimerization interface of Ultramarine [44]. Substitution R159 to H159 results in the conversion of a polar interface to a more apolar interface. This change is sufficient to cause the originally monomeric Ultramarine to revert to a dimeric form (**Figure 2.13A**). We later engineered the dimeric Ultramarine 7.2 into a

tandem dimer form (t-Ultramarine 7.2) that is effectively monomeric (**Figure 2.12**).

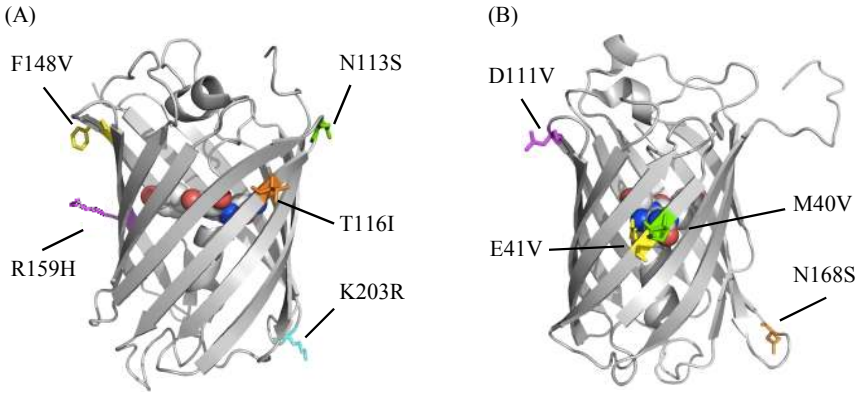

Figure 2.11 Location of substitutions in Ultramarine 7.2 and cjBlue 7.1 that were introduced during the directed evolution process. The X-ray crystal structure of Rtms5 (PDB ID 1MOU) is used here to represent Ultramarine (A). The monomeric cjBlue subunit is shown in B (PDB ID 2IB5).

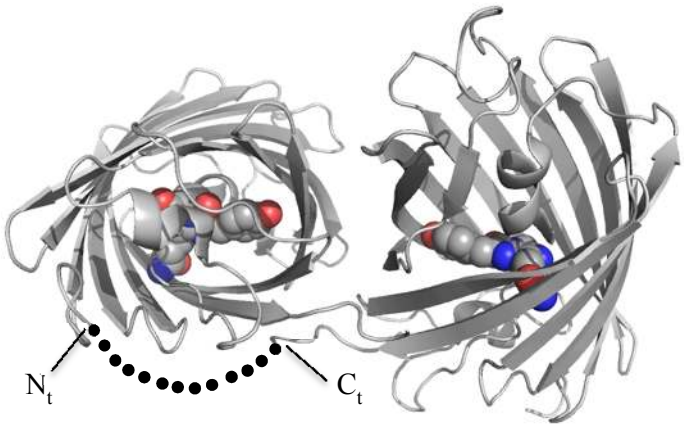

Figure 2.12 Graphical representation of t-Ultramarine 7.2. The X-ray crystal structure of Rtms 5 (H146) variant (PDB ID 2P4M) in high PH [57] is used here to represent Ultramarine 7.2. The intersubunit linker (13 residues--SCSGTGSTGSGSS) between N-terminal (N_t) and C-terminal (C_t) present in t-Ultramarine 7.2 shown as a purple dotted line.

Of the 4 mutations in cjBlue (**Figure 2.11B**), one is internal to the β-barrel (E41V) and three are surface mutations (M40V/D111V/N168S), which may facilitate the folding and maturation of the chromophore. These mutations did not change the protein from its octameric oligomerization state (**Figure 2.13B**). Compared to the Ultramarine and cjBlue precursors, the variants

(Ultramarine 7.2, t-Ultramarine 7.2 and cjBlue 7.1) exhibit much higher photoacoustic signal (see Chapter 2.2.3). However, the exact mechanism by which these mutations cause enhancement of photoacoustic signal is unclear.

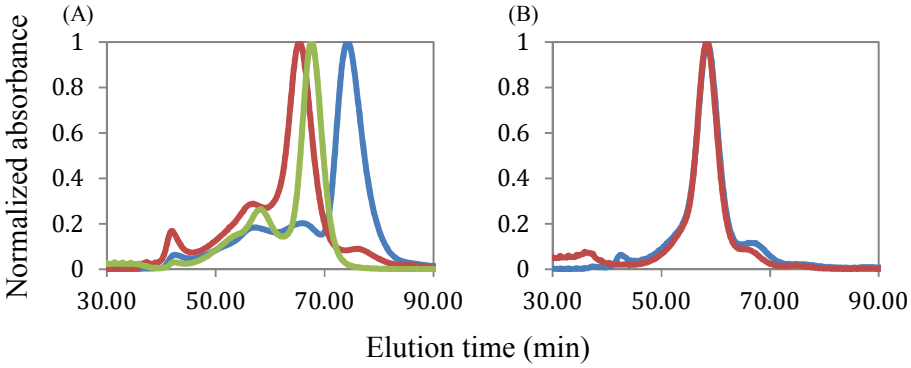

Figure 2.13 Characterization of the oligomeric structure of chromoproteins. (A) Ultramarine (blue), Ultramarine 7.2 (red) and t-Ultramarine 7.2 (light green) by size-exclusion chromatography. (B) cjBlue (Blue) and cjBlue 7.1 (red). Proteins purified by Ni-NTA chromatography were subjected to gel filtration chromatography on a HiLoad 16/60 Superdex 75 pg gel filtration column at 280 nm.

A limitation to the colony-based photoacoustic screening method is our inability to control the 'flatness' of the agar, especially around the edges where the meniscus forms. This causes a decrease in photoacoustic signal as seen around the edges of the plate (**Figure 2.8C**), as the colonies are out of the focal plane. This could be resolved by using a third axis and placing the transducer based on the time-of-flight of acoustic signals; however, we did not find this necessary since after many rounds of evolution the likelihood of detecting the best variant was very high.

2.2.3 *In vitro* spectral and photoacoustic characterization of chromoproteins

As described in the previous section, we used directed evolution to improve the photoacoustic signal of chromoproteins. Several improved

variants of both Ultramarine and cjBlue were identified after several rounds of screening. To attempt to determine the changes in spectral properties causative of enhanced photoacoustic signals we characterized Ultramarine 7.2, t-Ultramarine 7.2 and cjBlue 7.1 *in vitro* (**Table 2.2** and **Figure 2.14**). Both Ultramarine and cjBlue variants exhibit improvements in photoacoustic SNR. A 1.9-fold increase in photoacoustic SNR was seen in Ultramarine 7.2 with 27% increase extinction coefficient and at least a 2-fold lower quantum yield. Variant t-Ultramarine 7.2 had 4.3-fold greater photoacoustic signal with more than 3-fold higher extinction coefficient and a 2-fold lower quantum yield than Ultramarine while the absorption spectrum remained unchanged. Compared to cjBlue, variant cjBlue 7.1 had over 2-fold increase in photoacoustic signal, a slight blue shift, and no substantial changes in other spectral characteristics.

Table 2.2 Spectral characteristics of CPs and their enhanced variants

Protein	λ_{ex} (nm)	ε* ($10^3 M^{-1}cm^{-1}$)	Φ*	Relative SNR
Ultramarine	586	64.4	0.0002	1.0
Ultramarine 7.2	587	81.5	< 0.0001	1.9
t-Ultramarine 7.2	587	203.4	< 0.0001	4.3
cjBlue	610	52.7	< 0.0001	0.33
cjBlue 7.1	603	56.6	< 0.0001	0.70

* The published extinction coefficient of Ultramarine and cjBlue are 64000 $M^{-1}cm^{-1}$ and 66700 $M^{-1}cm^{-1}$ respectively [39, 44]. The published quantum yield of Ultramarine is 0.001 [44]. Relative SNR was normalized and compared with photoacoustic signal of Ultramarine. SNR data was collected by Alexander Forbrich.

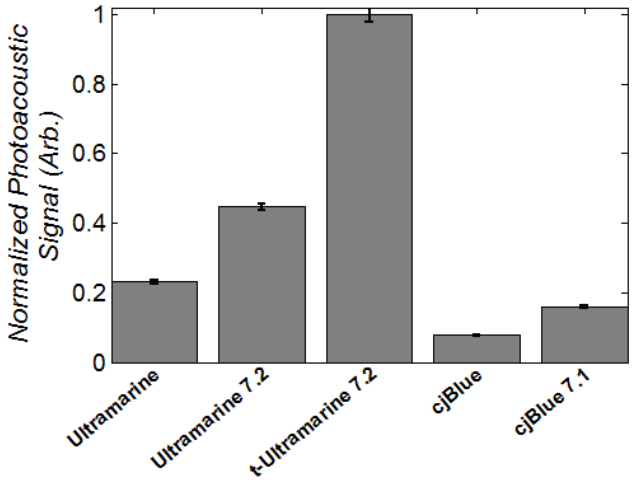

Figure 2.14: Photoacoustic signal-to-noise ratio (SNR) comparison of Ultramarine, cjBlue and their improved variants. Proteins purified by Ni-NTA chromatography were subjected to photoacoustic analysis. Figure was prepared by Alexander Forbrich.

To verify the similarity of the photoacoustic spectra between the precursor chromoproteins and the improved variants, we performed multi-wavelength photoacoustic studies (**Figure 2.15**). With both chromoproteins, the photoacoustic spectra of both the variants and the precursors resemble each other, as well as, the absorption spectra.

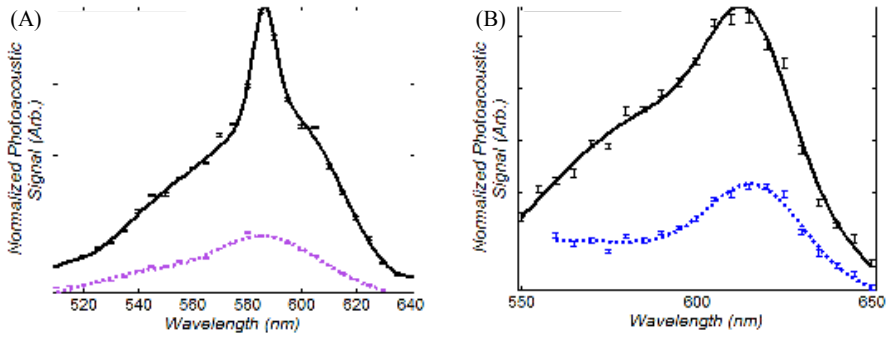

Figure 2.15: Photoacoustic spectrum comparison of purified Ultramarine, cjBlue and their improved variants. Proteins purified by Ni-NTA chromatography were subjected to photoacoustic imaging. (A) Ultramarine (purple dash) and t-Ultramarine (black line) are detected from 520 nm to 640 nm. (B) cjBlue (blue dash) and cjBlue 7.1 (black line) are monitored from 550 nm to 650 nm. Figure was prepared by Alexander Forbrich.

2.2.4 *In vivo* photoacoustic characterization of chromoproteins

To demonstrate the potential application of chromoproteins *in vivo*, *E. coli* cell pellets expressing Ultramarine and t-Ultramarine 7.2 were separately injected into the ear of a rat. Multi-wavelength imaging was conducted to compare photoacoustic SNR *in vivo* and assess the spectral unmixing potential of the chromoproteins in order to distinguish their signal from blood. **Figure 2.16** exhibits the results of spectral unmixing of Ultramarine and t-Ultramarine 7.2. The original Ultramarine was difficult to detect compared with blood in terms of SNR and unmixing of the signals had mediocre results.

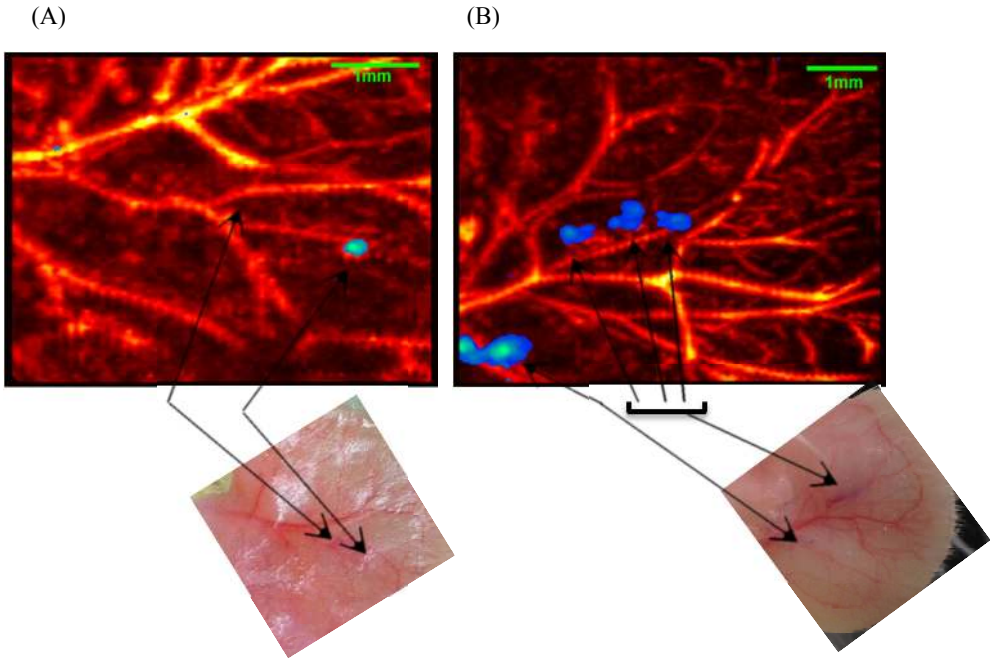

Figure 2.16: *In vivo* photoacoustic imaging of Ultramarine (A) and t-Ultramrarine 7.2 (B) *E. coli* pellets injected directly into the ear of a rat. Spectral demixing of the ultramarine from blood was conducted and a threshold was placed on the estimated concentration of ultramarine to overlay the ultramarine (in blue) overtop the blood (in red). Microscopy was used to verify the ultramarine location. Figure was prepared by Alexander Forbrich.

To minimize the noise, the threshold of detection for the original Ultramarine was relatively high. For the improved variant t-Ultramarine 7.2, the SNR was much higher and unmixing accurately determines the site of

injection. The threshold of detection could be set lower without being hindered by noise. Both microscopy and visual inspection were used to verify the site of injection.

2.3 Conclusion

We present a novel method to screen and evolve genetically-encoded chromoproteins with enhanced photoacoustic characteristics. Chromoproteins were found to generate large photoacoustic signals and had improved photostability relative to other fluorescent proteins. For this reason, chromoproteins were selected as ideal candidates for directed evolution for our photoacoustic screening system. After several rounds of screening, we achieved 2- to 4-fold improvements in photoacoustic signal, which was attributed to a higher extinction coefficient, lower quantum yield, and possibly due to protein structure-dependent changes in the Gruneisen parameter (Γ). We believe this screening technique will open many avenues for development of improved photoacoustic imaging reporter molecules and accelerate improvements in deep-tissue, non-invasive, *in vivo* imaging studies.

2.4 Materials and methods

2.4.1 General methods and materials

All synthetic DNA oligonucleotides used for cloning and library construction were purchased from Integrated DNA Technologies (Coralville, IA). Miniprep plasmid DNA, polymerase chain reactions (PCR), restriction enzyme digestion, ligation and agarose gel electrophoresis were performed according to Sambrook et al [125]. *Pfu* DNA polymerase was obtained from Fermetnas used for regular PCR and *Tag* polymerase was purchased from New England Biolabs used for error-prone PCR. All restriction enzymes were

obtained from Fermentas or New England Biolabs. T4 DNA ligase was obtained from Invitrogen or Life Technologies. PCR and digestion products were purified with the QIAquick gel extraction kit (QIAGEN, Valencia, CA) or GeneJET gel extraction kit (Fermentas) according to the manufacturer's instructions. All sequencing was performed at University of Alberta Molecular Biology Service Unit (MBSU) or University Core DNA Services at University of Calgary.

2.4.2 Random mutagenesis and library creation

Ultramarine and cjBlue, amplified from vector Ultramarine (kindly provided by Dr. Mark Prescott) in pQE9N (Qiagen) [44] and cjBlue (kindly provided by Dr. Atsushi Miyawaki) [39] in pRSET-B (Invitrogen) respectively, were used as the initial templates for the construction of genetic libraries. Random mutagenesis was performed by error-prone PCR as described [124]. Full-length gene libraries were digested with XhoI/HindIII (Fermetas) and ligated into similarly digested pBAD/His B plasmid (Invitrogen) with T4 DNA ligase (Invitrogen). Plasmid libraries were expressed in *E. coli* strain DH10B (Invitrogen) on LB (Luria-Bertani) agar plates supplemented with 0.1 mg/mL ampicillin and 0.02% L-arabinose at 37 °C overnight. Freshly prepared liquid 0.2% agar (~50 °C) was overlaid on the top of colonies prior to photoacoustic screening and allowed to cool.

2.4.3 Primary absorption screening

E. coli colonies expressing the Ultramarine or cjBlue libraries were grown on 10 cm Petri dishes. Top 20-30 colonies with darkest color were manually picked into 4 mL LB media supplemented with 0.1 mg/mL ampicillin and 0.02% L-arabinose and incubated overnight. Crude protein

extracts were obtained by taking advantage of B-PER Protein Extraction Reagent (Pierce/Thermo Scientific). 100 μL crude protein extracts were subject to absorption test and spectra (400-800 nm wavelength scan) were recorded by a DU-800 UV-visible spectrophotometer (Beckman). After absorption maximum comparison, 5-10 improved variants were picked and used as template for next round mutagenesis.

2.4.4 Photoacoustic imaging screening

After several rounds of primary absorption screening (4 rounds for Ultramarine and 3 rounds for cjBlue), 5-10 variants of each chromoprotein with the highest absorptions were picked and further subjected to photoacoustic image-based screening. A schematic of the photoacoustic imaging experimental setup is represented in **Figure 2.4**. A 10 Hz, Q-switched Nd:YAG laser (SLIII-10, Continuum) and an optical parametric oscillator (SL OPO Plus, Continuum) were utilized to create light with wavelengths extending from 450 to 700 nm. The generated light was coupled into a light guide (CeramOptec Industries, 900 fibres [185 µm core diameter, 200 µm cladding diameter, 250 µm jacket diameter], NA = 0.26/0.37 $\pm$ 0.02) with one input and ten outputs to direct the light to the sample, homogenize the beam shape, and illuminate the sample uniformly. The outputs of the light guide were arranged in a circular pattern around a 25 MHz, 12.7 mm focused ultrasound transducer (V324-SM, Olympus Panametrics-NDT) such that the center of the illumination spot was aligned with the focus of the transducer. The holder for the transducer and light guide was mounted on a motorized stage for raster scanning and positioning of the transducer. A camera was used

to visualize the samples, verify the alignment of the ultrasound and sample, and detect the *E. coli* colonies on the agar plates.

The acoustic and photoacoustic signals detected by the transducer were amplified by 39 dB using a pulser-receiver unit (5073PR, Olympus Panametric NDT) and recorded with a data acquisition card (CS8229, Gage Applied Technologies). For interlaced photoacoustic and ultrasound imaging, a digital input-output card (NI CB-2162, National Instruments) was used to synchronize the ultrasound and laser systems, similar to previous work [126]. A photodiode signal was recorded and used to normalize the photoacoustic signals.

2.4.5 Construction of tandem Ultramarine 7.2 dimer

To construct a tandem dimer, dimer Ultramarine 7.2 in pBAD/His B was amplified in two separate PCR reactions. In the first reaction, 5' *XhoI* and 3' *PstI* restriction sites were introduced. In the second reaction, 5' *PstI* with a linker and 3' *HindIII* were introducted. Three-way ligation strategy provided a tandem gene of the form A-linker-A in the *XhoI/HindIII* sites of pBAD/His B, where the linker was a 13-residue SCSGTGSTGSGSS including *PstI* restriction site.

2.4.6 Protein purification

E. coli strain JM109(DE3) (Promega) was transformed by electroporation with pQE9N expression vectors containing the Ultramarine gene. A 4 mL culture, inoculated with a single colony, was grown overnight (37 $^{\circ}$ C and 225 rev./min) before being diluted into 250 mL of Terrific broth media containing 0.1 mg/mL ampicillin. This culture was grown in 250 mL baffled shake flasks (37 $^{\circ}$ C and 225 rev./min) to an optical density of 0.6-0.7,

induced with 0.2 mM isopropyl 1-thio-β-D-galactopyranoside (IPTG), and cultured overnight at 30 $^{\circ}$ C before cells were harvested by centrifugation and lysed by cell disruptor (Constant Systems). Proteins were purified by Ni^{2+}-nitrilotriacetate (Ni-NTA) chromatography (Amersham) and then dialyzed into phosphate buffer saline (PBS) (pH 7.4).

E. coli strain JM109(DE3) (Promega) was transformed by electroporation with pRSET B expression vector containing the cjBlue gene. A 4 mL culture, inoculated with a single colony, was grown overnight (37 °C and 225 rev./min) before being diluted into 250 mL of M9 media containing 0.1 mg/mL ampicillin. This culture was grown in a 250 mL baffled shake flasks (37 °C and 225 rev./min) to an optical density of 0.7-0.8, inducted by 0.2 mM IPTG, and cultured for 48 h at 20 °C before cell were harvested by centrifugation and lysed by cell disruptor (Constant Systems). Proteins were purified by Ni-NTA chromatography (Amersham) and then dialyzed into PBS (pH 7.4).

For production of other proteins discussed in this thesis, *E. coli* strain ElectroMAX™ DH10B (Invitrogen) was transformed by electroporation with pBAD/His B expression vectors containing gene encoding the protein of interest. A 4 mL culture, inoculated with a single colony, was grown overnight (37 °C and 225 rev./min) before being diluted into 250 mL of LB medium containing 0.1 mg/mL ampicillin. This culture was grown in 250 mL baffled shake flasks (37 °C and 225 rev./min) to an optical density of 0.6-0.7, inducted by 0.02% L-arabinose, and cultured for overnight at 30 °C before cell were harvested by centrifugation and lysed by cell disruptor (Constant Systems). Proteins were purified by Ni-NTA chromatography (Amersham) and then dialyzed into PBS (pH 7.4).

2.4.7 Spectral feature and photoacoustic imaging signal determination

Absorption spectra exhibited in this chapter were recorded on a DU-800 UV-visible spectrophotometer (Beckman). Absorption measurements were achieved with a 1 cm quartz microcell cuvette.

The molar extinction coefficients (ε) of chromoproteins were determined using the Beer-Lambert Law (ε = A/cl). First, the concentrations of purified proteins were measured with BCA protein assay kit (Thermo Scientific). The known concentration proteins were 5, 10, 15, 20, 25, 30, 40, 50 times diluted into PBS buffer and subjected to absorbance test at given wavelength. Plotting absorbance vs. concentration gave a straight line, which indicated observance of Beer-Lambert law. The slope of the straight line gives the extinction coefficient of the tested chromoprotein.

To determine the quantum yield of chromoproteins, mCherry was chosen as a reference. Briefly, the concentration of a purified protein was adjusted by PBS buffer until absorbance at the excitation wavelength was between 0.2-0.6. A series of dilution of samples and reference with absorbance ranging from 0.01-0.1 were prepared and the fluorescence spectra were recorded on a QuantaMaster spectrofluorometer (Photon Technology International). Integration of the total fluorescence intensity vs. absorbance was plotted for each sample and reference. Quantum yield could be determined from the slopes (S) of each line with the equation: $\Phi_{sample} = \Phi_{reference} \times (S_{sample}/S_{standard})$.

To characterize the photoacoustic characteristics, purified proteins or resuspended *E. coli* cells (1-10×10^9 cells/mL) were diluted in PBS and injected into a 1.57 mm inner diameter tube (PE-205, Intramedic). The tubes were sealed and positioned beneath the transducer for M-mode, B-scan, and C-scan

imaging. To screen the *E. coli* plates, custom software was designed to integrate the data acquisition card, digital input-output card, motion controller, and camera to automatically detect and position the transducer above the *E. coli* colonies.

2.4.8 Determination of oligomerization state

The oligomeric state of all the variants was determined by gel filtration chromatography. Purified proteins were resolved over a HiLoad 16/60 Superdex 75 pg gel filtration column on an AKTA basic liquid chromatography system (GE Healthcare). Gel filtration chromatography buffer (0.05 M Na_3PO_4, 0.15 M NaCl, adjust pH to 7.4) were used as mobile phase with 1 mL/min flow rate. Elution fractions were monitored at 280 nm.

2.4.9 *In vivo* photoacoustic imaging

Animal imaging was performed by injected cells into either ear of rats. All animal experiments were conducted in accordance to the protocols set out by the Animal Care and Use Committee at the University of Alberta.

Chapter 3: Development of new FRET biosensors with a dark tandem dimer acceptor

3.1 Introduction

The FRET phenomenon that occurs between a pair of fluorescent proteins (donor to acceptor) in close proximity generates several design possibilities for fluorescent protein-based live-cell biosensors for a variety of biological processes and physiological functions in live cells. For example, fluorescent protein-based FRET biosensors are used to detect protein-protein interactions, protein conformational changes, [127] and metabolite concentrations in living cells [128]. However, a major limitation to developing these biosensors is spectral contamination. This occurs through undesired direct acceptor excitation and spectral overlap between donor and acceptor emission spectra. These unfavourable features limit experimental design and significantly complicate recording measurements and analyzing data [44]. To overcome this limitation, non-fluorescent chromoproteins have been utilized as 'dark' acceptors (also known as dark quencher) as a partner in FRET pairs. The dark acceptor absorbs energy transferred from donor fluorophore and dissipates it as heat rather than light (**Figure 3.1**).

Sundar et al. first demonstrated the applicability and advantages of dark acceptor based FRET to donor fluorescence lifetime imaging microscopy (FLIM) [25]. Since then, dark acceptor based FRET-FLIM has been widely used as a method for monitoring of caspase-3 activity in live cells [44, 129, 130]. The main advantages of using chromoproteins as dark acceptors arises from the absence of acceptor fluorescence, which not only eliminates the

requirement of narrow spectral filters, but also enables the introduction of other fluorescent indicators for simultaneous multicolor imaging of signaling events [25].

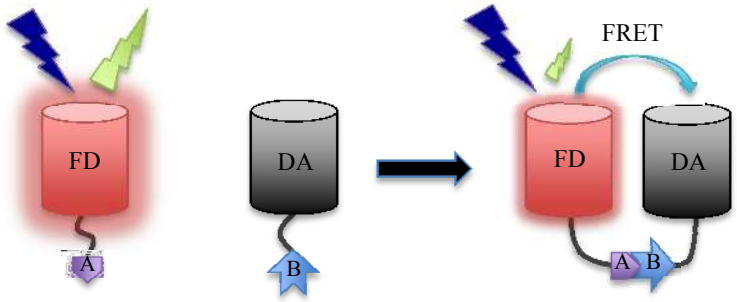

Figure 3.1 Schematic illustration of dark acceptor-based FRET. When fluorescent donor (FD) and Dark acceptor (DA) are brought in close proximity by binding domains (A and B), the fluorescence of donor will be quenched by the dark acceptor.

In Chapter 2, we described the tandem dimer t-Ultramarine 7.2, which exhibits a greater extinction coefficient (ε = 203,400 $M^{-1}cm^{-1}$) and lower quantum yield ($\Phi < 0.0001$) than Ultramarine (ε = 64,000 $M^{-1}cm^{-1}$, $\Phi = 0.001$) [44]. Pettikiriarachchi et al. showed Ultramarine could be used as a dark acceptor for FRET and utilized for live cell apoptosis imaging [44]. Given its spectral properties, we predicted t-Ultramarine 7.2 could serve as a superior dark acceptor for FRET. Therefore, we explored the utility of this dark tandem dimer acceptor to FRET-based biosensors in live cells. To demonstrate the broad application of a dark acceptor, three distinct fluorescent proteins (green EGFP [5], yellow mPapaya1 [131] and red mRuby2 [132]) were chosen as fluorescent donors in caspase-3 FRET-based biosensors. For comparison, caspase-3 biosensors were also constructed using the original Ultramarine as a dark acceptor.

To broaden the potential range of application of dark tandem dimer acceptors, we also developed a cameleon-type Ca^{2+} biosensor [112]. The

donor was also a tandem dimer, red fluorescent protein tdTomato [123]. This double tandem dimer-based cameleon Ca^{2+} biosensor (M13-t-Ultramarine 7.2-tdTomato-CaM) was designated as M2tC and used to monitor the change in Ca^{2+} concentrations in live cells.

3.2 Result and discussion

3.2.1 Verification of dark tandem dimer acceptor for fluorescent proteins *in vitro*

Compared to Ultramarine, the improved tandem dimer chromoprotein t-Ultramarine 7.2 exhibits a greater extinction coefficient (203,400 $M^{-1}cm^{-1}$) and lower quantum yield (< 0.0001). This suggests t-Ultramarine 7.2 would serve as a good dark acceptor for donor fluorescent proteins with a range of emissions in FRET-based biosensors. To verify our hypothesis, GFP, mPapaya1, and mRuby2, were chosen as fluorescent donors due to appropriate spectral overlap (**Figure 3.2**) and promising photophysical properties (**Table 3.1**). Each fluorescent donor was genetically fused to t-Ultramarine 7.2 with a short 10-amino acid peptide linker. The resultant FRET pairs were designated EGFP-t-Ultramarine 7.2, mPapaya1-t-Ultramarine 7.2 and mRuby2-t-Ultamarine 7.2 (**Figure 3.3A**). As a comparison, the FRET pairs EGFP-Ultramarine, mPapaya1-Ultramarine, and mRuby2-Ultramarine were also constructed (**Figure 3.3B**).

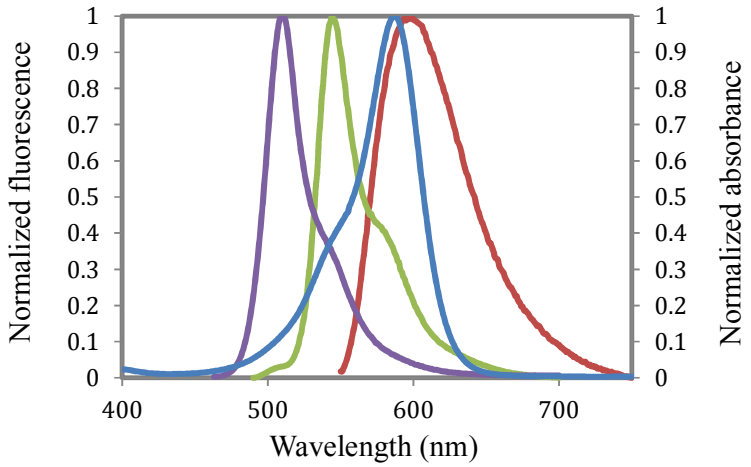

Figure 3.2. Overlap of absorbance of t-Ultramarine 7.2 with fluorescence emission of three fluorescent donors. The absorbance spectrum for t-Ultramarine 7.2 (blue) is shown overlaid with the fluorescence emission spectra of EGFP (purple), mPapaya1 (green) and mRuby2, red).

Table 3.1 Spectral properties of fluorescent donors and dark acceptors

Protein	λ_{ab} (nm)	λ_{em} (nm)	ε (10^3 $M^{-1}cm^{-1}$)	Φ
EGFP	488	507	56	0.60
mPapaya1	530	541	43	0.81
mRuby2	559	600	113	0.38
Ultramarine	586	626	64.6	0.0002
t-Ultramarine 7.2	587	-	203.4	< 0.0001

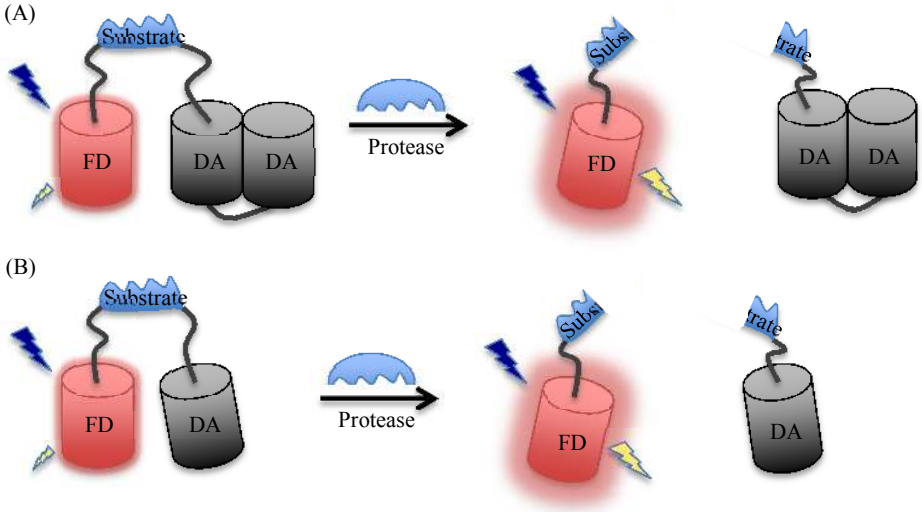

Figure 3.3 Schematic illustration of dark acceptor-based protease biosensor. (A) Schematic illustration of fluorescent protein (FP)-t-Ultramarine 7.2 FRET pairs. (B) Schematic illustration of FP-Ultramarine FRET pairs. Fluorescent donor (FD) and dark acceptor (DA) are depicted by red barrel and black barrel, respectively.

The absorption spectra of donors and acceptors, as well as FRET-biosensors (fusion proteins) were exhibited in **Figure 3.4**. The successful constructions of FRET-biosensors were suggested by the absorption spectra of fusion proteins. The absorption peak ratio of donor and acceptor displayed in each FRET-biosensor absorption spectrum was determined by the overlap of donor and acceptor absorption spectra and their respective extinction coefficient. The less absorption spectra overlap between donor and acceptor, the more dominance of extinction coefficient in the absorption peak ratio of donor and acceptor. **Figure 3.4A-B** exhibited the height of donor EGFP absorption peaks in EGFP-Ultramarine FRET biosensor was twice lower than that of EGFP-t-Ultramarine 7.2 FRET biosensor when the height of acceptors absorption peaks (Ultramarine or t-Ultramarine 7.2) was the same, indicating the extinction coefficient of t-Ultramarine 7.2 was at least twice that of Ultramarine. In addition, the Förster radius (R_o = distance at which 50% of the excitation energy of donor is transferred to the acceptor chromophore) of fluorescent protein-t-Ultramarine 7.2 FRET biosensors are ~1 nm larger than fluorescent protein-Ultramarine FRET pairs (**Table 3.2**). Therefore, we predicted t-Ultramarine 7.2 would be able to be substantially better at quenching the fluorescence of the fluorescent donors compared to Ultramarine.

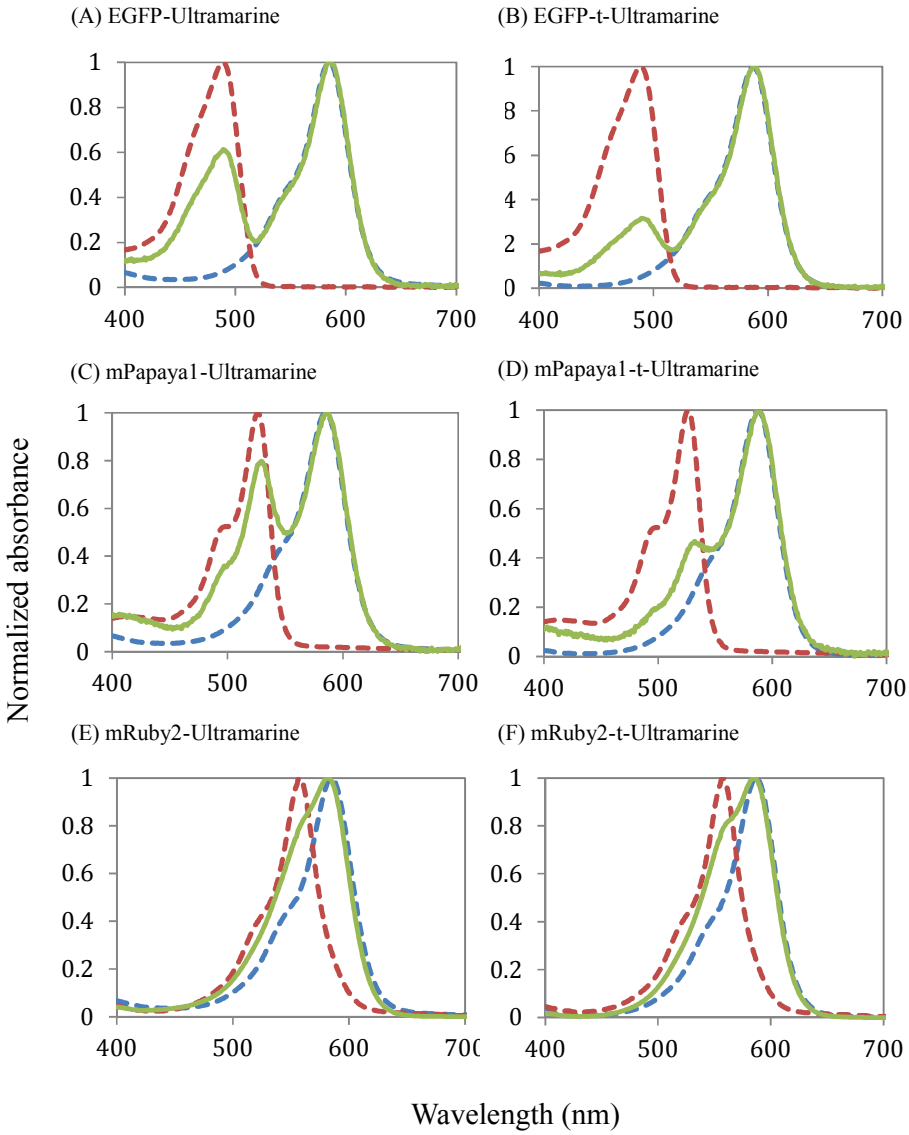

Figure 3.4 Overlap of absorption spectra. Absorption spectrum of FRET biosensors (fusion protein) (green solid) overlaid fluorescent donor absorption spectrum (red dash) and dark acceptor absorption spectrum (blue dash).

To explore the utility of t-Ultramarine 7.2 as a dark acceptor in FRET, all purified FRET fusion proteins were subject to protease cleavage. The fluorescence of the donor was monitored at regular time intervals until protease cleavage reaction completed. The performance of t-Ultramarine 7.2 was compared with Ultramarine (**Figure 3.5**). The fold-increase of donor emission after protease cleavage and p-value are shown in **Table 3.2**. These

results indicate t-Ultramarine 7.2 could be utilized as a dark acceptor in FRET, but surprisingly the performance is not improved relative to Ultramarine.

For the green fluorescent donor EFGP, Ultramarine performs slightly better than t-Ultramarine 7.2. This behaviour may be attributed to Ultramarine's monomeric character and the ability to form a more favourable orientation with EGFP. As we know, many of the mutations that differentiate Ultramarine and Ultramarine 7.2 are on the surface of the protein. The resulting differences in surface charge or hydrophobicity of the donor fluorescent proteins could change the proximity and orientation between the respective donors and acceptors.

For yellow fluorescent donor mPapaya1, t-Ultramarine 7.2 gave a slightly larger intensity change than Ultramarine. However, this improvement is not nearly as substantial as we had predicted. One barrel of the tandem dimer may be too far away from the donor to work optimally as a dark acceptor, resulting in little functionality for the distal barrel.

For the red fluorescent donor mRuby2, Ultramarine is a much better quencher than t-Ultramarine 7.2. The Ultramarine absorption peak of mRuby2-Ultramarine absorption spectrum decreased only slightly after protease cleavage, while mRuby2-t-Ultramarine 7.2 absorption spectrum kept the same (**Figure 3.6**). Since monomer Ultramarine exhibits 65% identity with mRuby2, Ultramarine may form a heterodimer with mRuby2, boosting Ultramarine absorbance in this assay due to higher FRET efficiency. Tandem dimer t-Ultramarine would be unable to make a heterodimer with mRuby2 since its dimer interface is occupied by the fused second copy of the protein.

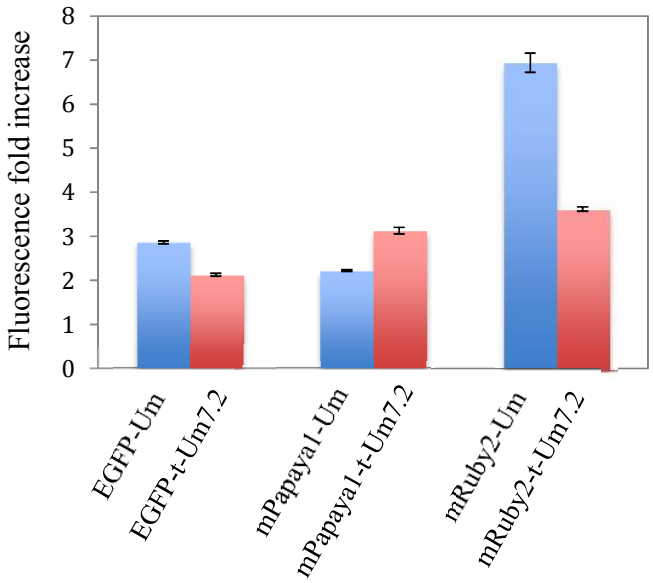

Figure 3.5 Fluorescence intensity increase comparison of FP-t-Ultramarine with FP-Ultramarine after protease cleavage. For the sake of brevity, we use Um instead of Ultramarine. Fluorescence intensity fold increase defined as the fluorescence of donor at the end of protease cleavage/fluorescence of donor without protease cleavage. The end of protease cleavage was identified by SDS-PAGE. Error bars indicate the mean ± s.e.m. All experiments were performed at least three times in triplicate.

Table 3.2 Fluorescence intensity increases of different FRET pairs after protease cleavage

FRET pair	R_0 (nm)*	Fold increase	p-value**
EGFP-Ultramarine	5.05	2.85	< 0.0001
EGFP-t-Ultramarine7.2	6.02	2.13	
mPapaya1-Ultramarine	6.12	2.22	< 0.0001
mPapaya1-t-Ultramarine7.2	7.37	3.13	
mRuby2-Ultramarine	5.38	6.94	< 0.0001
mRuby2-t-Ultramarine7.2	6.54	3.62	

* R_0 values were calculated according to [133]
**Statistical significance was calculated using unpaired Student's test.

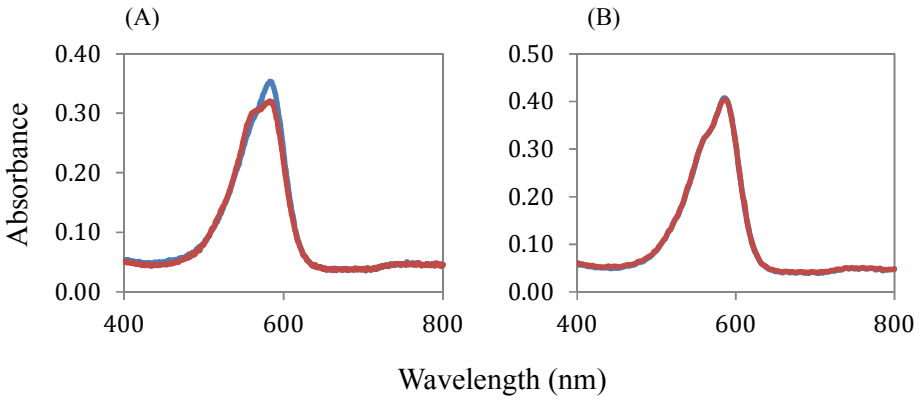

Figure 3.6 Absorption spectra of mRuby2-CP (chromoprotein) before and after protease cleavage. (A) Absorption spectrum of mRuby2-Ultramarine before (blue line) and after (red line) protease cleavage. (B) Absorption spectrum of mRuby2-t-Ultramarine 7.2 before (blue line) and after (red line) protease cleavage.

3.2.2 Live cell imaging with dark tandem dimer acceptor-caspase biosensor

In vitro characterization of fluorescent protein-t-Ultramarine FRET biosensors has demonstrated that chromoproteins are suitable as dark acceptors for a variety of FRET donors. To assess whether our improved dark tandem dimer acceptor could be employed in a caspase-3 biosensor in live cells, six similar FRET constructs were generated as described in Section 3.3.1. The caspase-3 substrate sequence (DEVD) was introduced into the linker joining the fluorescent donor and dark acceptor. These constructs were independently expressed in HeLa cells, followed by treatment with staurosporine to induce caspase-3 activation. As shown in **Figure 3.7**, caspase-3-mediated cleavage of the substrate sequence during apoptosis resulted in an increase in fluorescence. The shrinkage and blebbing of cells indicated the end stages of apoptosis [134]. A comparison of t-Ultramarine 7.2 with Ultramarine as dark acceptor in the caspase-3 biosensors is shown in **Figure 3.8** and **Table 3.3**. The results were consistent with *in vitro*

characterization, with the exception of the mRuby2-Ultramarine FRET pair. We propose that the low expression of protein and complex intracellular environment decreased the extent of heterodimerization between mRuby2 and Ultramarine. Overall, these experiments demonstrate that t-Ultramarine 7.2 is a good quencher for mPapaya1 and mRuby2, but not for EGFP. Disappointingly, t-Ultramarine 7.2 did not provide any substantial improvements relative to the original Ultramarine construct.

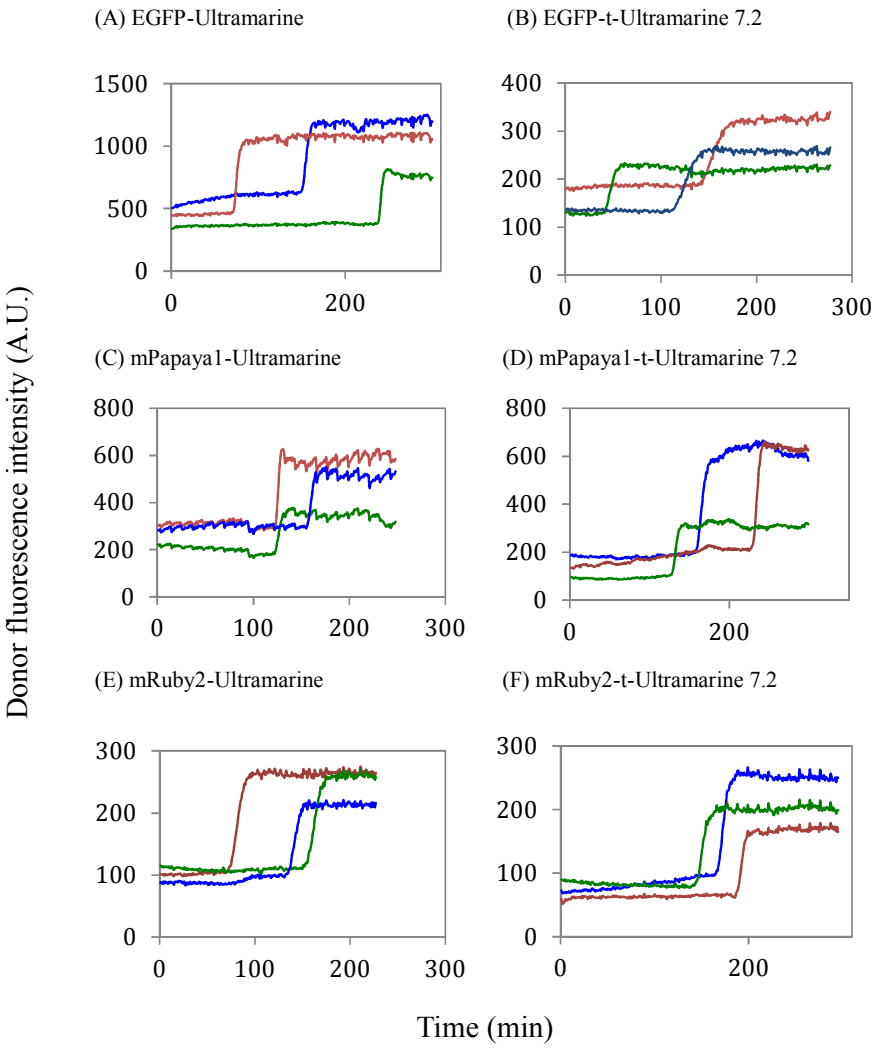

Figure 3.7 Caspase-3 activation assayed by dark acceptor-based FRET described in this work. Transfected HeLa cells were treated with staurosporine (2 μM in HHBSS) and donor fluorescence was monitored over time. Representative traces for individual cells are depicted.

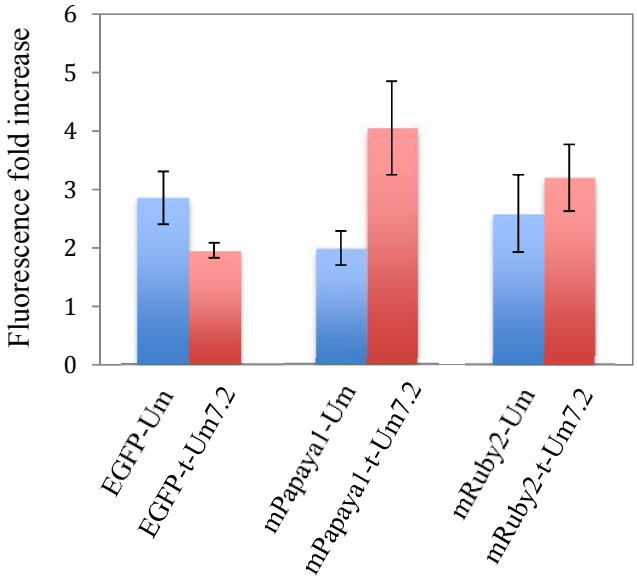

Figure 3.8 Fluorescence intensity increase comparison of FP-t-Ultramarine 7.2 with FP-Ultramarine after caspase-3 activation. For the sake of brevity, we use Um instead of Ultramarine. Error bars indicate the mean ± s.e.m.

Table 3.3 Fluorescence intensity increases of different FRET pairs after caspase-3 activation

FRET pair	Cell number*	Fold increase	p-value**
EGFP-Ultramarine	26	2.86	< 0.0001
EGFP-t-Ultramarine7.2	20	1.96	
mPapaya1-Ultramarine	22	2.00	< 0.0001
mPapaya1-t-Ultramarine7.2	28	4.05	
mRuby2-Ultramarine	13	2.59	< 0.01
mRuby2-t-Ultramarine7.2	18	3.20	

*The number of cells was initiated apoptosis and monitored by microscopy.
**Statistical significance was calculated using unpaired Student's test.

3.2.3 Construction and characterization of a tandem dimer-based calcium ion (Ca^{2+}) biosensor

To determine if the t-Ultramarine acceptor-based FRET could be employed to visualize an intracellular signalling activity, we designed a double tandem dimer-based Ca^{2+} biosensor. In this design, tdTomato was chosen as the fluorescent donor (**Figure 3.9** and **Table 3.4**) with t-Ultramarine

7.2 serving as the dark acceptor due to the large spectra overlap and promising extinction coefficient, quantum yield and the Förster radius.

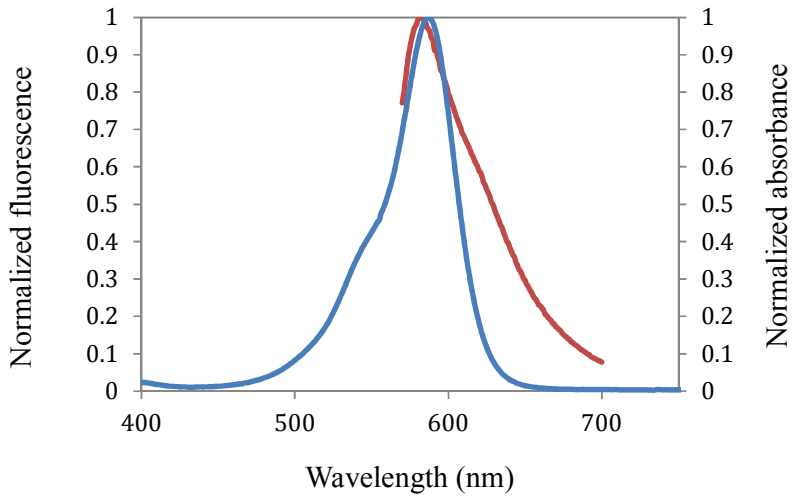

Figure 3.9 Overlap of t-Ultramarine 7.2 absorbance (blue line) and tdTomato fluorescence (red line).

Table 3.4 Spectral properties of fluorescent donors and dark acceptors

Protein	λ_{ab} (nm)	λ_{em} (nm)	ε ($10^3 M^{-1}cm^{-1}$)	Φ	R_0 (nm)
tdTomato	554	581	138	0.6	7.21
t-Ultramarine 7.2	587	-	203.4	< 0.0001	

The Ca^{2+}-binding protein calmodulin (CaM) and its binding peptide M13 (from skeletal muscle myosin light-chain kinase) were genetically fused to the N-terminus of t-Ultramarine 7.2 and C-terminus of tdTomato, respectively. This rendered the following fusion: CaM-t-Ultramarine 7.2-tdTomato-M13 (designated as M2tC) (**Figure 3.10**). Ca^{2+} binding to CaM induces the interaction of CaM and M13, which brings the donor and acceptor fluorescent proteins into close proximity and leads to a decrease in fluorescence.

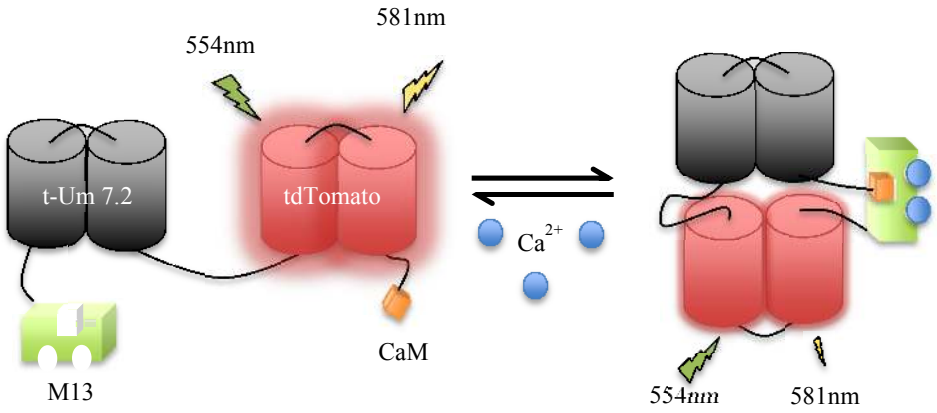

Figure 3.10 Schematic illustration of dark-acceptor-based Ca^{2+} sensor. Donor is tdTomato (red barrels) and dark acceptor is t-Ultramarine 7.2 (black barrels). For the sake of brevity, we use Um instead of Ultramarine.

In vitro characterization of the purified FRET construct showed M2tC exhibited a spectral response to Ca^{2+}. As shown in **Figure 3.11A**, addition of Ca^{2+} resulted in a donor fluorescence decreasing approximately 1.9-fold, which is very good relative to some other cameleon-type Ca^{2+} biosensors. For example, the fold changes in donor fluorescence of YC3.3 [135], YC6.1 [136], D3cpv [112] and CaYin1 [137] were approximately 1.2- and 1.6-, 1.7- and 1.5-fold respectively. However, YC3.3, YC6.1, D3cpv and CaYin1 are ratiometric cameleon-type Ca^{2+} biosensors, which helps to increase their dynamic range beyond that achievable from only the change in donor intensity. Specifically, the cameleon-type sensors mentioned here have ratiometric dynamic ranges of approximately 2.0-, 2.0-, 6.1- and 2.1-fold, respectively.

The M2tC Ca^{2+} biosensor has a K_d value of 419 ± 37 nM and a Hill coefficient (n) value of 2.6 (**Figure 3.11B**). Since the concentration of free calcium (Ca^{2+}) ions in cytoplasm of a eukarytic cell before stimulation is approximately 100 nM and increases to 1000 nM after stimulation [138], therefore, M2tC can be used to monitor the concentration change of Ca^{2+} cytoplasm.

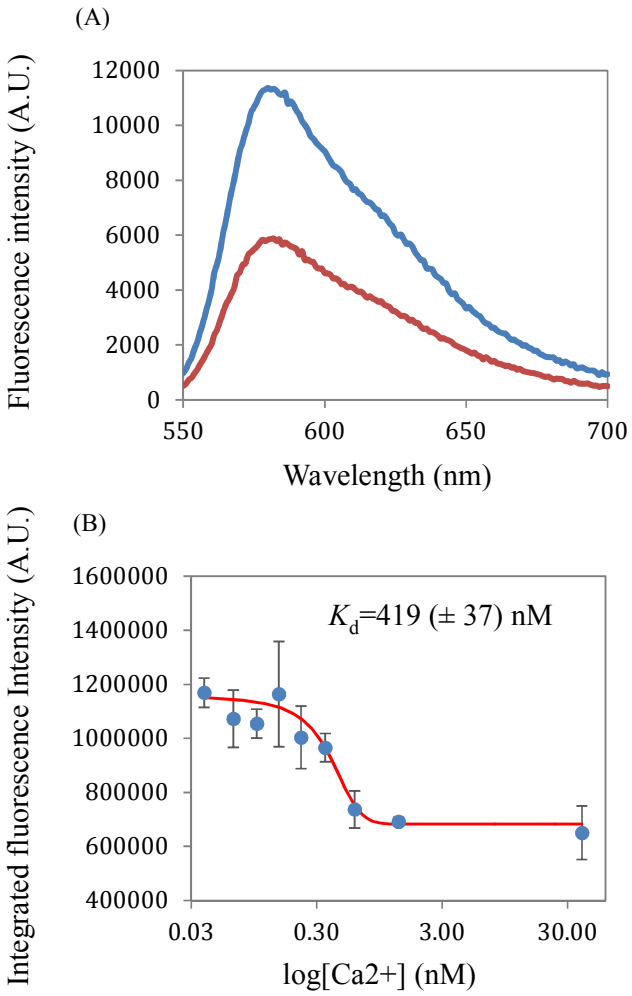

Figure 3.11 *In vitro* characterization of Ca^{2+} biosensor. (A) The Ca^{2+} dependent donor emission change of M2tC. Fluorescence of donor at Ca^{2+} free and saturation are exhibited by blue and red line respectively. (B) Determination of the K_d of Ca^{2+} binding to M2tC.

We next investigated the utility of M2tC for monitoring changes in Ca^{2+} by live cell imaging. HeLa cells were transfected with a M2tC-encoding plasmid and imaged 24 h post transfection. Upon histamine stimulation, oscillations in donor red fluorescence intensity were observed due to Ca^{2+} release (**Figure 3.12**), which was consistent with the results obtained for previously reported Ca^{2+} indicators [23]. Unlike conventional Ca^{2+} sensors, fluorescence decreases with Ca^{2+} binding. To determine the *in situ* dynamic range, cells were treated with ionomycin/EGTA to deplete Ca^{2+} after

approximately 10 min of fluorescence oscillations, and then treated with a high concentration of ionomycin/Ca^{2+} to saturate CaM [139]. It demonstrated that M2tC exhibited comparable dynamic range (~1.3-fold) with other ratiometric cameleon-type Ca^{2+} biosensors in live cells, such as YC2.1 (~1.4-fold) [113], YC3.3 (~1.7-fold) [135], YC6.1 (~2.1-fold) [136] and D3cpv (~1.9-fold) [112], or single fluorescent protein-based Ca^{2+} biosensors, like CH-GECO1.0 (~1.7-fold) [140]. However, the dynamic range of M2tC *in situ* was less than that observed *in vitro*, possibly indicating the partners were partially associated at the levels of intracellular protein production.

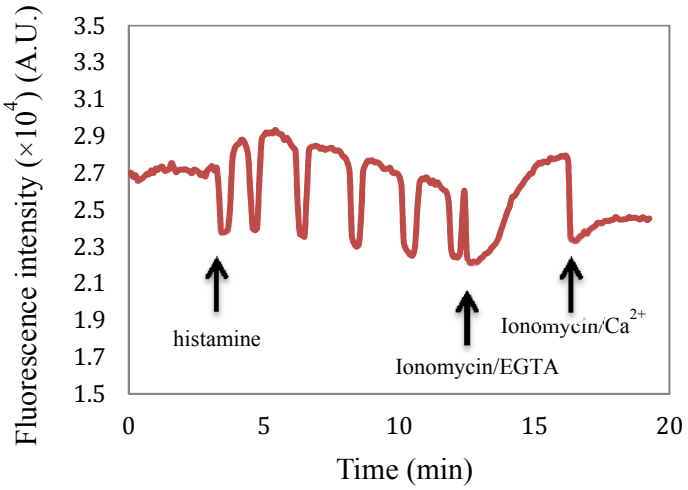

Figure 3.12 Imaging of Ca^{2+} dynamics in live cells using biosensor M2tC. Representative live cell trace of a transfected HeLa cell treated with histamine, followed by EGTA/ionomycin and Ca^{2+}/ionomycin. Donor red fluorescence was imaged as a function of time.

3.3 Conclusion

In this chapter, we utilized the improved chromoprotein t-Ultramarine 7.2 to develop FRET-based biosensors. We demonstrated dark tandem dimer acceptor based protease biosensors could be used to monitor protease activity and successfully monitored caspase-3 activity in live cells. Furthermore, the

newly developed two tandem dimer-based Ca^{2+} biosensor **M2tC** enables monitoring Ca^{2+} concentration of single live cell. Therefore, the tandem dimer could be used in FRET-based biosensors with satisfactory performance, which alleviates the requirement of engineering monomer versions.

3.4 Materials and methods

3.4.1 General method

All synthetic DNA oligonucleotides used for cloning and library were purchased from Integrated DNA Technologies (Coralville, IA). Miniprep plasmid DNA, polymerase chain reactions (PCR), restriction enzyme digestion, ligation and agarose gel electrophoresis were performed according to Sambrook et al [125]. *Pfu* DNA polymerase was obtained from Fermentas used for regular PCR and the QuikChange Multi kit was purchased from Agilent Technologies used for Site-Directed Mutagenesis. All restriction enzymes were obtained from Fermentas or New England Biolabs. T4 DNA ligase was obtained from Invitrogen or Life Technologies. PCR and digestion products were purified with the QIA quick gel extraction kit (QIAGEN, Valencia, CA) or GeneJET gel extraction kit (Fermentas) according to the manufacturer's instructions. All sequencing was performed at the MBSU at the University of Alberta or University Core DNA Services at University of Calgary. All filters for fluorescence imaging were purchased from Chroma Technology (Rockingham, VT), Omega Filters (Brattleboro, VT), or Semrock (Rochester, NY).

3.4.2 Construction of protease biosensor for in vitro test

To construct t-Ultramarine 7.2 fusions to EGFP, mPapaya1 and mRuby2 for testing protease activity, the fluorescent donor genes (EGFP, mPapaya1

and mRuby2) were amplified with a 5' *XhoI* forward primer and a 3' *KpnI* containing a linker 1 reverse primer in three separate PCR reactions. This linker 1 was a 10-residue GSGDEVDGGT including *KpnI* restriction site. Meanwhile, Ultramarine 7.2 in pBAD/His B was amplified in two separate PCR reactions. In the first reaction, 5' *KpnI* and 3' *PstI* restriction sites were introduced. In the second reaction, 5' *PstI* with a linker 2 and 3' *HindIII* were introduced, where the linker 2 was a 13-residue SCSGTGSTGSGSS including *PstI* restriction site, see 2.4.5 (construction of t-Ultramarine 7.2). A four-way ligation strategy provided a form A-linker 1-B-linker 2-B in *XhoI/HindIII* sites of spBAD/His B (**Figure 3.13**). [Note: spBAD/His B was an unexpected gift from research progress. I discovered a pBAD/His B plasmid with mutation 2056 A-C in pBR322 origin, which boosted the plasmid replication at least two times. The s stands for strong, namely spBAD/His B].

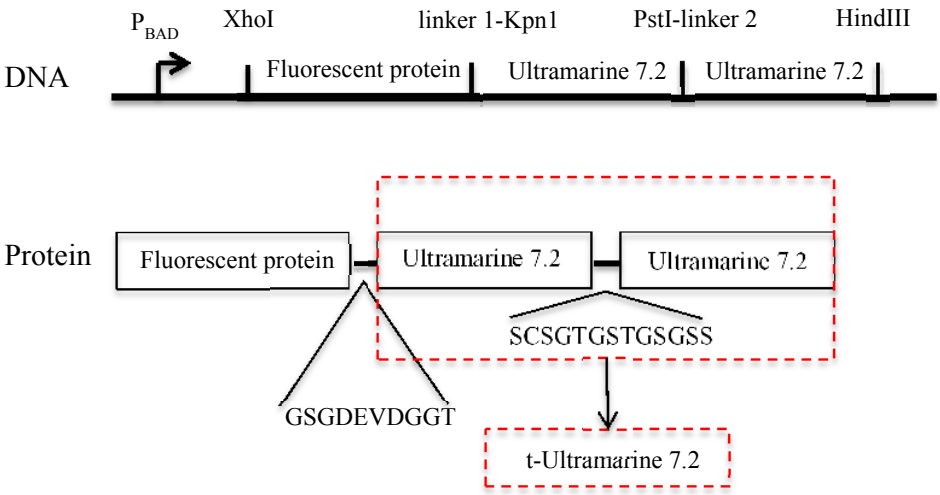

Figure 3.13 Expression cassette design for protease biosensor. Fluorescent protein refers to EGFP, mPapaya1 or mRuby2.

To construct fluorescent protein (i.e., EGFP, mPapaya1 and mRuby2) plus Ultramarine FRET constructs, the gene encoding Ultramarine was

amplified with a 5' *KpnI* forward primer and 3' *HindIII* reverse primer. Three-ligation (A-linker 1-B) was performed in *XhoI/HindIII* sites of spBAD/His B.

To achieve complete cleavage by trypsin for FRET (mPapaya 1-chromoprotein and EGFP-chromoprotein), we increased the efficiency of trypsin cleavage by substituting the DE amino acids in linker 1 with KK.

3.4.3 Construction of caspase-3 biosensor for live cell imaging

For mammalian cell expression of FRET construct, a modified pcDNA3.1(+) vector developed by Dr. Yidan Ding [137] was utilized. After modification, the vector has *XhoI* and *HindIII* restriction sites in the same reading frame as the same site in pBAD/His B vector. All the FRET constructs containing caspase-3 cleavage substrate DEVD were treated with XhoI and HindIII, and ligated with similarly treated modified pcDNA3.1(+) vector.

3.4.4 Construction of a tandem dimer-based Ca^{2+} biosensor

To assemble **M2tC**, a modified pBAD/His B containing N-M13-*XhoI* and C-*MluI*-CaM-*HindIII* were utilized. This modified vector is credited to PhD candidate Jiahui Wu. Ultramarine 7.2 in pBAD/His B was amplified in two separate PCR reactions. In the first reaction, 5' *XhoI* and 3' *PstI* restriction sites were introduced. In the second reaction, 5' *PstI* with a linker 1 (13-residue SCSGTGSTGSGSS including *PstI* restriction site) and 3' *XbaI* with a linker 2 (6-residue GGGSSR including *XbaI* restriction site) were introduced. Meanwhile, tdTomato was amplified with a 5' *XbaI* forward primer and 3' *MluI* reverse primer. Four-way ligation was performed to construct plasmid M13-t-Ultramarine 7.2-tdTomato-CaM (M2tC) in pBAD/His B (**Figure 3.14**).

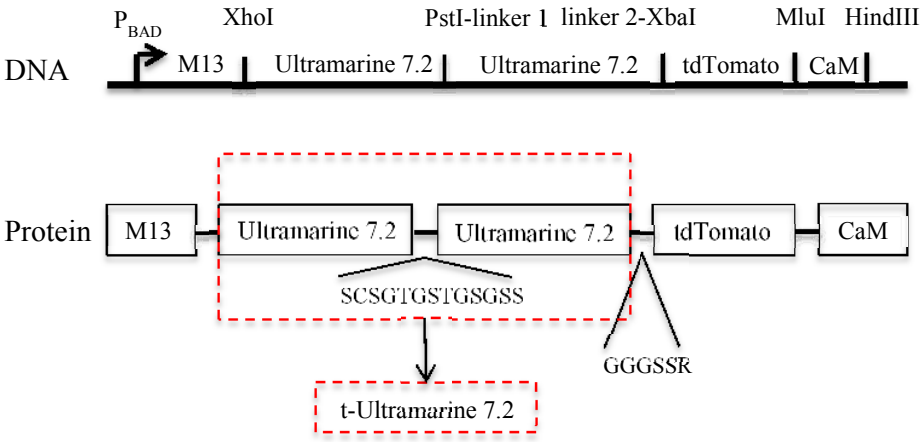

Figure 3.14 Expression cassette design for M2tC Ca^{2+} biosensor.

To construct a mammalian expression plasmid, the *XhoI* restriction site in modified pcDNA3.1(+) described in Section 3.4.3 was mutated to create an *EagI* site, while concurrently, the *EagI* restriction site in the ampicillin-resistance gene was eliminated. CaM was amplified with 5' *EagI* forward primer and 3' *XhoI* reverse primer. Plasmid **M2tC** in pBAD/His B was treated with XhoI and HindIII to obtain genes t-Ultramarine 7.2-tdTomato-M13. Finally, three-way ligation was performed to construct M2tC mammalian expression plasmid.

3.4.5 Protein purification and characterization

For production of protein, *E. coli* strain ElectroMAX™ DH10B (Invitrogen) was transformed by electroporation with spBAD/His B expression vectors containing gene encoding the protein of interest. A 4 mL culture, inoculated with a single colony, was grown overnight (37 °C and 225 rev./min) before being diluted into 250 mL of LB medium containing 0.1 mg/mL ampicillin. This culture was grown in 250 mL baffled shake flasks (37 °C and 225 rev./min) to an optical density of 0.6-0.7, inducted by 0.02% L-arabinose, and cultured for overnight at 28 °C and then low temperature to

20 °C for another 24-48 h culture before cell were harvested by centrifugation and lysed using a cell disruptor (Constant Systems). Proteins were purified by Ni-NTA chromatography (Amersham) and then buffer changed into PBS (pH 7.4). FRET constructs for protease cleavage were further purified by size exclusion column chromatography (Amersham Superdex 75 prep) in gel filtration chromatography buffer (GFC) (0.05 M Na_3PO_4, 0.15 M NaCl, pH 7.4). The Ca^{2+} biosensor **M2tC** was dialyzed into KCl-MOPS buffer (30 mM MOPS, 100 mM KCl, pH 7.2).

Absorption spectra were recorded on a DU-800 UV-visible spectrophotometer (Beckman). Absorption measurements were acquired with a 1 cm quartz microcell cuvette. Fluorescence measurements were recorded on a Safire2 plate reader (Tecan).

Protease cleavage of FRET *in vitro* was tested by monitoring the donor fluorescence change. 100 μL purified each FRET fusion proteins (absorption < 0.1 at wavelength 280 nm) with and without 1 μL trypsin (5mg/mL) were incubated at 37 °C for 30 min. The donor fluorescence was monitored at regular time intervals on a Safire2 plate reader (Tecan) until cleavage endpoint was achieved. To confirm the trypsin cleavage efficiency, the samples were further analysed by SDS-PAGE. Fluorescence intensity fold increase defined as the fluorescence of donor at the end of protease cleavage/fluorescence of donor without protease cleavage. All experiments were performed at least three times in triplicate.

The Ca^{2+} dependent spectra measurement of M2tC were performed in solution containing 1 μL purified protein and 10 mM EGTA or 10 mM EGTA-Ca^{2+} 30 mM MOPS, 100 mM KCl, pH 7.2. To determine the K_d of

M2tC for binding to Ca^{2+}, a series of KCl-MOPS buffers containing a range of Ca^{2+} concentration were prepared according to the protocol provided by 'Molecular probes' Ca^{2+} calibration buffer kits. Purified M2tC was then diluted 1:50 into the Ca^{2+} buffer and their fluorescence were recorded on a Safire2 plate reader (Tecan). Data was fit with a Hill equation: $F_i = F_0 + (F_{max} - F_0) \times \frac{[Ca^{2+}]^n}{(K_d{}^n + [Ca^{2+}]^n)}$, where F_0 and F_{max} are fluorescence without Ca^{2+} and with saturated Ca^{2+}, respectively, and n is Hill coefficient. The calculated K_d represents the concentration of Ca^{2+} that gives half of the maximum fluorescence change.

3.4.6 General methods for the live cell imaging

All the mammalian cells expression plasmids were purified using a Plasmid Miniprep kit (Qiagen). Hela cells (CCL2 line; ATCC) were maintained in Dulbecco's Modified Eagle Medium (DMEM) (Invitrogen) supplemented with 10% fetal bovine serum (FBS) (Sigma), 2 mM GlutaMax (Invitrogen) and penicillin-streptomycin at 37 °C and 5% CO_2 according to standard procedures. Transient transfection was carried out using Turbofect™ (Fermentas) according to manufacturer's instructions. Generally, cells in 35 mm imaging dishes were transfected with 1 μg plasmid DNA mixed with 2 μL of transfection reagent. Imaging was performed after 24-48h post-transfection at room temperature in HEPES-buffered Hank's Balance Salt Solution (HHBSS).

3.4.7 Imaging of staurospaurine-induced apoptosis

To initiate apoptosis, cells were treated with 2 μM staurosporine and incubated another 60-90 min before imaging. Imaging was conducted on an

Axiovert 200M microscopy (Zeiss) equipped with a 75W xenon-arc lamp and 20× objective lens (NA=0.75, air) and a 14-bit CoolSnap HQ2 cooled CCD camera (Photometrics), driven by open source Micro-Manager software. For a typical experiment, images were recorded at 1 minute intervals.

3.4.8 Ca^{2+} imaging in live cells

Cells were maintained in 1-1.5 mL HHBSS and imaged on an inverted Nikon Eclipse Ti microscope equipped with a 150W Lumen 200 metal halide lamp (Prior Scientific) with a 25% neutral density filter, a 40× objective (NA=0.95, air) and a 16-bit 512SC QuantEM CCD (Photometrics) for approximate 200 s prior to addition of 5 mM histamine. Recorded histamine-induced oscillations images for 10 min before adding 5 mM EGTA and 5 μM ionomycin. After approximately 2 min imaging, 10 mM Ca^{2+} and 5 μM ionomycin was added and continued imaging another 2 min before the end the experiment. Images were recorded at a frequency of 5 s. The NIS-Elements AR 3.0 software package (Nikon) was used for automated computer control and for quantitative image analysis.

Chapter 4: Conclusion and future directions

4.1 Summary of thesis

The discovery of non-fluorescent chromoproteins in coral polyps and hydroid jellyfish broadened the scope of our knowledge about GFP-like proteins. They are a valuable source of fluorescent proteins with unique characteristics, such as far-red fluorescence, photoswitching properties, and enhanced phototoxicity. However, chromoproteins have been thus far under-utilized as probes for live cell imaging due to their lack of fluorescence. Fortunately, the energy absorbed by chromoproteins leads to the generation of acoustic waves, which can be detected by an ultrasound transducer. Therefore, there is great potential to use chromoproteins as genetically encoded labels for photoacoustic imaging, giving impetus to evolve chromoproteins for enhanced photoacoustic properties.

With this purpose, and in collaboration with Dr. Roger J. Zemp, we developed a novel colony-based chromoproteins screening method. Using this method in addition with absorption-based screening, we were able to image libraries of chromoproteins mutants and picked the best variants. To provide motivation for evolving chromoproteins rather than fluorescent proteins, we initially demonstrated chromoproteins exhibited more red-shift absorption and higher photoacoustic signal as well as enhanced photostability. Ultramarine and cjBlue were chosen as chromoprotein gene templates and subjected to iterative directed evolution and subsequent absorption screening with photoacoustic screening. The variants t-Ultramarine 7.2 and cjBlue 7.1 exhibited much stronger photoacoustic signals relative to the starting

templates and were proven suitable for *in vivo* imaging.

In vitro characterization showed t-Ultramarine 7.2 is a tandem dimer and has greater quantum yield and lower extinction coefficient relative to monomer Ultramarine. To verify t-Ultramarine 7.2 could serve as a superior dark acceptor for FRET than Ultramarine, we constructed biosensors using six different FRET pairs that utilized three distinct fluorescent proteins (green EGFP, yellow mPapaya1 and red mRuby2) as fluorescent donors and explored their application in live cell imaging. We showed the tandem dimer was suitable for FRET applications with two acceptors and served as useful caspase-3 biosensors. Furthermore, to expand the application of t-Ultramarine 7.2, we successfully developed a 'cameleon'-style Ca^{2+} biosensor M2tC with fluorescent donor (tdTomato) and dark acceptor (t-Ultramarine 7.2) and applied it to monitor the changes in Ca^{2+} concentration in the cytoplasm of a single live cell. In contrast to traditional FRET-based biosensors (both donor and acceptor are fluorescent proteins), dark acceptor based FRET biosensors only need one emission channel and thus allow additional emission channel to be assigned to detect other parameters concurrently.

4.2 Future directions

4.2.1 Photoacoustic imaging-based screening method for the evolution of chromoproteins

Non-invasive imaging of deep tissues in live organisms requires both advanced imaging techniques and probes. Photoacoustic imaging enables imaging deeper optically-absorbing molecules in tissue with higher resolution compared with traditional optical imaging techniques. Genetically-encoded probes are useful in biomedical imaging and academic research to non-

invasively understand various biological interactions and activity. An optimal genetically-encoded probe for *in vivo* photoacoustic imaging should exhibit an absorption maxima within the near-infrared window (650-900nm), for which tissue has lowest absorption [141]. However, heretofore the absorption spectra of even the most far-red shifted GFP-like proteins still are outside of the near-infrared window. Filonov et al. has engineered a phytochrome-based near-infrared protein (iRFP) with an absorption maximum at 692nm and also demonstrated its application to photoacoustic imaging [107, 142]. Compared with t-Ultramarine 7.2 (ε = 203,400 $M^{-1}cm^{-1}$, Φ < 0.0001), iRFP is also a dimer but has lower extinction coefficient (ε = 105,400 $M^{-1}cm^{-1}$) and higher quantum yield (Φ = 0.057), which means iRFP has a great potential for improvement. In chapter 2, we proved the utility of a photoacoustic imaging based screening method for the directed evolution of chromoproteins. Therefore, we can utilize this new method to develop iRFP to be a good genetically-encoded photoacoustic probe. Another near-infrared protein DsmURFP (not published) developed from the allophycocyanin alpha subunit of phycobilisome of cyanobacteria by Erik Rodriguez (post-doc. in Roger Tsien group) is also a good candidate for photoacoustic imaging attributing to its promising spectral properties (absorbance maximum = 666nm, ε = 160,000 $M^{-1}cm^{-1}$, Φ = 0.18).

After characterization of the improved variants obtained from directed evolution, we observed that improved photoacoustic signal might due to increase of extinction coefficient and decrease of quantum yield. This leads us to speculate the photoacoustic signal intensity can be used to make quantitative measurements of chromoprotein spectral properties. Thereby, we

can take advantage of this photoacoustic imaging-based screening technique to evolve a range of chromoproteins to be used as dark acceptors in FRET.

We applied t-Ultramarine 7.2 to *in vivo* imaging in rodents, but we have thus far only investigated the implants of *E. coli* pellets in ear of a rat due to time limitations. In future *in vivo* imaging studies, stable mammalian cell lines expressing t-Ultramarine 7.2 will be required. Cell implants with these cells will permit more physiologically relevant t-Ultramarine 7.2 imaging in live animals.

4.2.2 'Dark' acceptor-based FRET biosensors

A well documented limitation to using fluorescent protein-based FRET biosensors is broad excitation and emission profiles, which limit the number of FRET pairs that can be applied in single cells. The use of a dark acceptor fluorescent protein as one FRET partner addresses this limitation since only the donor emission is monitored. Monomeric fluorescent proteins are generally preferred as acceptors in FRET biosensors because of their small size and reduced propensity to oligomerize. However, as we described in Chapter 3, we successfully demonstrated tandem dimer t-Ultramarine 7.2 can be used as a dark acceptor in FRET-based biosensors, including biosensors for caspase-3 activity and Ca^{2+} dynamics. The tandem dimer also behaved similarly to its corresponding monomeric dark acceptor. This represents an important development for protein engineering, especially for chromoproteins, since most naturally occurring chromoproteins are tetrameric, or even oligomeric. Importantly, development of a dimer is less laborious than engineering a monomeric protein, thus saving significant time and expense. To illustrate, the dimeric red fluorescent protein called dimer2 was engineered

from DsRed by introducing 17 mutations, but the monomeric red fluorescent protein mRFP1 required 33 mutations relative to DsRed. Since monomeric character is not a necessity, protein engineers are now poised to evolve a variety of chromoproteins for use as dark acceptors in FRET-based biosensors.

One interesting exception of a chromoprotein that lacks oligomeric character is anm2CP, which is naturally a monomer [61]. Its promising spectral characters (absorbance maximum = 572nm, ε = 120,000 $M^{-1}cm^{-1}$, Φ < 0.001) of anm2CP will enable its use in FRET-based biosensors, serving as dark acceptor.

In addition to monitoring single cell caspase-3 activity or Ca^{2+} concentration in the cytoplasm, future applications could extend to dark acceptor-based dual biosensors (such as EGFP-Ultramarine and mRuby2-Ultramarine). Other applications include: (1) imaging the Ca^{2+} concentration in two compartments of a single cell [137]; (2) measuring the delay between the onset of caspase-3 activity in the nucleus and cytoplasm during apoptosis of a single cell [24]; (3) monitoring both Ca^{2+} concentration and caspase-3 activity in the same compartment of a single cell [137]; (4) Concurrent monitoring of two caspase activities [143].

What's more interesting and promising, the photoacoustic imaging method may to be utilized to test or monitor photoacoustic signal intensity change of dark acceptor-based FRET, instead of donor fluorescence change monitored by microscopy.

4.3 Concluding remarks

In summary, the research presented in this thesis described our efforts to engineer and optimize chromoproteins and utilize improved variants in

photoacoustic imaging and FRET-based biosensor applications. With this purpose in mind, we developed a novel photoacoustic imaging based screening method used to screen for photoacoustic signals in *E.coli* colonies. The method proved useful for the identification of improved variants with higher photoacoutic signal as well as desirable spectral characteristics. Using an improved variant, t-Ultramarine 7.2, we successfully demonstrated the utility of a tandem dimer acceptor in FRET-based caspase-3 biosensors and Ca^{2+} biosensors. We believe photoacoustic screening method will be useful in the photoacoustic molecules evolution and help in deep-tissue, non-invasive, *in vivo* studies while improved chromoproteins mark a significant addition to the GFP-like protein toolkit and will facilitate the design of useful biosensors.

Bibliography

1. Fox, D.L. Animal Biochromes and Structural Colours: Physical, Chemical, Distributional & Physiological Features of Coloured Bodies in the Animal World (2th ed.). *University of California Press*, Berkeley, **1976.**

2. Cheesman, D.F., Lee, W.L., and Zagalsky, P.F. Carotenoproteins in Invertebrates. *Biol Rev Camb Philos Soc* **1967**, 42(1), 131.

3. Herring, P.J. Blue Pigment of a Surface-Living Oceanic Copepod. *Nature* **1965**, 205(4966), 103.

4. Fox, D.L. and Pantin, C.F.A. Pigments in the Coelenterata. *Biol Rev Camb Philos Soc* **1944**, 19(4), 121.

5. Tsien, R.Y. The Green Fluorescent Protein. *Annu. Rev. Biochem.* **1998**, 67, 509-544.

6. Labas, Y.A., Gurskaya, N.G., Yanushevich, Y.G., Fradkov, A.F., Lukyanov, K.A., Lukyanov, S.A., and Matz, M.V. Diversity and Evolution of the Green Fluorescent Protein Family. *Proc. Natl. Acad. Sci. U. S. A.* **2002**(7), 4256.

7. Craggs, T.D. Green Fluorescent Protein: Structure, Folding and Chromophore Maturation. *Chem. Soc. Rev.* **2009**, 38(10), 2865-2875.

8. Matz, M.V., Lukyanov, K.A., and Lukyanov, S.A. Family of the Green Fluorescent Protein: Journey to the End of the Rainbow. *Bioessays* **2002**, 24(10), 953-959.

9. Campbell, R.E. and Davidson, M.W. "Fluorescent Reporter Proteins", Molecular Imaging with Reporter Genes. Eds. Gambhir, S.S., Yaghoubi, S.S. *Cambridge University Press*, New York, **2010**, 3-40.

10. Davidson, M.W. and Campbell, R.E. Engineered Fluorescent Proteins: Innovations and Applications. *Nat. Methods* **2009,** 6(10), 713-717.

11. Chudakov, D.M., Matz, M.V., Lukyanov, S., and Lukyanov, K.A. Fluorescent Proteins and Their Applications in Imaging Living Cells and Tissues. *Physiol. Rev.* **2010**, 90(3), 1103-1163.

12. Wu, B., Piatkevich, K.D., Lionnet, T., Singer, R.H., and Verkhusha, V.V. Modern Fluorescent Proteins and Imaging Technologies to Study Gene Expression, Nuclear Localization, and Dynamics. *Curr. Opin. Cell Biol.* **2011**, 23(3), 310-317.

13. Zhang, H.F., Maslov, K., Stoica, G., and Wang, L.V. Functional Photoacoustic Microscopy for High-Resolution and Noninvasive in Vivo Imaging. *Nat. Biotechnol.* **2006**, 24(7), 848-851.

14. Wang, L.V. and Hu, S. Photoacoustic Tomography: In Vivo Imaging from Organelles to Organs. *Science* **2012**, 335(6075), 1458-1462.

15. Wang, L.V. Prospects of Photoacoustic Tomography. *Med. Phys.* **2008**, 35(12), 5758-5767.

16. Wang, L.V. Multiscale Photoacoustic Microscopy and Computed Tomography. *Nat. Photonics* **2009**, 3(9), 503-509.

17. Razansky, D., Distel, M., Vinegoni, C., Ma, R., Perrimon, N., Köster, R.W., and Ntziachristos, V. Multispectral Opto-Acoustic Tomography of Deep-Seated Fluorescent Proteins in Vivo. *Nat. Photonics* **2009**, 3(7), 412-417.

18. Laufer, J., Jathoul, A., Pule, M., and Beard, P. Evaluation of Genetically Expressed Absorbing Proteins Using Photoacoustic Spectroscopy. *Proc. of SPIE*. Eds. Oraevsky, A.A. and Wang, L.V. Bellingham, **2013**, 8581, 8581X-1-5.

19. Zhang, J., Campbell, R.E., Ting, A.Y., and Tsien, R.Y. Creating New Fluorescent Probes for Cell Biology. *Nat. Rev. Mol. Cell Biol.* **2002**, 3(12), 906-918.

20. Griesbeck, O. Fluorescent Proteins as Sensors for Cellular Functions. *Curr. Opin. Neurobiol.* **2004**, 14(5), 636-641.

21. Ibraheem, A. and Campbell, R.E. Designs and Applications of Fluorescent Protein-Based Biosensors. *Curr. Opin. Chem. Biol.* **2010**, 14(1), 30-36.

22. Ding, Y.D., Ai, H.W., Hoi, H., and Campbell, R.E. Forster Resonance Energy Transfer-Based Biosensors for Multiparameter Ratiometric Imaging of Ca^{2+} Dynamics and Caspase-3 Activity in Single Cells. *Anal. Chem.* **2011**, 83(24), 9687-9693.

23. Zhao, Y.X., Araki, S., Wu, J.H., Teramoto, T., Chang, Y.F., Nakano, M., Abdelfattah, A.S., Fujiwara, M., Ishihara, T., Nagai, T., and Campbell, R.E. An Expanded Palette of Genetically Encoded Ca2+ Indicators. *Science* **2011**, 333(6051), 1888-1891.

24. Ai, H.W., Hazelwood, K.L., Davidson, M.W., and Campbell, R.E. Fluorescent Protein Fret Pairs for Ratiometric Imaging of Dual Biosensors. *Nat. Methods* **2008**, 5(5), 401-403.

25. Ganesan, S., Ameer-Beg, S.M., Ng, T.T.C., Vojnovic, B., and Wouters, F.S. A Dark Yellow Fluorescent Protein (YFP)-Based Resonance Energy-Accepting Chromoprotein (REACh) for Förster Resonance Energy Transfer with GFP. *Proc. Natl. Acad. Sci. U. S. A.* **2006**, 103(11), 4089-4094.

26. Paul, C. D., Kiss, C., Traore, D.A.K., Gong, L., Wilce, M.C.J., Devenish, R.J., Bradbury, A., and Prescott, M. Phanta: A Non-Fluorescent Photochromic Acceptor for pcFRET. *PLoS ONE* **2013**, 8(9), 1-9.

27. Dove, S.G., Hoegh-Guldberg, O., and Ranganathan, S. Major Colour Patterns of Reef-Building Corals Are Due to a Family of GFP-Like Proteins. *Coral Reefs* **2001**, 19(3), 197-204.

28. Oswald, F., Schmitt, F., Leutenegger, A., Ivanchenko, S., D'Angelo, C., Salih, A., Maslakova, S., Bulina, M., Schirmbeck, R., Nienhaus, G.U., Matz, M.V., and Wiedenmann, J. Contributions of Host and Symbiont Pigments to the Coloration of Reef Corals. *FEBS J.* **2007**, 274(4), 1102-1122.

29. Kelmanson, I.V. and Matz, M.V. Molecular Basis and Evolutionary Origins of Color Diversity in Great Star Coral Montastraea Cavernosa (Scleractinia: Faviida). *Mol. Biol. Evol.* **2003**, 20(7), 1125-1133.

30. Matz, M.V., Marshall, N.J.M., Vorobyev, M. Are Corals Colorful? *Photochem. Photobiol.* **2006**, 82(2), 345-350.

31. Dove, S.G., Takabayashi, M., and Hoegh-Guldberg, O. Isolation and Partial Characterization of the Pink and Blue Pigments of Pocilloporid and Acroporid Corals. *Biol. Bull.* **1995**, 189(3), 288-297.

32. Prescott, M., Ling, M., Beddoe, T., Oakley, A.J., Dove, S., Hoegh-Guldberg, O., Devenish, R.J., and Rossjohn, J. The 2.2 a Crystal Structure of a Pocilloporin Pigment Reveals a Nonplanar Chromophore Conformation. *Structure* **2003**, 11(3), 275-284.

33. Lukyanov, K.A., Fradkov, A.F., Gurskaya, N.G., Matz, M.V., Labas, Y.A., Savitsky, A.P., Markelov, M.L., Zaraisky, A.G., Zhao, X.N., Fang, Y., Tan, W.Y., and Lukyanov, S.A. Natural Animal Coloration Can Be Determined by a Nonfluorescent Green Fluorescent Protein Homolog. *J. Biol. Chem.* **2000**, 275(34), 25879-25882.

34. Andresen, M., Wahl, M.C., Stiel, A.C., Grater, F., Schafer, L.V., Trowitzsch, S., Weber, G., Eggeling, C., Grubmuller, H., Hell, S.W., and Jakobs, S. Structure and Mechanism of the Reversible Photoswitch of a Fluorescent Protein. *Proc. Natl. Acad. Sci. U. S. A.* **2005**, 102(37), 13070-13074.

35. Schafer, L.V., Groenhof, G., Klingen, A.R., Ullmann, G.M., Boggio-Pasqua, M., Robb, M.A., and Grubmuller, H. Photoswitching of the Fluorescent Protein asFP595: Mechanism, Proton Pathways, and Absorption Spectra. *Angew. Chem. Int. Ed.* **2007**, 46(4), 530-536.

36. Chudakov, D.M., Feofanov, A.V., Mudrik, N.N., Lukyanov, S., and Lukyanov, K.A. Chromophore Environment Provides Clue to "Kindling Fluorescent Protein" Riddle. *J. Biol. Chem.* **2003**, 278(9), 7215-7219.

37. Gurskaya, N.G., Fradkov, A.F., Terskikh, A., Matz, M.V., Labas, Y.A., Martynov, V.I., Yanushevich, Y.G., Lukyanov, K.A., and Lukyanov, S.A. GFP-Like Chromoproteins as a Source of Far-Red Fluorescent Proteins. *FEBS Lett.* **2001**, 507(1), 16-20.

38. Martynov, V.I., Maksimov, B.I., Martynova, N.Y., Pakhomov, A.A., Gurskaya, N.G., and Lukyanov, S.A. A Purple-Blue Chromoprotein from Goniopora Tenuidens Belongs to the Dsred Subfamily of GFP-Like Proteins. *J. Biol. Chem.* **2003**, 278(47), 46288-46292.

39. Shkrob, M.A., Yanushevich, Y.G., Chudakov, D.M., Gurskaya, N.G., Labas, Y.A., Poponov, S.Y., Mudrik, N.N., Lukyanov, S., and Lukyanov, K.A. Far-Red Fluorescent Proteins Evolved from a Blue Chromoprotein from *Actinia Equina*. *Biochem. J.* **2005**, 392(3), 649-654.

40. Chan, M.C.Y., Karasawa, S., Mizuno, H., Bosanac, I., Ho, D., Privé, G.G., Miyawaki, A., and Ikura, M. Structural Characterization of a Blue Chromoprotein and Its Yellow Mutant from the Sea Anemone Cnidopus Japonicus. *J. Biol. Chem.* **2006**, 281(49), 37813-37819.

41. Chiang, C.Y., Chen, Y.L., and Tsai, H.J. Different Visible Colors and Green Fluorescence Were Obtained from the Mutated Purple Chromoprotein Isolated from Sea Anemone. *Mar. Biotechnol.* **2014**, 16(4), 436-446.

42. Salih, A., Larkum, A., Cox, G., Kuhl, M., and Hoegh-Guldberg, O. Fluorescent Pigments in Corals Are Photoprotective. *Nature* **2000**, 408(6814), 850-853.

43. Alieva, N.O., Konzen, K.A., Field, S.F., Meleshkevitch, E.A., Hunt, M.E., Beltran-Ramirez, V., Miller, D.J., Wiedenmann, J., Salih, A., and Matz, M.V. Diversity and Evolution of Coral Fluorescent Proteins. *PLoS ONE* **2008**, 3(7), 1-12.

44. Beddoe, T., Ling, M., Dove, S., Hoegh-Guldberg, O., Devenish, R.J., Prescott, M., and Rossjohn, J. The Production, Purification and Crystallization of a Pocilloporin Pigment from a Reef-Forming Coral. *Acta Crystallogr. D Biol. Crystallogr.* **2003**, 59(3), 597-579.

45. Pettikiriarachchi, A., Gong, L., Perugini, M.A., Devenish, R.J., and Prescott, M. Ultramarine, a Chromoprotein Acceptor for Förster Resonance Energy Transfer. *PLoS ONE* **2012**, 7(7), 1-9.

46. Ormo, M., Cubitt, A.B., Kallio, K., Gross, L.A., Tsien, R.Y., and Remington, S.J. Crystal Structure of the Aequorea Victoria Green Fluorescent Protein. *Science* **1996**, 273(5280), 1392-1395.

47. Wall, M.A., Socolich, M., and Ranganathan, R. The Structural Basis for Red Fluorescence in the Tetrameric GFP Homolog DsRed. *Nat. Struct. Biol.* **2000**, 7(12), 1133-1138.

48. Strack, R.L., Strongin, D.E., Mets, L., Glick, B.S., and Keenan, R.J. Chromophore Formation in DsRed Occurs by a Branched Pathway. *J. Am. Chem. Soc.* **2010**, 132(24), 8496-8505.

49. Verkhusha, V.V., Chudakov, D.M., Gurskaya, N.G., Lukyanov, S., and Lukyanov, K.A. Common Pathway for the Red Chromophore Formation in Fluorescent Proteins and Chromoproteins. *Chem. Biol.* **2004**, 11(6), 845-854.

50. Bulina, M., Chudakov, D., Mudrik, N., and Lukyanov, K. Interconversion of Anthozoa GFP-Like Fluorescent and Non-Fluorescent Proteins by Mutagenesis. *BMC Biochem*. **2002**, 3(7), 1-8.

51. Gross, L.A., Baird, G.S., Hoffman, R.C., Baldridge, K.K., and Tsien, R.Y. The Structure of the Chromophore within DsRed, a Red Fluorescent Protein from Coral. *Proc. Natl. Acad. Sci. U. S. A.* **2000**, 97(22), 11990-11995.

52. Verkhusha, V.V. and Lukyanov, K.A. The Molecular Properties and Applications of Anthozoa Fluorescent Proteins and Chromoproteins. *Nat. Biotechnol.* **2004**, 22(3), 289-296.

53. Subach, F.V., Subach, O.M., Gundorov, I.S., Morozova, K.S., Piatkevich, K.D., Cuervo, A.M., and Verkhusha, V.V. Monomeric Fluorescent Timers That Change Color from Blue to Red Report on Cellular Trafficking. *Nat. Chem. Biol.* **2009**, 5(2), 118-126.

54. Yarbrough, D., Wachter, R.M., Kallio, K., Matz, M.V., and Remington, S.J. Refined Crystal Structure of DsRed, a Red Fluorescent Protein from Coral, at 2.0-Å Resolution. *Proc. Natl. Acad. Sci. U. S. A.* **2001**, 98(2), 462-467.

55. Petersen, J., Wilmann, P.G., Beddoe, T., Oakley, A.J., Devenish, R.J., Prescott, M., and Rossjohn, J. The 2.0-a Crystal Structure of eqFP611, a Far Red Fluorescent Protein from the Sea Anemone Entacmaea Quadricolor. *J. Biol. Chem.* **2003**, 278(45), 44626-44631.

56. Quillin, M.L., Anstrom, D.A., Shu, X.K., O'Leary, S., Kallio, K., Chudakov, D.A., and Remington, S.J. Kindling Fluorescent Protein from Anemonia Sulcata: Dark-State Structure at 1.38 Angstrom Resolution. *Biochemistry* **2005**, 44(15), 5774-5787.

57. Wilmann, P.G., Petersen, J., Pettikiriarachchi, A., Buckle, A.M., Smith, S.C., Olsen, S., Perugini, M.A., Devenish, R.J., Prescott, M., and Rossjohn, J. The 2.1 Angstrom Crystal Structure of the Far-Red Fluorescent Protein HcRed: Inherent Conformational Flexibility of the Chromophore. *J. Mol. Biol.* **2005**, 349(1), 223-237.

58. Battad, J.M., Wilmann, P.G., Olsen, S., Byres, E., Smith, S.C., Dove, S.G., Turcic, K.N., Devenish, R.J., Rossjohn, J., and Prescott, M. A Structural Basis for the pH-Dependent Increase in Fluorescence Efficiency of Chromoproteins. *J. Mol. Biol.* **2007**, 368(4), 998-1010.

59. Maddalo, S.L. and Zimmer, M. The Role of the Protein Matrix in Green Fluorescent Protein Fluorescence. *Photochem. Photobiol.* **2006**, 82(2), 367-372.

60. Rusanov, A.L., Mironov, V.A., Goryashenko, A.S., Grigorenko, B.L., Nemukhin, A.V., and Savitsky, A.P. Conformational Partitioning in pH-Induced Fluorescence of the Kindling Fluorescent Protein (KFP). *J Phys Chem B* **2011**, 115(29), 9195-9201.

61. Shagin, D.A., Barsova, E.V., Yanushevich, Y.G., Fradkov, A.F., Lukyanov, K.A., Labas, Y.A., Semenova, T.N., Ugalde, J.A., Meyers, A., Nunez, J.M., Widder, E.A., Lukyanov, S.A., and Matz, M.V. GFP-Like Proteins as Ubiquitous Metazoan Superfamily: Evolution of Functional Features and Structural Complexity. *Mol. Biol. Evol.* **2004**, 21(5), 841-850.

62. Park J. S., Cochran, J.R. Protein Engineering and Design. *CRC Press*, Boca Raton, **2010**.

63. Cordes, M.H., Davidson, A.R., and Sauer, R.T. Sequence Space, Folding and Protein Design. *Curr. Opin. Struct. Biol.* **1996**, 6(1), 3-10.

64. Chica, R.A., Moore, M.M., Allen, B.D., and Mayo, S.L. Generation of Longer Emission Wavelength Red Fluorescent Proteins Using Computationally Designed Libraries. *Proc. Natl. Acad. Sci. U. S. A.* **2010**, 107(47), 20257-20262.

65. Yuan, L., Kurek, I., English, J., and Keenan, R. Laboratory-Directed Protein Evolution. *Microbiol. Mol. Biol. Rev.* **2005**, 69(3), 373-392.

66. Hutchison, C.A., 3rd, Phillips, S., Edgell, M.H., Gillam, S., Jahnke, P., and Smith, M. Mutagenesis at a Specific Position in a DNA Sequence. *J. Biol. Chem.* **1978**, 253(18), 6551-6560.

67. Cirino, P.C., Mayer, K.M., and Umeno, D. Generating Mutant Libraries Using Error-Prone PCR. *Methods Mol. Bio.* **2003**, 231, 3-9.

68. Beckman, R.A., Mildvan, A.S., and Loeb, L.A. On the Fidelity of DNA Replication: Manganese Mutagenesis in Vitro. *Biochemistry* **1985**, 24(21), 5810-5817.

69. Drummond, D.A., Iverson, B.L., Georgiou, G., and Arnold, F.H. Why High-Error-Rate Random Mutagenesis Libraries Are Enriched in Functional and Improved Proteins. *J. Mol. Biol.* **2004**, 350(4), 806-816.

70. Sen, S., Dasu, V.V., and Mandal, B. Developments in Directed Evolution for Improving Enzyme Functions. *Appl. Biochem. Biotechnol.* **2007**, 143(3), 212-223.

71. Stemmer, W.P. DNA Shuffling by Random Fragmentation and Reassembly: In Vitro Recombination for Molecular Evolution. *Proc. Natl. Acad. Sci. U. S. A.* **1994**, 91(22), 10747-10751.

72. Zhao, H. and Zha, W. In Vitro 'Sexual' Evolution through the PCR-Based Staggered Extension Process (StEP). *Nat. Protoc.* **2006**, 1(4), 1865-1871.

73. Turner, N.J. Directed Evolution Drives the Next Generation of Biocatalysts. *Nat. Chem. Biol.* **2009**, 5(8), 567-573.

74. Aharoni, A., Griffiths, A.D., and Tawfik, D.S. High-Throughput Screens and Selections of Enzyme-Encoding Genes. *Curr. Opin. Chem. Biol.* **2005**, 9(2), 210-216.

75. Xu, M.H. and Wang, L.V. Photoacoustic Imaging in Biomedicine. *Rev. Sci. Instrum.* **2006**, 77(4), 041101-1-21.

76. Bell, A.G. Selenium and the Photophone. *Nature* **1880**, 22(569), 500-503.

77. Kruger, R.U. and Liu, P. Photoacoustic Ultrasound: Pulse Production and Detection in 0.5 % Liposyn. *Med. Phys.* **1994**, 21(7), 1179-1184.

78. Hoelen, C.G., de Mul, F.F., Pongers, R., and Dekker, A. Three-Dimensional Photoacoustic Imaging of Blood Vessels in Tissue. *Opt. Lett.* **1998**, 23(8), 648-650.

79. Gusev, V.E. and Karabutov, A.A. Laser Optoacoustics. Tran. Kevin Hendzel. *American Institute of Physics*, New York, **1993**.

80. Wang, L.V., Wu, H.I. Biomedical Optics: Principles and Imaging, *Book News, Inc.* **2007**.

81. Bauer, A.Q., Nothdurft, R.E., Erpelding, T.N., Wang, L.H.V., and Culver, J.P. Quantitative Photoacoustic Imaging: Correcting for Heterogeneous Light Fluence Distributions Using Diffuse Optical Tomography. *J. Biomed. Opt.* **2011**, 16(9), 096016-1-7.

82. Daoudi, K., Hussain, A., Hondebrink, E., and Steenbergen, W. Correcting Photoacoustic Signals for Fluence Variations Using Acousto-Optic Modulation. *Opt. Express* **2012**, 20(13), 14117-14129.

83. Prince, J.L. and Links, J. Medical Imaging Signals and Systems. *Pearson College Div*, **2014**.

84. Zhang, H.F., Maslov, K., and Wang, L.V. In Vivo Imaging of Subcutaneous Structures Using Functional Photoacoustic Microscopy. *Nat. Protoc.* **2007**, 2(4), 797-804.

85. Maslov, K., Zhang, H.F., Hu, S., and Wang, L.V. Optical-Resolution Photoacoustic Microscopy for in Vivo Imaging of Single Capillaries. *Opt. Lett.* **2008**, 33(9), 929-931.

86. Hu, S., Maslov, K., and Wang, L.V. Second-Generation Optical-Resolution Photoacoustic Microscopy with Improved Sensitivity and Speed. *Opt. Lett.* **2011**, 36(7), 1134-1136.

87. Chen, S.L., Burnett, J., Sun, D.X., Wei, X.B., Xie, Z.X., and Wang, X.D. Photoacoustic Microscopy: A Potential New Tool for Evaluation of Angiogenesis Inhibitor. *Biomed Opt Express* **2013**, 4(11), 2657-2666.

88. Yao, J. and Wang, L.V. Photoacoustic Microscopy. *Laser Photon. Rev.* **2013**, 7(5), 758-778.

89. Maslov, K., Stoica, G., and Wang, L.V. In Vivo Dark-Field Reflection-Mode Photoacoustic Microscopy. *Opt. Lett.* **2005**, 30(6), 625-627.

90. Hu, S. and Wang, L.V. Neurovascular Photoacoustic Tomography. *Front Neuroenergetics* **2010**, 2(10), 1-10.

91. Kim, C., Favazza, C., and Wang, L.V. In Vivo Photoacoustic Tomography of Chemicals: High-Resolution Functional and Molecular Optical Imaging at New Depths. *Chem. Rev.* **2010**, 110(5), 2756-2782.

92. Prahl, S. Optical Absorption of Hemoglobin. **1999**.

93. Hu, S. and Wang, L.V. Photoacoustic Imaging and Characterization of the Microvasculature. *J. Biomed. Opt.* **2010**, 15(1), 011101-1-15.

94. Shao, P., Shi, W., Chee, R.K.W., and Zemp, R.J. Mosaic Acquisition and Processing for Optical-Resolution Photoacoustic Microscopy. *J. Biomed. Opt.* **2012**, 17(8), 080503-1-3.

95. Jiang, Y., Forbrich, A., Harrison, T., and Zemp, R.J. Blood Oxygen Flux Estimation with a Combined Photoacoustic and High-Frequency Ultrasound Microscopy System: A Phantom Study. *J. Biomed. Opt.* **2012**, 17(3), 036012-1-8.

96. Staley, J., Grogan, P., Samadi, A.K., Cui, H.Z., Cohen, M.S., and Yang, X.M. Growth of Melanoma Brain Tumors Monitored by Photoacoustic Microscopy. *J. Biomed. Opt.* **2010**, 15(4), 040510-1-3.

97. Weight, R.M., Viator, J.A., Dale, P.S., Caldwell, C.W., and Lisle, A.E. Photoacoustic Detection of Metastatic Melanoma Cells in the Human Circulatory System. *Opt. Lett.* **2006**, 31(20), 2998-3000.

98. Galanzha, E.I., Shashkov, E.V., Spring, P.M., Suen, J.Y., and Zharov, V.P. In Vivo, Noninvasive, Label-Free Detection and Eradication of Circulating Metastatic Melanoma Cells Using Two-Color Photoacoustic Flow Cytometry with a Diode Laser. *Cancer Res.* **2009**, 69(20), 7926-7934.

99. Wang, Y., Maslov, K., Zhang, Y., Hu, S., Yang, L.M., Xia, Y.N., Liu, J.A., and Wang, L.H.V. Fiber-Laser-Based Photoacoustic Microscopy and Melanoma Cell Detection. *J. Biomed. Opt.* **2011**, 16(1), 011014-1-4.

100. Zhang, Y., Cai, X., Choi, S.W., Kim, C., Wang, L.H.V., and Xia, Y.N. Chronic Label-Free Volumetric Photoacoustic Microscopy of Melanoma Cells in Three-Dimensional Porous Scaffolds. *Biomaterials* **2010**, 31(33), 8651-8658.

101. Song, W., Wei, Q., Liu, T., Kuai, D., Burke, J.M., Jiao, S.L., and Zhang, H.F. Integrating Photoacoustic Ophthalmoscopy with Scanning Laser Ophthalmoscopy, Optical Coherence Tomography, and Fluorescein Angiography for a Multimodal Retinal Imaging Platform. *J. Biomed. Opt.* **2012**, 17(6), 061206-1-7.

102. Li, L., Zemp, R.J., Lungu, G., Stoica, G., and Wang, L.H.V. Photoacoustic Imaging of Lacz Gene Expression in Vivo. *J. Biomed. Opt.* **2007**, 12(2), 020504-1-3.

103. Li, L., Zhang, H.F., Zemp, R.J., Maslov, K., and Wang, L.H.V. Simultaneous Imaging of a Lacz-Marked Tumor and Microvasculature Morphology in Vivo by Dual-Wavelength Photoacoustic Microscopy. *J Innov Opt Health Sci* **2008**, 1(2), 207-215.

104. Krumholz, A., Vanvickle-Chavez, S.J., Yao, J., Fleming, T.P., Gillanders, W.E., and Wang, L.V. Photoacoustic Microscopy of Tyrosinase Reporter Gene in Vivo. *J. Biomed. Opt.* **2011**, 16(8), 080503-1-3.

105. Paproski, R.J., Forbrich, A.E., Wachowicz, K., Hitt, M.M., and Zemp, R.J. Tyrosinase as a Dual Reporter Gene for Both Photoacoustic and Magnetic Resonance Imaging. *Biomed. Opt. Express* **2011**, 2(4), 771-780.

106. Paproski, R.J., Heinmiller, A., Wachowicz, K., and Zemp, R.J. Multi-Wavelength Photoacoustic Imaging of Inducible Tyrosinase Reporter Gene Expression in Xenograft Tumors. *Sci. Rep.* **2014**, 4, 5329-1-7

107. Filonov, G.S., Krumholz, A., Xia, J., Yao, J., Wang, L.V., and Verkhusha, V.V. Deep-Tissue Photoacoustic Tomography of a Genetically Encoded near-Infrared Fluorescent Probe. *Angew. Chem. Int. Ed. Engl.* **2012**, 51(6), 1448-1451.

108. Förster T. Zwischenmolekulare Energiewanderung und Fluoreszenz. *Annalen der Physik* **1948**, 437(1-2), 55-75.

109. Lakowicz, J.R., Principles of Fluorescence Spectroscopy (3th ed.). *Berlin : Springer*, New York, **2006**.

110. Campbell, R.E. Fluorescent-Protein-Based Biosensors: Modulation of Energy Transfer as a Design Principle. *Anal. Chem.* **2009**, 81(15), 5972-5979.

111. Miyawaki, A., Llopis, J., Heim, R., McCaffery, J.M., Adams, J.A., Ikura, M., and Tsien, R.Y. Fluorescent Indicators for Ca^{2+} Based on Green Fluorescent Proteins and Calmodulin. *Nature* **1997**, 388(6645), 882-887.

112. Palmer, A.E., Giacomello, M., Kortemme, T., Hires, S.A., Lev-Ram, V., Baker, D., and Tsien, R.Y. Ca^{2+} Indicators Based on Computationally Redesigned Calmodulin-Peptide Pairs. *Chem. Biol.* **2006**, 13(5), 521-530.

113. Miyawaki, A., Griesbeck, O., Heim, R., and Tsien, R.Y. Dynamic and Quantitative Ca^{2+} Measurements Using Improved Cameleons. *Proc. Natl. Acad. Sci. U. S. A.* **1999**, 96(5), 2135-2140.

114. Aoki, K. and Matsuda, M. Visualization of Small GTPase Activity with Fluorescence Resonance Energy Transfer-Based Biosensors. *Nat. Protoc.* **2009**, 4(11), 1623-1631.

115. Zhang, J. and Allen, M.D. Fret-Based Biosensors for Protein Kinases: Illuminating the Kinome. *Mol. Biosyst.* **2007**, 3(11), 759-765.

116. Aye-Han, N.N., Allen, M.D., Ni, Q., and Zhang, J. Parallel Tracking of Camp and Pka Signaling Dynamics in Living Cells with Fret-Based Fluorescent Biosensors. *Mol. Biosyst.* **2012**, 8(5), 1435-1440.

117. Heim, R. and Tsien, R.Y. Engineering Green Fluorescent Protein for Improved Brightness, Longer Wavelengths and Fluorescence Resonance Energy Transfer. *Curr. Biol.* **1996**, 6(2), 178-182.

118. Wu, X.L., Simone, J., Hewgill, D., Siegel, R., Lipsky, P.E., and He, L.S. Measurement of Two Caspase Activities Simultaneously in Living Cells by a Novel Dual Fret Fluorescent Indicator Probe. *Cytom. Part A* **2006**, 69A(6), 477-486.

119. Figueroa, R.A., Ramberg, V., Gatsinzi, T., Samuelsson, M., Zhang, M., Iverfeldt, K., and Hallberg, E. Anchored FRET Sensors Detect Local Caspase Activation Prior to Neuronal Degeneration.*Mol Neurodegener* **2011**, 6(1), 35-45.

120. Kominami, K., Nagai, T., Sawasaki, T., Tsujimura, Y., Yashima, K., Sunaga, Y., Tsuchimochi, M., Nishimura, J., Chiba, K., Nakabayashi, J., Koyamada, K., Endo, Y., Yokota, H., Miyawaki, A., Manabe, N., and Sakamaki, K. In Vivo Imaging of Hierarchical Spatiotemporal Activation of Caspase-8 During Apoptosis. *PLoS ONE* **2012**, 7(11), 1-18.

121. Grashoff, C., Hoffman, B.D., Brenner, M.D., Zhou, R., Parsons, M., Yang, M.T., McLean, M.A., Sligar, S.G., Chen, C.S., Ha, T., and Schwartz, M.A. Measuring Mechanical Tension across Vinculin Reveals Regulation of Focal Adhesion Dynamics. *Nature* **2010**, 466(7303), 263-266.

122. Esposito, A., Gralle, M., Dani, M.A.C., Lange, D., and Wouters, F.S. Phlameleons: A Family of Fret-Based Protein Sensors for Quantitative pH Imaging. *Biochemistry* **2008**, 47(49), 13115-13126.

123. Shaner, N.C., Campbell, R.E., Steinbach, P.A., Giepmans, B.N.G., Palmer, A.E., and Tsien, R.Y. Improved Monomeric Red, Orange and Yellow Fluorescent Proteins Derived from Discosoma Sp. Red Fluorescent Protein. *Nat. Biotechnol.* **2004**, 22(12), 1567-1572.

124. Fromant, M., Blanquet, S., and Plateau, P. Direct Random Mutagenesis of Gene-Sized DNA Fragments Using Polymerase Chain Reaction. *Anal. Biochem.* **1995**, 224(1), 347-353.

125. Sambrook, J. and Russell, D.W., Molecular Cloning : A Laboratory Manual (3th ed.), *Cold Spring Harbor Laboratory Press*, New York., **2001**.

126. Harrison, T., Ranasinghesagara, J.C., Lu, H.H., Mathewson, K., Walsh, A., and Zemp, R.J. Combined Photoacoustic and Ultrasound Biomicroscopy. *Opt. Express* **2009**, 17(24), 22041-22046.

127. Truong, K. and Ikura, M. The Use of Fret Imaging Microscopy to Detect Protein-Protein Interactions and Protein Conformational Changes in Vivo. *Curr. Opin. Struct. Biol.* **2001**, 11(5), 573-578.

128. Lalonde, S., Ehrhardt, D.W., and Frommer, W.B. Shining Light on Signaling and Metabolic Networks by Genetically Encoded Biosensors. *Curr. Opin. Plant Biol.* **2005**, 8(6), 574-581.

129. Rusanov, A.L., Ivashina, T.Y., Vinokurov, L.M., Fiks, I.L., Orlova, A.G., Turchin, I.V., Meerovich, I.G., Zherdeva, V.V., and Savitsky, A.P. Lifetime Imaging of FRET between Red Fluorescent Proteins. *J. Biophotonics* **2010**, 3(12), 774-783.

130. Savitsky, A.P., Rusanov, A.L., Zherdeva, V.V., Gorodnicheva, T.V., Khrenova, M.G., and Nemukhin, A.V. FLIM-FRET Imaging of Caspase-3 Activity in Live Cells Using Pair of Red Fluorescent Proteins. *Theranostics* **2012**, 2(2), 215-226.

131. Hoi, H., Howe, E.S., Ding, Y.D., Zhang, W., Baird, M.A., Sell, B.R., Allen, J.R., Davidson, M.W., and Campbell, R.E. An Engineered Monomeric Zoanthus Sp Yellow Fluorescent Protein. *Chem. Biol.* **2013**, 20(10), 1296-1304.

132. Lam, A.J., St-Pierre, F., Gong, Y., Marshall, J.D., Cranfill, P.J., Baird, M.A., McKeown, M.R., Wiedenmann, J., Davidson, M.W., Schnitzer, M.J., Tsien, R.Y., and Lin, M.Z. Improving Fret Dynamic Range with Bright Green and Red Fluorescent Proteins. *Nat. Methods* **2012**, 9(10), 1005-1012.

133. Clegg, R.M. "Chapter 1 Förster Resonance Energy Transfer—FRET What Is It, Why Do It, and How It's Done″ Laboratory Techniques in Biochemistry and Molecular Biology, Eds. Vliet, P.C.V. and Pillai, S. *North-Holland pub. co*, Amsterdam, **2009**, 33, 1-57.

134. Bortner, C.D. and Cidlowski, J.A. Apoptotic Volume Decrease and the Incredible Shrinking Cell. *Cell Death Differ.* **2002**, 9(12), 1307-1310.

135. Griesbeck, O., Baird, G.S., Campbell, R.E., Zacharias, D.A., and Tsien, R.Y. Reducing the Environmental Sensitivity of Yellow Fluorescent Protein. Mechanism and Applications. *J. Bio. Chem.* **2001**, 276(31), 29188-29194.

136. Truong, K., Sawano, A., Mizuno, H., Hama, H., Tong, K.I., Mal, T.K., Miyawaki, A., and Ikura, M. Fret-Based in Vivo Ca^{2+} Imaging by a New Calmodulin-GFP Fusion Molecule. *Nat. Struct. Biol.* **2001**, 8(12), 1069.

137. Ding, Y.D., Ai, H.W., Hoi, H., and Campbell, R.E. Forster Resonance Energy Transfer-Based Biosensors for Multiparameter Ratiometric

Imaging of Ca^{2+} Dynamics and Caspase-3 Activity in Single Cells. *Anal. Chem.* **2011**(24), 9687-9693.

138. Berridge, M.J., Lipp, P., and Bootman, M.D. The Versatility and Universality of Calcium Signalling. *Nat. Rev. Mol. Cell Biol.* **2000**, 1(1), 11-21.

139. Palmer, A.E. and Tsien, R.Y. Measuring Calcium Signaling Using Genetically Targetable Fluorescent Indicators. *Nat. Protoc.* **2006**, 1(3), 1057-1065.

140. Carlson, H.J. and Campbell, R.E. Circular Permutated Red Fluorescent Proteins and Calcium Ion Indicators Based on Mcherry. *Protein Eng. Des. Sel.* **2013**, 26(12), 763-772.

141. Ntziachristos, V. Going Deeper Than Microscopy: The Optical Imaging Frontier in Biology. *Nat. Methods* **2010**, 7(8), 603-614.

142. Filonov, G.S., Piatkevich, K.D., Ting, L.-M., Zhang, J., Kim, K., and Verkhusha, V.V. Bright and Stable near-Infrared Fluorescent Protein for in Vivo Imaging. *Nat. Biotechnol.* **2011**, 29(8), 757-763.

143. Alford, S.C., Ding, Y., Simmen, T., and Campbell, R.E. Dimerization-Dependent Green and Yellow Fluorescent Proteins. *ACS Synth. Biol.* **2012**, 1(12), 569-575.